NORTHWESTERN UNIVERSITY

Protein Stabilization with Metal–Organic Frameworks for Drug Delivery and Catalysis

A DISSERTATION

SUBMITTED TO THE GRADUATE SCHOOOL

IN PARTIAL FULFILLMENT OF THE REQUIREMENTS

for the degree

DOCTOR OF PHILOSOPHY

Field of Chemistry

By

Yijing Chen

EVANSTON, ILLINOIS

September 2021

Abstract

Proteins are known to have diverse biomedical functions and excellent catalytic performance; however, they are also fragile outside living cells, challenging their use in industrial applications. Metal-organic frameworks (MOFs) are highly porous crystalline materials that consist of metal cluster nodes and organic linkers. With their rigid structures, MOFs can effectively prevent structural changes of proteins after encapsulation and further increase the protein's stability under different conditions. Importantly, the high surface areas and tunability of MOFs give rise to many possible structures which can achieve high protein loading capacities as well as concentrate the substrate to enhance reaction rates for catalysis.

Therefore, one of the focuses of this thesis is the encapsulation of proteins with MOFs to enhance their stability in denaturing conditions that occur during the therapeutic protein delivery process. For that application, an insulin@MOF composite was designed and synthesized by encapsulating insulin in a MOF. The MOF can stabilize insulin in stomach acid by preventing its unfolding in an acidic environment while performing size exclusion towards the degradation enzyme existing in the stomach. After insulin@MOF reached the blood environment, MOF will start to degrade under the presence of phosphate ions and release a large amount of insulin from it. In addition, after DNA modification, the insulin@MOF nanoparticles show greatly enhanced colloidal stability and can penetrate the cells and enable the intercellular delivery of target large biomolecules.

The other half of this thesis focuses on the stabilization of enzymes with MOFs for enhanced catalysis. Formate dehydrogenases (FDH), a class of enzymes that catalyze the reduction of CO_2 to formic acid, show increased stability in both acidic and neutral environments upon encapsulation within a MOF. The regeneration of co-enzyme nicotinamide adenine dinucleotide

(NADH) can be realized electrochemically via a modified fluorine-doped tin oxide (FTO) glass electrode. The photochemical NADH regeneration can also be achieved after MOF-modification with an electron mediator. With the coupling of the enzymatic CO_2 fixation and the electrochemical or photochemical cofactor regeneration, formic acid can be produced using CO_2 in the atmosphere and a catalytic amount of NADH at high efficiency. The mechanism of the enhanced catalytic performance of MOF-encapsulated enzyme was also investigated with different characterization instruments. From both experimental and simulation results, an enzyme Cytochrome c (Cyt c) shows structural changes in its heme-based active center during MOF encapsulation, likely resulting in enhanced accessibility of the active center to reaction substrates.

In this thesis, proteins are encapsulated in and stabilized by MOFs for both protein delivery and enhanced biocatalysis applications. The mechanism of the enhanced performance of MOF encapsulated protein is also investigated.

Acknowledgements

Thank you to everyone who is there with me during my graduate study. I may not be able to list everyone here due to the limit of the space, I do appreciate all of your help, support, and companion along the way.

Firstly, I would like to thank my advisor Professor Omar Farha for letting me join this amazing research group and for giving me this exciting project to work on. Omar was always there to encourage me to work on the projects that I am interested in and was always approachable when I need to discuss. I also want to thank Professor Joseph Hupp for the helpful discussions we had and for the support he provided when I was applying for fellowships and jobs. I would like to thank all of the program assistants in the group, Amanda Mahoney, Abby Rosensweig, and Nick Huryk who have helped to make my life so much easier by solving all of the random problems I had.

I would like to everyone in the group who has participated in my projects, Peng Li, Xuan Zhang, Cassandra Buru, Chung-Wei Kung, Hyunho Noh, Xingjie Wang, Satoshi Kato, Xinyi Gong, Fanrui Sha, I wouldn't be able to learn that much and finish all of those projects by myself without your help. I would also like to thank my collaborators outside the group, Justin Modica, Luka Đorđević, Jiawang Zhou, Felipe Jiménez-Angeles, Baofu Qiao, Matthew D. Krzyaniak, for the fun discussions we had and for teaching me things that I might not be able to learn working in my group.

I would like to thank everyone in the group for always being amazing, I enjoyed my time working in the lab because of you. Cassandra Buru, thank you for being my TA, my mentor, my collaborator, my friend and my wedding officiant, I feel so lucky to meet you in graduate school. Xinyi Gong, thank you for always being supportive of my choices, for your companion during

my hard times and for all the fun we had. Fanrui Sha, thank you for being an amazing mentee and for being a cheerful person to work with. I would also want to thank Chung-Wei Kung, Kenichi Otake, Satoshi Kato, Hyunho Noh, Seung-Joon Lee, Rodrigo Maldonado, Megan Wasson, Tim Goetjen, Kenton Hicks, Sylvia Hanna for the fun times we had on Thursdays.

I would also like to thank my friends who have helped me surviving graduate school. Rui Wang, Dawn Duan, Wuliang Zhang, thank you for bringing me all the delicious food you cooked. Tracy Chen, thank you for being able to give me wise suggestions when I am struggling in life. I also want to thank my friends who came to Northwestern the same year as me, Eunice Bae, Priscilla Choo, Wuliang Zhang, Wenjie Zhou, Xiaotong Li, Yue Wu, you have made my graduate life a lot more enjoyable. Wenting Deng, it is my honor to be your friend for over 15 years, I feel so lucky to have a friend with whom I can share all of the happiness and sadness in my life with.

I would also want to thank my family for their supports, and I would never be able to achieve what I have now without them. Mom and dad, I am so lucky to have parents like you that are very supportive of every decision I ever made. I would not be able to finish my Ph.D. without your financial and mental support and I am so proud of you for being able to understand what I did for my Ph.D. research. Lastly, I want to thank Allen Yang for being around every time I need help and for sharing his honest opinions to figure out the best solution when I met with difficulties. Thank you for being my husband and my best friend and thank you for encouraging me not to give up and to finish my Ph.D. when I had struggles.

Table of Contents

List of Figures

List of Tables

Chapter 1 . Introduction to Protein Encapsulation with Metal-Organic Frameworks and its Applications

1.1 Motivation: Protein Immobilization

Functional proteins are of great significance in a wide variety of fields. Because of their unique biological and biotechnical applications and outstanding performance in reactions, proteins are in great demand in disease treatment,[1-2] bioimaging,[3] as well as serving as catalysts in reactions to realize high production yield and good product selectivity.[4] However, proteins usually suffer from poor stability which hinders their applications in being formulated into protein-based drugs[5] Additionally, the difficulty in enzyme recycling and poor enzyme stability also limit the wide applications of using enzymes for industrial catalysis.

Because of the difficulty in recycling and poor stability of proteins, researchers have investigated techniques to immobilize them by different methods. Among different reported protein immobilization techniques reported: physical adsorption of proteins onto a substrate suffers from protein leaching under varying local environments;[6] covalently binding of all proteins onto various substrate following one robust method still remains challenging;[7] chemical cross-linking of the enzymes could lead to the alteration of the original protein structure and further affect the function of proteins.[8] Entrapment/encapsulation of proteins with heterogeneous materials, on the other hand, remains a promising immobilization method to minimize protein leaching as well as protecting its original structure. A variety of solid supports such as hydrogels,[9-10] porous silica,[11-12] synthetic polymers,[13] and activated carbon,[14] have been studied to encapsulate proteins to gain recyclability and to enhance stability.

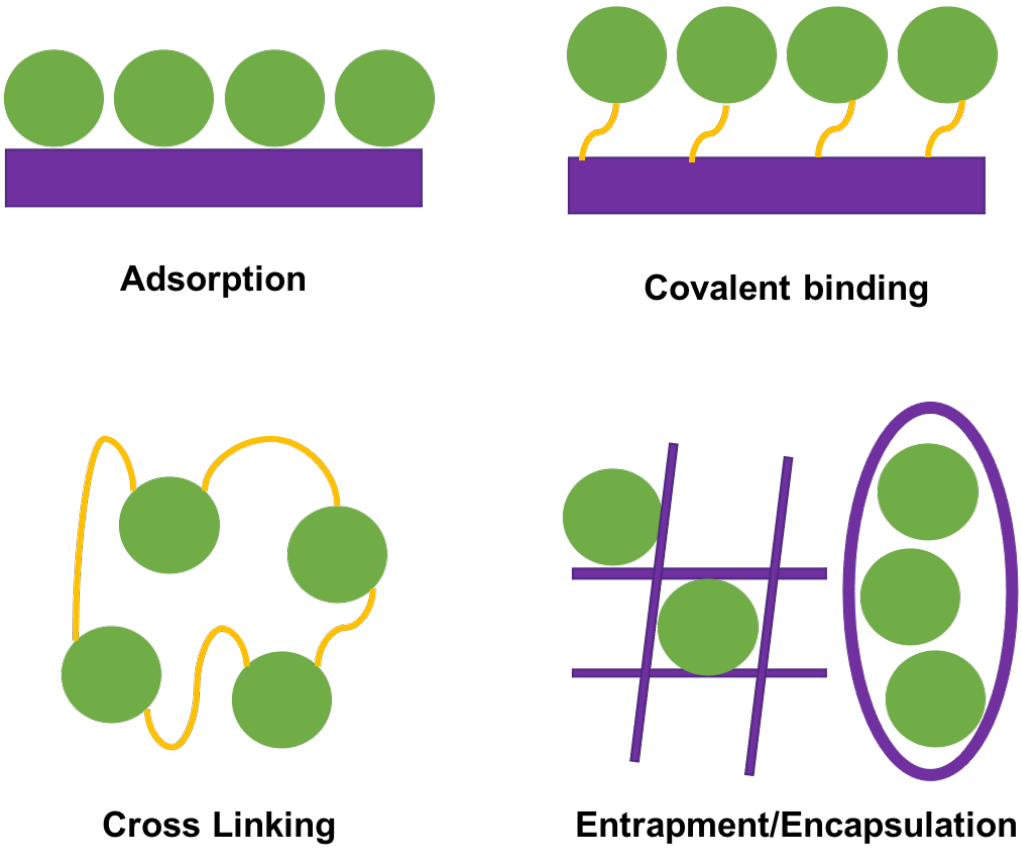

Figure 1-1 Illustration of protein immobilization techniques.

1.2 Metal-Organic Frameworks as Protein Supports

Metal-organic frameworks (MOFs) are porous and crystalline materials that are consist of inorganic metal or metal clusters nodes and organic linkers. Due to the diversity in the topologies of the nodes and the linkers, MOFs with diverse structures and functions can be designed and synthesized by isoreticular design, topology-guided design, and modulated synthesis as well as post-synthetic modification methods.[15] Due to their high porosity, well-defined structure as well as high tunability, MOFs are considered to have potentials in gas storage and separation,[16-18] chemical separation,[19-20] heterogenous catalysis,[21-22] and chemical sensing.[23]

Recently, MOF materials have also been investigated for protein immobilization applications.[24-25] The encapsulation of proteins in MOFs can be achieved via two pathways. Firstly,

proteins are introduced during the MOF synthesis process (*in vivo* encapsulation). With proteins serving as seeds, MOF will then gradually grow around them in the reaction mixture and encapsulate them during the MOF growth. Secondly, the pre-synthesized meso-porous MOFs are added to solutions that contains proteins (post-synthetic encapsulation). Driven by the interactions between proteins and MOFs, proteins can gradually enter the pores of MOFs through diffusion. There are three possible mechanisms by which proteins can be stabilized by MOFs: firstly, the spatial constraints provided by the pores of MOFs could limit protein unfolding and could further help proteins retaining its original structure; secondly, being confined in MOF pores, protein aggregation and deactivation can be largely limited; lastly, the interaction between MOF pores and the encapsulated proteins could lead to the shift of protein conformation and results in a more ordered and favorable protein structure.[26] Due to the stabilizing effect of MOFs on the encapsulated proteins, MOFs can be used in protecting proteins for diverse applications.

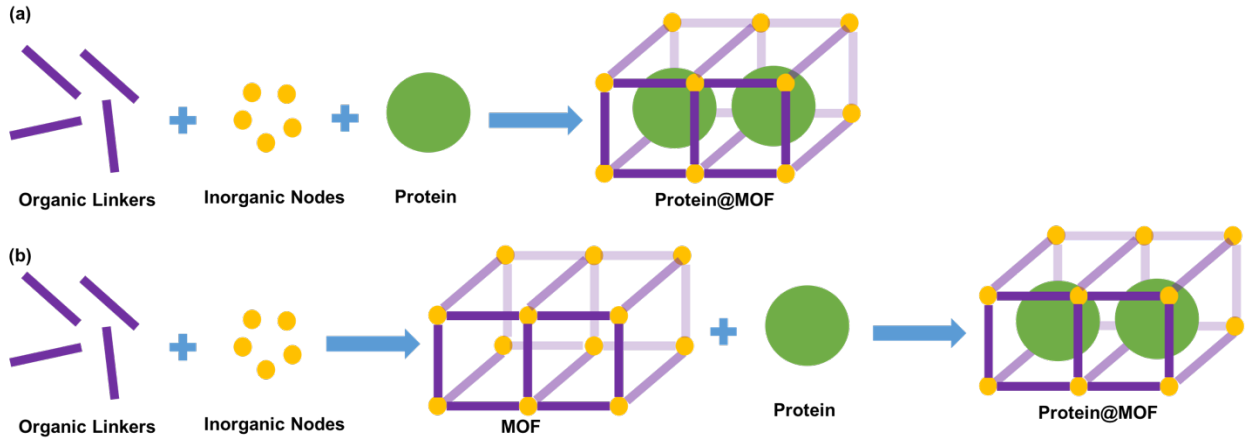

Figure 1-2 Illustration of two pathways to encapsulate proteins in MOFs. (a) *in vivo* encapsulation. (b) post-synthetic encapsulation.

1.3 Stabilizing Insulin as A Model Therapeutic Proteins in MOFs for Delivery

Therapeutic proteins are of increasing importance in recent years because of their diverse function, high bioactivity, and specificity. Despite their excellent performance compared to conventional drugs, their

broad application has been limited by the high costs of production and purification, the cold storage and transportation requirement, short shelf life, as well as the ineffective delivery methods. Insulin, one of the most well-known protein-based drugs, is widely used in the treatment of diabetes. As an anabolic hormone in the body, it regulates the blood sugar level by promoting the uptake of glucose by the liver. As of the year 2017, more than 29 million people in the US have diabetes[27] and the total Medicare Part D spending on insulin has reached $13.3 billion.[28] Despite the wide need for effective diabetes treatment, subcutaneous injection of insulin still remains the main therapy due to the instability of insulin in the stomach.

With their relatively rigid structures, MOFs can effectively prevent structural changes of proteins after encapsulation and further increase the protein's stability under different conditions. Also, the growth of MOF crystals can be controlled within the nano regime during synthesis, and the intracellular drug delivery of proteins via MOF nanocarriers can be realized. Importantly, the high surface areas and tunability of MOFs give rise to many possible structures which can achieve high protein loading capacities as well as concentrate the substrate to enhance reaction rates. In this thesis, a Zr-based MOF, NU-1000, is found to be able to successfully protects insulin from degradation in a simulated stomach environment. When the insulin@NU-1000 composite ends up in the simulated blood condition, the phosphate ions from the blood plasma will trigger the degradation of MOF and result in the release of insulin. To improve the MOFs as potential drug carriers, NU-1000 of a wide variety of sizes can be synthesized by tuning the synthetic conditions. The nano-sized NU-1000 can be brought into the cells through endocytosis. To prevent the aggregation of MOF nanoparticles, phosphate-modified DNA strands were utilized to functionalize the surface of MOFs to enhance their colloidal stability. Details on the protein-based drug delivery application of MOF will be discussed in later chapters.

1.4 Stabilizing Enzymes in MOFs for Enhanced Catalysis

Developing techniques to combat the rising levels of carbon emissions is an urgent challenge that scientists and engineers are addressing to reduce environmental change. Thus, the exploration of new pathways to realize CO_2 reduction and the conversion of CO_2 into other value-added products using green energy sources becomes significant. One of the most efficient methods to mitigate atmospheric CO_2 is biological carbon fixation. This process is widely observed in nature, with the photosynthetic process being a commonly known example, and these processes usually require the participation of enzymes.

However, the high cost of enzymatic cofactors and the instability of common CO_2 fixation enzymes in non-physiological conditions have limited the development of this method. As a solution, the regeneration of cofactors with a renewable source of energy (e.g. electricity or sunlight) and the enhancement of the enzymatic reaction rates, can both be achieved by stabilizing these carbon fixation enzymes within MOFs.

In this thesis, formate dehydrogenases (FDH), a class of enzymes that catalyze the oxidation of formate to CO_2 as well as the reverse reaction, is encapsulated and stabilized by MOF NU-1006. The enzyme shows increased stability in acidic environments upon encapsulation within a MOF. In addition, the encapsulated FDH demonstrates enhanced activity even at the optimal pH. The regeneration of co-enzyme nicotinamide adenine dinucleotide (NADH) required by the reaction electrochemically can be achieved by modifying a fluorine-doped tin oxide (FTO) glass electrode with a Rh complex. Additionally, drop-casting the encapsulated enzyme on the surface of the Rh modified electrode can couple the enzymatic CO_2 fixation and the electrochemical cofactor regeneration. The further modified electrode can produce formate using environmental CO_2 and a small amounts of NADH at high turnover frequency. On the other hand, after modifying the MOF supports with the same Rh complex, the modified MOF as enzyme supports can be

excited by white light, delivering the photoelectrons to the Rh complex for photochemical co-enzyme regeneration. The photochemically regenerated co-enzyme can then be consumed by the FDH encapsulated in the MOF pores for efficient CO_2 reduction. More details on using MOF to stabilize FDH for CO_2 reduction will be included in the following chapters.

1.5 Investigation of Structures of MOF Encapsulated Enzyme

Noting that in the MOF encapsulated FDH shows significantly enhanced activity even under the optimal reaction pH of the enzyme, the mechanism behind the improved catalytic performance is investigated. Three hypotheses have been brought up to explain the improved activity: firstly, the enzyme is retained in its favorable structure during the reaction, as a result, the encapsulated enzyme is protected against degradation or aggregation; secondly, the high surface area of MOFs would enable the accumulation of reaction substrate inside the MOFs and the high local concentration in MOF pores can further facilitate the enzyme reaction; lastly, the enzyme could be confined in a structure that favors the reaction after entering the MOF pores which leads to its higher activity compared to the native enzyme.

Previously, enzymes have been proved to show enhanced stability against denaturing conditions after being entrapped in MOFs. For example, MOFs are able to protect proteins under high environmental temperature, in organic solvents, or under acidic conditions. There have been studies on the substrate preconcentration in the MOF pores, affecting the apparent catalytic reaction rate. However, there is a lack of studies to understand the structure of MOF encapsulated enzymes. Thus, in this thesis, the enzyme cytochrome c (Cyt c) was selected as a model enzyme to probe the behavior and structural change when enzymes enter the MOFs. In the study, Cyt c@NU-1000 shows increased activity measured by both UV-Vis (overestimating the reaction rate of Cyt c@NU-1000) and ITC (underestimating the reaction rate of Cyt c@NU-1000). Both

experimental and simulation results showed that Cyt c went through structural changes around its heme-based active center during MOF encapsulation. As a result of the change, the catalytic active center in Cyt c becomes more accessible to the reaction substrates and resulted in a faster reaction.

1.6 Outline

This thesis focuses on taking advantage of the stabilization effect that MOFs have on proteins. For one of the applications of MOF stabilized proteins, insulin-loaded MOF is designed and characterized and the potential of using MOFs as insulin carriers for oral delivery is investigated. The colloidal stability and the cytotoxicity of the MOF nanoparticles have been tested. In the MOF encapsulated enzyme for efficient CO_2 reduction study, MOF encapsulated FDH has been synthesized, characterized and the activity of the encapsulated FDHvhas also been tested. The coenzyme regeneration (photochemical and electrochemical regeneration) is coupled with enzymatic CO_2 reduction to achieve efficient and sustainable CO_2 fixation. The mechanism of MOF encapsulated enzyme showing high catalytic performance is also studied using Cyt c as a model enzyme. The structure of the encapsulated Cyt c is investigated using various experimental characterization techniwues well as MD simulation to understand

Chapter 2 describes a proof-of-concept work where immobilize insulin in a crystalline mesoporous MOF, NU-1000, and obtain a high loading of ~40 wt% in only 30 min. The acid-stable MOF capsules are found to effectively prevent insulin from degrading in the presence of stomach acid and the digestive enzyme, pepsin. Furthermore, the encapsulated insulin can be released from NU-1000 under simulated physiological conditions.

In Chapter 3, the MOF-based protein hosts have been further improved by tuning their sizes and modifying their surface with phosphate-terminated oligonucleotides to form MOF nanoparticle (MOF NP) conjugates for both NU-1000 and PCN-222/MOF-545. They have been

characterized structurally and with respect to their ability to enter mammalian cells. The MOFs act as protein hosts and their densely functionalized, oligonucleotide-rich surfaces make them colloidally stable and ensure facile cellular entry. With insulin as a model protein, high loading and a 10-fold enhancement of cellular uptake (as compared to that of the native protein) were achieved. Importantly, this approach can be generalized to facilitate the delivery of a variety of proteins as biological probes or potential therapeutics.

Chapter 4 takes advantage of the stabilization effect of MOF on encapsulated proteins to form a bio-electrocatalytic system by depositing crystallites of a mesoporous MOF, NU-1006, encapsulated with formate dehydrogenase on a fluorine-doped tin oxide glass electrode modified with Cp*Rh(2,2'-bipyridyl-5,5'-dicarboxylic acid)Cl_2 complex. The system continuously converts CO_2 into formic acid at a rate of 79 ± 3.4 mM/h with electrochemical regeneration of the cofactor nicotinamide adenine dinucleotide. More notably, the MOF-enzyme composite exhibited significantly higher catalyst stability when subjected beyond the native environment (i.e. from neutral to acidic pH), doubling the formic acid yield compared to the free enzyme.

Chapter 5 again takes the structure and function of MOF NU-1006 to establish a semi-artificial system - containing an immobilized enzyme, formate dehydrogenase, in a light-harvesting scaffold - is reported for the conversion of CO_2 to formic acid using white light. The electron-mediator Cp*Rh(2,2'-bipyridyl-5,5'-dicarboxylic acid)Cl_2 was anchored to the nodes of the MOF NU-1006 to facilitate ultrafast photo-induced electron transfer when irradiated, leading to the reduction of the coenzyme nicotinamide adenine dinucleotide at a rate of about 28 mM h^{-1}. Most importantly of all, the immobilized enzyme utilizes the reduced coenzyme to generate formic acid selectively from CO_2 at a high turnover frequency of about 865 h^{-1} in 24 hours. The outcome of this research is the demonstration of a feasible pathway for solar-driven carbon fixation.

Chapter 6 attempts to determine the mechanism of the enhanced catalytic performance showed by MOF encapsulated enzyme. The structural change of cytochrome c (Cyt c) upon encapsulation within MOF NU-1000, is investigated through a combination of experimental and computational methods, such as electron paramagnetic resonance, diffuse reflective ultraviolet-visible spectroscopies, and all-atom explicit solvent molecular dynamics simulations. The enhanced catalytic performance of Cyt c after being encapsulated with NU-1000 is supported by the physical and in silico observations of a change in the heme ferric active center.

Chapter 2 . Acid-Resistant Mesoporous Metal–Organic Framework Toward Oral Insulin Delivery: Protein Encapsulation, Protection & Release

Portions of this chapter appear in the following manuscript:

Chen, Y. *, Li, P. *, Modica, J. A., Drout, R. J., & Farha, O. K.. Acid-resistant Mesoporous Metal–Organic Framework Toward Oral Insulin Delivery: Protein Encapsulation, Protection, and Release. *JACS*, **2018**, *140*, 5678-5681.

Contribution:

For the paper, **Chen,Y.** conducted all the MOF synthesis, insulin encapsulation and nearly all characterization, except confocal laser scanning microscopy and thermogravimetric analysis conducted by Li, P. Other co-authors have contributed to constructive scientific discussions and hence are listed as part of the co-author list.

2.1 Introduction

Diabetes currently affects more than 30 million Americans and as a result, costs the United States government approximately $245 billion per year as of 2012.[29] This chronic metabolic disease leads to long-term organ damage, and in some cases, death.[30-31] Diabetes causes affected individuals to have excessive glucose content in their bloodstream. Insulin, a hormone produced by the pancreas, is responsible for regulating the concentration of glucose in blood plasma. Currently, direct insulin injection3 remains the only effective therapeutic treatment for insulin resistant (IR) patients, even though several therapies have been designed to treat type I (T1DM) and type II (T2DM) diabetes mellitus. The development of oral insulin delivery methods is therefore necessary to reduce the pain and inconvenience inflicted on patients who must routinely receive insulin subcutaneously by injection.

Advancements in developing an oral insulin delivery agent have been hindered by challenges arising from the instability of insulin in the stomach. In the gastrointestinal tract, insulin is degraded by proteolytic enzymes thereby limiting the transport of insulin across the intestinal epithelium into the bloodstream. In this degradation process, the disulfide bonds in insulin are first cleaved by gastric acid, the fluid in the stomach composed of HCl and NaCl, initiating denaturation.[32] The unfolded insulin chains are then broken into short multi-peptide segments by pepsin, a digestive enzyme. Ongoing efforts dedicated to developing oral insulin delivery agents aim to achieve high loading capacities, stabilize the protein against degradation, and release the insulin cargo in a controlled manner.[33]

Encapsulation in biocompatible nanocarriers is recognized as a promising strategy for oral insulin delivery because particles of this size can facilitate paracellular or transcellular transport of insulin across the intestinal mucosa.[34] To this end, various materials such as alginate beads,[35-36]

nanoparticles,[37] poly nanocapsules,[38] and collagen[39] have been examined as insulin encapsulation and delivery agents; however, due to their low porosity, these materials exhibit only moderate insulin loading capacities (~5-30 wt%).[40] To achieve the desired insulin concentration (100 IU/mL) with these agents, an excess amount of the support material would be required. Further, the current strategy for increasing insulin loading requires the incorporation of adsorption enhancers like bile salts, fatty acids, and surfactants;[41] however, this increases the concentration of undesirable molecules delivered to the patient. Therefore, development of a carrier with high insulin capacity is imperative to make oral insulin delivery feasible. An acid stable, highly porous material would likely protect insulin from degradation and exhibit a high insulin loading capacity.

Metal–organic frameworks (MOFs) are crystalline porous materials composed of metal nodes connected by organic ligands.[42] By judicious selection of the node and ligand, MOFs can be elegantly tuned toward various applications including, but not limited to, gas storage/separation,[43-44] heterogeneous ca-talysis,[45-47] and chemical separation.[48] Most recently, MOFs have been examined for drug delivery[49-53] and enzyme fixation.[54-58] Though immobilization of biomolecules in MOFs could be realized through either de novo or post-synthetic methods,[59-63] the number of MOFs suitable for insulin encapsulation and oral delivery is still limited[64] due to their instability in the aqueous acidic environment of the stomach (pH=1.5-3.5). We hypothesized that immobilization of insulin in zirconium MOFs would be advantageous because (1) they can survive in neutral to acidic media (pH as low as 1); (2) their pore size and surface charge can be tailored to interact favorably with insulin and increase the loading; and (3) can disassemble in the presence of phosphate ions in the blood stream which irreversibly cleave the node-linker bonds[65-66] thereby initiating insulin release. Therefore, we chose a Zr_6-based mesoporous MOF, NU-1000, as an insulin carrier.

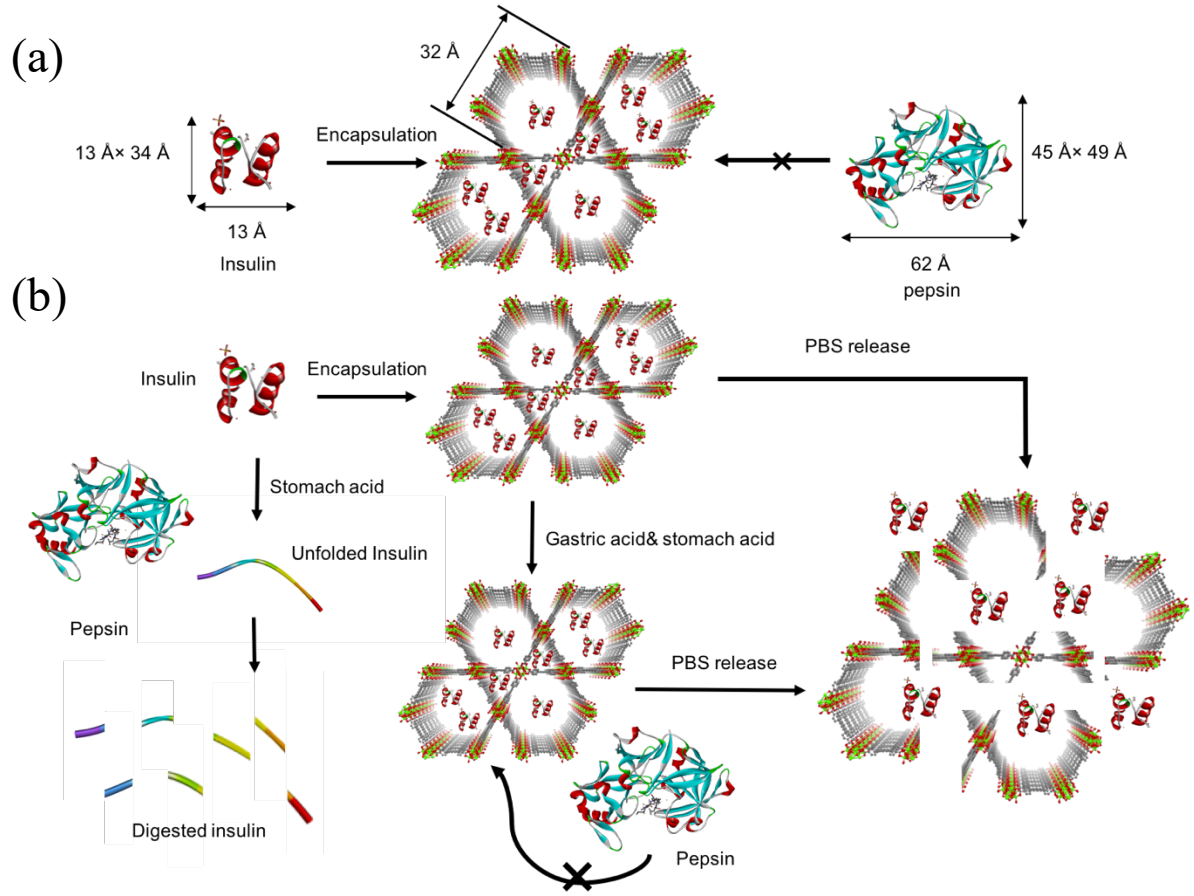

Figure 2-1 Schematic representation of (a) encapsulation of insulin in the mesopores of NU-1000 and exclusion of pepsin from the MOF framework. (b) Exposure of free insulin and insulin@NU-1000 to stomach acid. Free insulin denatures in stomach acid and is digested by pepsin. Insulin@NU-1000 releases insulin when exposed to a PBS solution. Insulin@NU-1000 withstands exposure to gastric acid and stomach acid and releases encapsulated insulin in PBS.

In this chapter, we show that NU-1000 satisfies the key requirements of an insulin delivery agent, namely sufficient porosity, favorable interactions, protection of insulin in harsh environments, and controlled insulin release. The one-dimensional pores of NU-1000 (mesopores with size ~ 30 Å and micropores with size ~12 Å in diameters) are ideally sized to not only allow insulin (13 Å × 13 Å) to diffuse through the framework facilitating encapsulation (**Figure 2-1** a), but to also exclude pepsin (48 Å × 64 Å), thereby limiting its proteolysis. Additionally, insulin molecules can be encapsulated in NU-1000 because of the electrostatic (**Figure 2-1**) and/or hydrophobic interactions between insulin and the MOF surface. Finally, when in acidic

environments like the stomach, confinement within the pores inhibits excessive insulin un-folding and significantly reduces degradation (**Figure 2-1** b). When exposed to conditions simulating the bloodstream, which is high in phosphate ions, NU-1000 is expected to slowly degrade and release the encapsulated insulin (**Figure 2-1** b). Here, we report a route to encapsulate and stabilize insulin in NU-1000, while demonstrating controlled release from the composite.

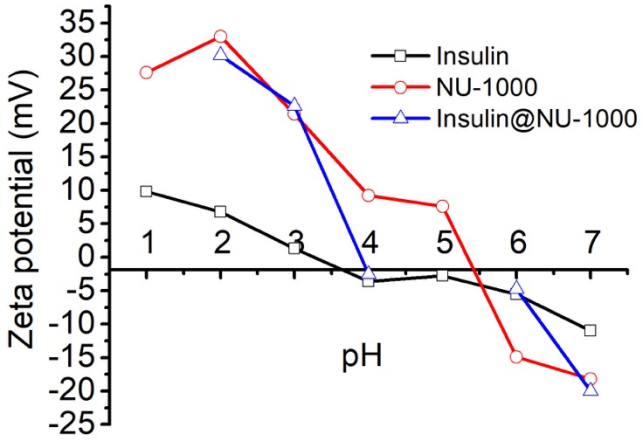

Figure 2-2 Zeta potentials of insulin, NU-1000 crystals and inslin@NU-1000 in different conditions.

2.2 Experimental Methods

2.2.1 Material Syntheses

NU-1000 was synthesized and activated according to a report-ed procedure.[67] All other reagents were purchased from commercial sources and used without further purification.

2.2.2 Physical Methods

Inductively coupled plasma-optical emission spectroscopy (ICP-OES) was used to determine the ratio of Zr (Zr nodes in NU-1000) to S (disulfide bonds in insulin) in insulin@NU-1000 to confirm the highest loading of insulin in NU-1000. The experiment was performed on a computer-controlled (QTEGRA software v. 2.2) Thermo iCap 7600 Duo ICP-OES (Thermo Fisher

Scientific, Waltham, MA, USA) operating in standard mode. The insulin@NU-1000 samples (2-3 mg) were digested by an acidic solution (vHNO3:vH2O2 = 3:1) by heating in a Biotage (Uppsala, Sweden) SPX microwave reactor (software version 2.3, build 6250) at 150 °C for 5 minutes. The solution was then diluted with Millipore water and analyzed for S and Zr content comparing to the standard S and Zr solutions. N_2 sorption isotherm measurements were performed on a Micromeritics Tristar II 3020 (Micromeritics, Norcross, GA) at 77 K. Between 30 and 50 mg of material was used for each measurement. Powder X-ray diffraction (PXRD) data were collected on a Rigaku model ATX-G diffractometer equipped with a Cu rotating anode X-ray source. Scanning electron microscopy (SEM) images and energy dispersive spectroscopy (EDX) profiles were collected on a Hitachi SU8030. Samples were coated with OsO4 to ~7 nm thickness in a Denton Desk III TSC Sputter Coater (Moorestown, NJ) before SEM-EDX analysis. Confocal laser scanning microscopy analysis (CLSM) was performed on 10μm-long NU-1000 crystals to examine the distribution of AlexaFluor-647 dye labeled insulins throughout the matrix. Fluorescence was examined, applying CLSM on a Leica TCS SP5. The Ar laser was set to 5%. Bit depth was set to 12 to achieve 4096 grey levels intensity resolution. Laser line 633 with 3% laser power was used to visualize AlexaFluor-647 dye labeled insulins on NU-1000 at different depth along z direction. ELISA test for the insulin concentration was performed following the manual in the ELISA Insulin Kit and the results were determined by UV-vis.

2.2.3 Zeta Potential and DLS Size Distribution

Samples were prepared in 10^{-3} 1×Tris buffer at a concentration of 0.1 mg/mL and sonicated for 15 min. The pH from 1 to 7 of the solution was manually adjusted by the addition of gastric acid to 10-15 mL of the suspension before the zeta potential and DLS size distribution was measured.

2.2.4 Insulin Encapsulation

Insulin647 encapsulation with NU-1000: 3mg of activated NU-1000 crystals were treated with labeled insulin solution (in DI water, 1 mg/mL) for 1 hour at room temperature to encapsulate insulin. Insulin loading was monitored by testing the concentration of labeled insulin through UV-vis.

Human insulin encapsulation with NU-1000: 3mg of activated NU-1000 crystals were treated with an insulin solution (in DI water, 4×10^{-4}g/L) for 1 hour at room temperature to encapsulate insulin. Insulin loading was measured by Inductively coupled plasma-optical emission spectroscopy (ICP-OES) and thermogravimetric analyses (TGA). To remove the insulin attached to the surface of NU-1000, the supernatant was decanted and the solid sample was then washed with DI water for three times to remove the insulin molecules attached to the surface of the crystals. Insulin loading was calculated by:

$$loading = \frac{weight\ of\ encapsulated\ insulin\ molecules}{weight\ of\ the\ encapsulating\ material} \times 100\%$$

Thermogravimetric analyses (TGA) were performed on a TGA/DCS 1 system (Mettler-Toledo AG, Schwerzenbach, Switzerland), which runs on a PC with STARe software. Samples were heated from 25 to 600 °C at a rate of 10 °C/min under flowing N_2. The elemental analysis was performed by Galbraith laboratories, Inc (Knoxville, Tennessee). The loading of insulin@NU-1000 was calculated with the following method:

$$loading = \frac{28\%}{72\%} \times 100\% = 38.9\%$$

Molar ratio (Insulin:NU-1000) = $1.0: 7.0$

Mass Ratio (Insulin:NU-1000) = $5808: 15191$

wt% (mass insulin: mass support) ≈ 40%

2.2.5 The Degradation of NU-1000 and Release of Insulin647 in PBS

1mg of bare NU-1000 or insulin647@NU-1000 was exposed to 1ml 1g/L K_3PO_4 solution (pH=7.0). The supernatant was replaced by fresh 1g/L K_3PO_4 solution every 10 min to mimic the constant flowing blood plasma. The UV-vis absorbance of the replaced supernatant was measured and the released percentage of linkers/insulin647 over time was calculated based on the standard curves.

2.3 Results and Discussion

MOF crystals (2 μm in length, **Figure 2-1**) were soaked in an insulin solution (4×10^{-4} g/L in DI water at pH 4) for 30 minutes at room temperature to encapsulate the protein. The resulting solid composite, insulin@NU-1000, was isolated by filtration and washed with DI water to remove excess insulin. Dye (AlexaFluor-647) labeled insulin (insulin647) was encapsulated in NU-1000 and its uptake was observed by in situ confocal laser scanning microscopy (CLSM, **Figure 2-1**) and quantified by monitoring the concentration of insulin647 in the supernatant by UV-vis spectroscopy (**Figure 2-1** a). The highest loading was achieved after the MOF was exposed to the insulin647 solution for 30 min (**Figure 2-1** b). Inductively coupled plasma-optical emission spectroscopy (ICP-OES) was used to determine the S (3 disulfide bonds per insulin molecule) to Zr (from NU-1000) ratio for insulin@NU-1000 (**Error! Reference source not found.**). NU-1000 e xhibits a loading capacity of 40 wt% which exceeds most of the previously reported insulin encapsulation materials.[40] Mass loss as observed by thermogravimetric analysis (TGA) was also in agreement with the insulin loading (**Figure 2-1**) determined by ICP. These results suggest that NU-1000 is a potential insulin encapsulation agent.

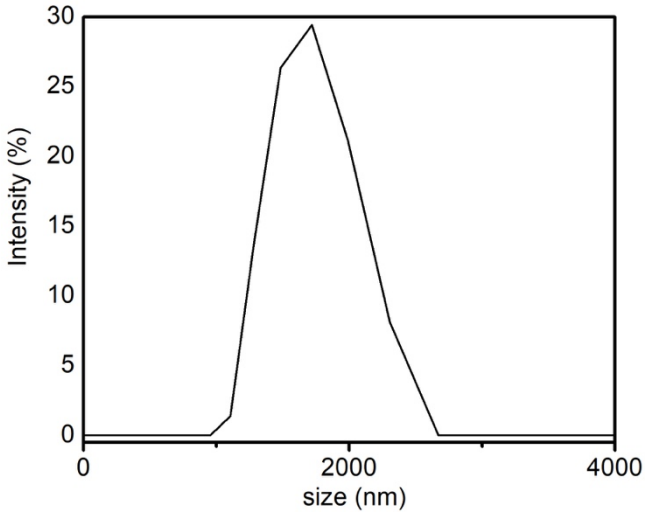

Figure 2-3 Size distribution of NU-1000 crystals.

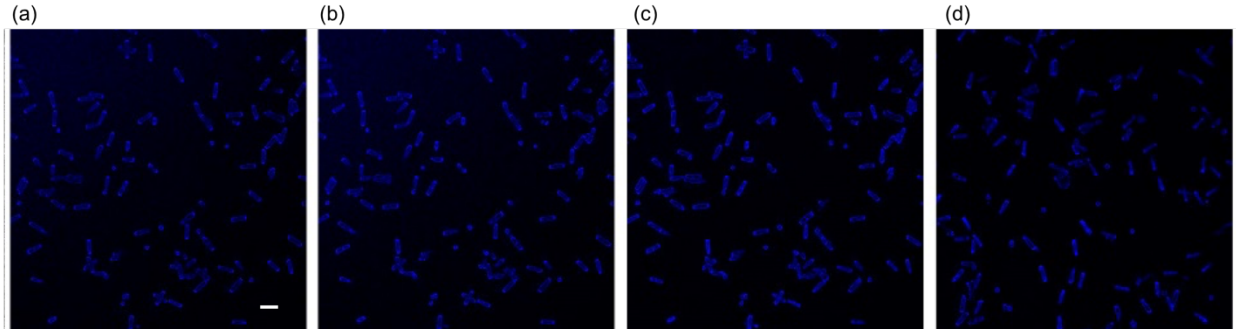

Figure 2-4 Confocal laser scanning microscopy images of labeled insulin@10 μm NU-1000 crystals. The scale bar stands for 10 μm. Figure (a)-(d) indicate the distribution of insulin in the NU-1000 crystals at 10 min, 15 min, 20 min, and 30 min respectively.

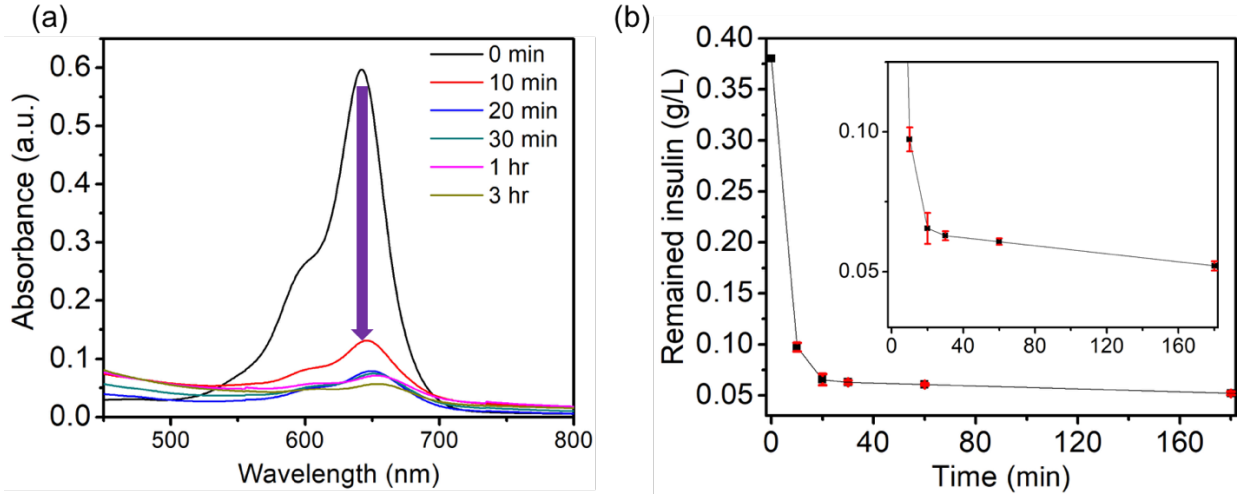

Figure 2-5 (a) UV-vis spectra used to monitor the insulin647 concentration in the supernatant at various timepoints after adding NU-1000. (b) The adsorption of insulin647 in NU-1000 crystals (inset: adsorption process from 10 to 60 min).

Table 2-1 ICP-OES data for insulin@NU-1000.

						NU1000 insulin
S 180.731 {486} (Axial) [ppm]	0.000	0.499	0.253	0.126	0.060	1.653
S 182.034 {485} (Axial) [ppm]	0.000	0.498	0.252	0.127	0.061	1.646
S 182.624 {484} (Axial) [ppm]	0.000	0.497	0.252	0.130	0.066	1.599
Zr 339.198 {99} (Axial) [ppm]	0.000	0.500	0.251	0.124	0.061	31.238
Zr 343.823 {98} (Axial) [ppm]	0.000	0.500	0.250	0.125	0.062	31.767
Zr 327.305 {103} (Axial) [ppm]	0.000	0.499	0.252	0.125	0.063	33.682
Zr 349.621 {96} (Axial) [ppm]	0.000	0.500	0.252	0.124	0.061	32.852

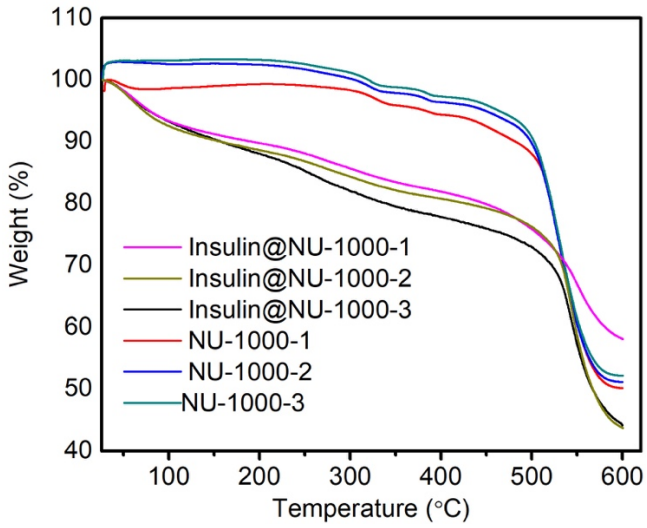

Figure 2-6 Thermogravimetric analysis of NU-1000 crystals and insulin@NU-1000.

The insulin@NU-1000 material was fully characterized via nitrogen adsorption/desorption measurements, powder X-ray diffraction (PXRD), and scanning electron microscopy (SEM). As expected, the N_2 isotherm indicates that insulin@NU-1000 has a lower N_2 uptake capacity and therefore lower surface area than the parent NU-1000 (**Figure 2-7**a). Further, the density function

theory (DFT) calculated pore size distribution reveals a significant reduction of the hexagonal mesopore volume and a smaller, but still significant, decrease for the triangular micropore volume (**Figure 2-7** b). This suggests that insulin resides in both pores. PXRD patterns and SEM images verify that NU-1000 retains its crystallinity throughout the encapsulation process (**Figure 2-7** c). Furthermore, SEM dispersive X-ray spectroscopy (SEM-EDX) indicates insulin is uniformly distributed throughout NU-1000 crystals (**Figure 2-7** d).

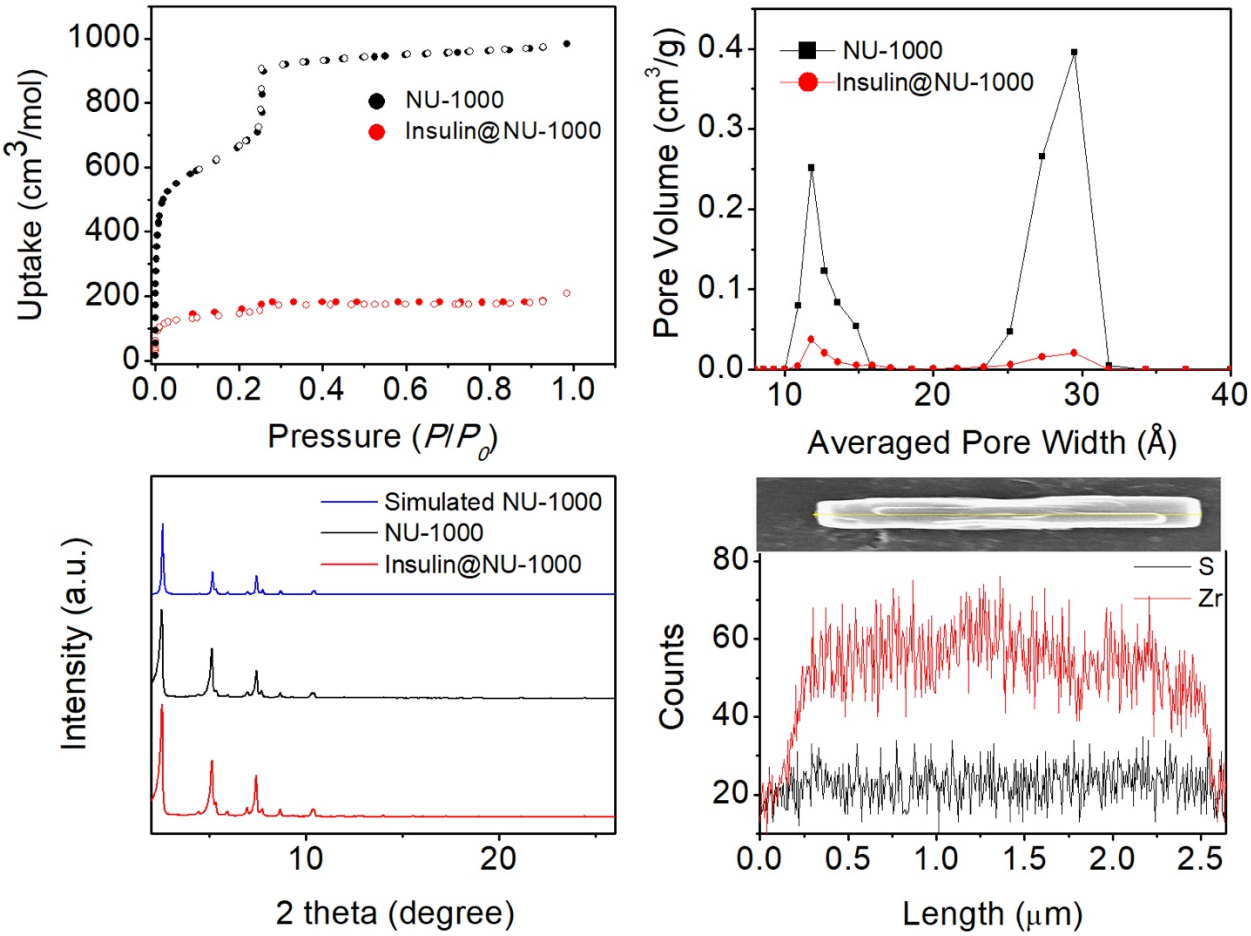

Figure 2-7 (a) N_2 adsorption-desorption isotherms reveal significant surface area reduction after encapsulation of insulin. (b) DFT pore size distributions of NU-1000 (black) and insulin@NU-1000 (red) suggest insulin occupies both the meso-pores and micropores. (c) PXRD patterns of NU-1000, simulated NU-1000, and insulin@NU-1000 confirm the retention of crystallinity. (d) SEM image and associated EDX line scan for Zr (red) and S (black) which confirms uniform distribution of insulin throughout crystal in insulin@NU-1000.

While high loading capacities are desirable, it is also vital that the delivery agent effectively protects insulin from harsh conditions and releases the insulin only in the target environment. The insulin release process was examined by exposing insulin@NU-1000 samples to solutions designed to emulate conditions that an orally delivered insulin drug may encounter. Specifically, samples were exposed for 1 hour to one of the following: gastric acid solution (pH = 1.29) (simulating the stomach pH or simulated physiological condition (pH=7.0) (**Figure 2-8** a). The amount of insulin released was again quantified by analyzing the concentration of labeled insulin in the supernatant by UV-vis spectroscopy after exposure to the aforementioned conditions. In simulated stomach acid solution (pH = 1.29), only 10% of insulin was released after 60 min. This suggests that insulin encapsulated in NU-1000 is protected from the harsh conditions of the stomach. Additionally, after the exposure to the simulated physiological condition, NU-1000 degradation initiates the release of insulin. After 1 h, most of the encapsulated insulin (91%) is released from insulin@NU-1000. The degradation of NU-1000 crystals was monitored by measuring the concentration of linker in the supernatant via UV-vis spectroscopy (**Figure 2-8**). In conditions designed to simulate the stomach environment (gastric acid and pepsin as used in the aforementioned experiments), NU-1000 crystals remained stable for at least 1 h. On the contrary, in the simulated physiological condition, NU-1000 starts to degrade immediately. After 1 h, 10% of the total linker was released. These results are promising considering insulin is protected in environments mimicking the stomach and released in those designed to imitate the bloodstream, the target delivery point.

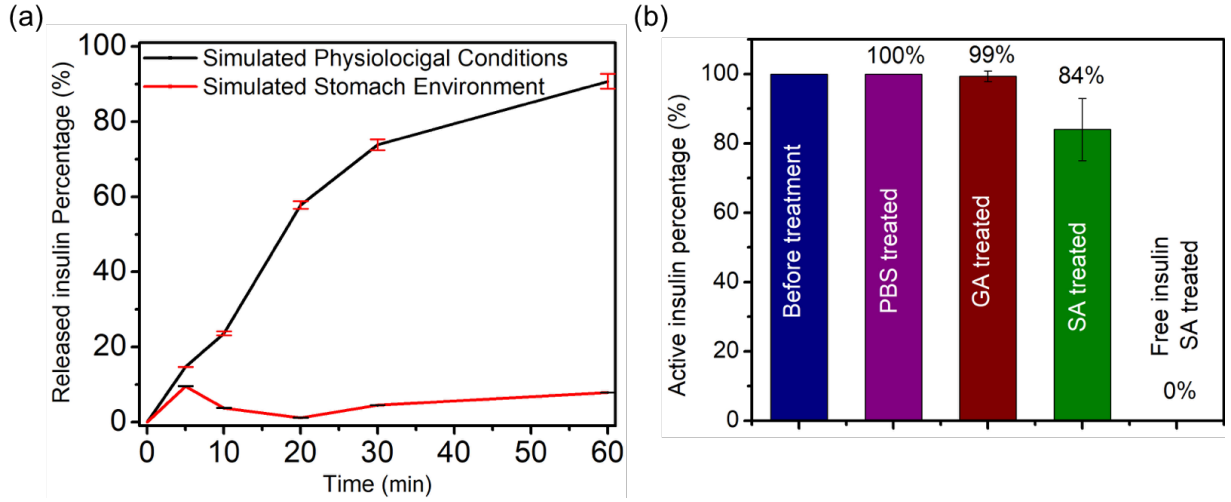

Figure 2-8 (a) The percent of encapsulated insulin released from simulated physiological condition (black) and simulated stomach acid (red). (b) The concentration of active insulin after loading, and treatment under various harsh conditions. The black column shows the original concentration of active insulin in solution. The red areas show the amount of active insulin released from insulin@NU-1000 after different treatments (GA for gastric acid and SA for stomach acid).

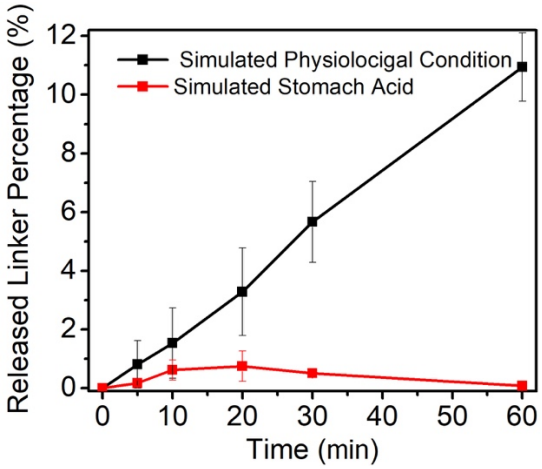

Figure 2-9 The percent of linker released from NU-1000 in simulated physiological condition (black) and simulated stomach acid (red).

Considering insulin is only an effective therapeutic agent when in its active form (i.e. not denatured or digested), an enzyme-linked immunosorbent assay (ELISA) was employed to determine the concentration of insulin after release from the framework and to further evaluate the effect of release conditions on insulin activity (**Figure 2-8** b). The initially encapsulated insulin was assumed to be entirely active prior to re-lease from insulin@NU-1000. As expected,

when exposed to stomach acid, free insulin does not survive as measured by ELISA, confirming the necessity of an encapsulation method if insulin must pass through the stomach. When insulin@NU-1000 was exposed to PBS, the released protein retains its full activity. Further, insulin released from insulin@NU-1000 samples first exposed to gastric acid or stomach acid solutions followed by exposure to a PBS solution also retained the majority of its activity (99% for gastric acid and 84% for stomach acid). These results suggest insulin@NU-1000 can withstand the low pH environment of the stomach and release insulin in the desired environment. The high concentrations of insulin observed via ELISA even after exposure to such harsh conditions further demonstrates the ability of NU-1000 to protect insulin. It is evident that NU-1000 stabilizes and protects insulin under denaturing conditions encountered in the stomach (gastric acid or stomach acid solutions) and releases the encapsulated insulin under conditions mimicking the delivery target point, the blood-stream (PBS solution).

2.4 Conclusions

In conclusion, we successfully utilized the zirconium MOF, NU-1000, as an insulin carrier and achieved high loading of insulin. Under mild conditions, insulin easily diffuses through the framework and interacts favorably with the pore surface, leading to rapid encapsulation. Further, insulin@NU-1000 withstands harsh conditions mimicking the stomach environment while releasing insulin in conditions that imitate the ideal release environment, the bloodstream. Most importantly, upon being released from insulin@NU-1000, insulin maintains the majority of its activity. These results demonstrate that NU-1000 is a potential insulin carrier for oral delivery.

Chapter 3 . DNA-Functionalized Metal−Organic Framework Nanoparticles for Intracellular Delivery of Proteins

Portions of this chapter appear in the following manuscript:

Wang, S., Chen, Y., Wang, S., Li, P., Mirkin, C. A., & Farha, O. K. DNA-Functionalized Metal–Organic Framework Nanoparticles for Intracellular Delivery of Proteins. *JACS*, **2019**, *141(6)*, 2215-2219.

Contribution:

For the paper, **Chen,Y.** conducted all the MOF synthesis, insulin encapsulation and release characterization. DNA modification, post-modification characterization was conducted by Wang. S.. Wang. S. has performed the cell uptake characterizations as well as the tocxicity tests. Other co-authors have contributed to constructive scientific discussions and hence are listed as part of the co-author list.

3.1 Introduction

Proteins play key roles in living systems, and the ability to diagnostic and therapeutic purposes.[68] Potential uses involve the evaluation of metabolic pathways,[69] regulation of cellular processes,[70] and treatment of disease involving protein deficiencies.[71-73] During the past decade, a series of techniques have been developed to facilitate protein internalization by live cells, including the use of complementary transfection agents, nanocarriers,[74-76] and protein surface modifications.[77-80] Although each strategy has its own merit, none are perfect solutions; they can cause cytotoxicity, reduce protein activity, and suffer from low delivery payloads.[81] For example, we have made the observation that one can take almost any protein and functionalize its surface with DNA to create entities that will naturally engage the cell-surface receptors involved in spherical nucleic acid (SNA) uptake.[80, 82-84] While this method is extremely useful in certain situations, it requires direct modification of the protein and large amounts of nucleic acid, on a per-protein basis, to effect transfection. Ideally, one would like to deliver intact, functional proteins without the need to chemically modify them, and to do so in a nucleic-acid efficient manner.

Metal organic frameworks (MOFs) have emerged as a class of promising materials for the immobilization and storage of functional proteins.[24] Their mesoporous structures allow for exceptionally high protein loadings, and their framework architectures can significantly improve the thermal and chemical stabilities of the encapsulated proteins.[61, 63, 85-88] However, although MOF NPs have been recognized as potentially important intracellular delivery vehicles for proteins,[89-91] their poor colloidal stability and positively charged surfaces,[92-93] inhibit their cellular uptake and have led to unfavorable bioavailabilities.[94-97] Therefore, the development of

general approaches for reducing MOF NP aggregation, minimizing positive charge (which can cause cytotoxicity), and facilitating cellular uptake is desirable.[98-99]

In this chapter, we report a new method for the intracellular delivery of proteins that relies on nucleic acid−MOF NP conjugates (**Figure 3-1** A).[98-101] In this protocol, two water-stable zirconium mesoporous MOFs, NU-1000 ($Zr_6(\mu_3\text{-}O)_4(\mu_3\text{-}OH)_4(OH)_4(H_2O)_4(TBAPy)_2$, H_4-TBAPy = tetraethyl 4,4′,4″,4‴-(pyrene-1,3,6,8-tetrayl)tetrabenzoic acid) and PCN-222/MOF-545 ($Zr_6(\mu_3\text{-}O)_4(\mu_3\text{-}OH)_4(OH)_4(H_2O)_4(TCPP\text{-}H_2)_2$, H_4-TCPP-H_2 = tetrakis(4-carboxyphenyl)porphyrin),[102-104] were synthesized in nanoparticle form and used to encapsulate insulin, a model protein for the studies described herein (**Figure 3-1**B).[54, 105] Next, via modification of literature procedures, these insulin@MOF NPs were surface functionalized with terminal phosphate-modified DNA to yield insulin@DNA-MOF NPs (**Figure 3-1** C).[100] The 3D oligonucleotide shell creates a steric and electrostatic barrier to stabilize MOF NPs in high dielectric media and renders them functional with respect to cellular entry.[98] In principle, this strategy can be generalized to MOFs with different pore sizes and topologies, thereby creating an arsenal of nucleic acid−MOF-based delivery vehicles for transporting functional enzymes across cellular membranes with high payloads.

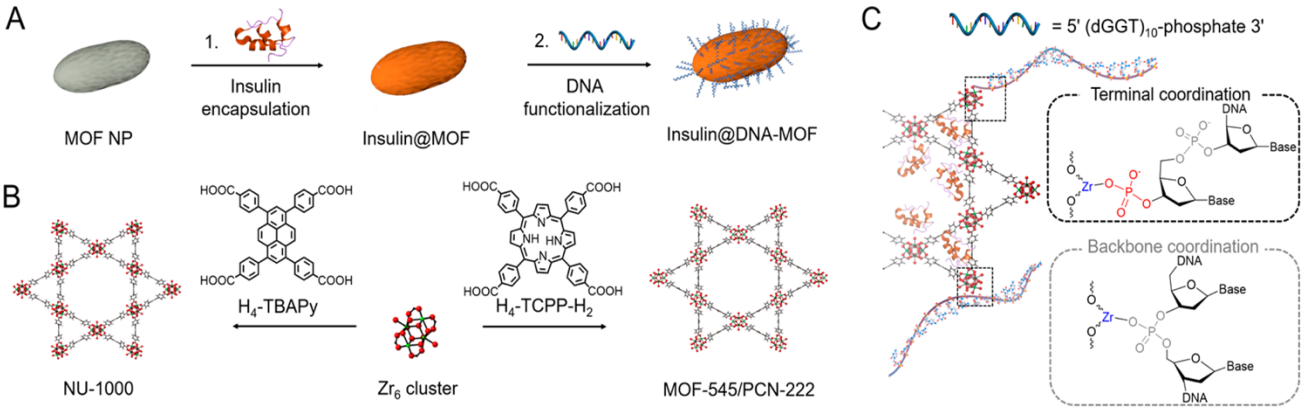

Figure 3-1 (A) Schematic illustration of insulin encapsulation in the mesoporous channels of MOF NPs followed by DNA surface functionalization; (B) crystal structures of two mesoporous Zr MOFs: NU-1000 and PCN-222/MOF-545 and their respective organic linkers; (C) DNA

functionalization of insulin encapsulated MOF NPs using 3′ terminal phosphate modified nucleic acids.

3.2 Experimental Methods

3.2.1 Material Syntheses

All reagents unless otherwise stated were obtained from commercial sources and were used without further purification. All oligonucleotides used in this work were synthesized on a solid-support MM12 synthesizer with reagents purchased from Glen Research. The water used in all experiments was ultrapure deionized (DI) grade (18.2 MΩ·cm resistivity), obtained from a Milli-Q Biocel system (Millipore, Billerica, MA, USA).

Synthesis of 150 nm NU-1000 MOF NPs. 8 mg (34.3nmol) of zirconium chloride and 2 mg (3 nmol) of 1,3,6,8-tetrakis(p-benzoic acid)pyrene (H4TBAPy) ligand were dissolved in 2.0 mL of N,N-Dimethylformamide (DMF), 0.4 ml acetic acid and 0.2 ml DI water was also added to the mixture solution resulting in a translucent yellow solution. Ten sample vials were prepared under the same conditions at once and were placed into an oven at 90 °C for 30 min, during which time a light yellow suspension was formed. After cooling down to room temperature, the 10 vials were combined and the nanocrystals were collected by centrifugation (15000 rpm, 30 min), followed by solvent exchange with DMF and acetone third times, then subsequently activated with HCl.

Synthesis of 10 μm NU-1000 MOF particles. 70 mg of $ZrCl_4$ (0.30 mmol) and 2700 mg (22 mmol) of benzoic acid were mixed in 8 mL of *N,N*-Diethylformamide (DEF) (in a 6-dram vial) and ultrasonically dissolved. The clear solution was incubated in an oven at 80 °C for 1h. After cooling down to room temperature, 40 mg (0.06 mmol) of H_4TBAPy was added to this solution and the mixture was sonicated for 20 min. The yellow suspension was heated in an oven at 120 °C

for 48 h. After cooling down to room temperature, yellow single crystals were present on the vial walls. The sample was washed with DMF and acetone and subsequently activated with HCl.

Synthesis of PCN-222 MOF NPs. Zirconyl chloride octahydrate (37.5 mg, 0.116 mmol) and tetrakis(4- carboxyphenyl)-porphyrin (6.5 mg, 0.0082 mmol) were dissolved in DMF (16.25 mL) in a 22 mL borosilicate vial with a Teflon-lined cap. Dichloroacetic acid (0.25 mL, 3.0 mmol) was added, and the resulting solution was heated at 130 °C for 18 hours to afford dark purple rod-shaped nanocrystals and a yellow mother liquor. The nanocrystals were collected by centrifugation (15000 rpm, 5 min), followed by solvent exchange with DMF.

3.2.2 Physical Methods

The crystallinity of the MOF nanoparticles (as-synthesized, insulin encapsulated, and insulin encapsulated DNA-MOF conjugates) were confirmed by powder X-ray diffraction (PXRD). Powder X-ray diffraction (PXRD) data were collected on a Rigaku model ATX-G diffractometer equipped with a Cu rotating anode X-ray source. N_2 sorption isotherm measurements were performed on a Micromeritics Tristar II 3020 (Micromeritics, Norcross, GA) at 77K. Between 20 and 30 mg of material was used for each measurement. Surface areas were estimated by applying the Brunauer– Emmett–Teller (BET) equation. T-plot internal and external surface area were determined by Harkins and Jura equation in the second linear regions of N_2 isotherms (0.26 P/P_0 to 1.0 P/P_0).

3.2.3 Insulin Encapsulation

Activated MOF nanoparticles (3 mg) were treated with an insulin solution (in DI water, 0.4 mg/mL) for 1 hour at room temperature to encapsulate insulin. Insulin loading was measured by Inductively coupled plasma-optical emission spectroscopy (ICP-OES) and thermogravimetric analyses (TGA) based on literature reported methods.[105] To remove the insulin attached to the

surface of MOF NPs, the supernatant was decanted and the solid sample was then washed with DI water for three times to remove the insulin molecules attached to the surface of the crystals.

3.2.4 DNA Synthesis and Functionalization

Synthesis of oligonucleotides. Oligonucleotides were synthesized using a Mermaid MM12 DNA synthesizer (Bio Automation) on a standard CPG solid phase support. All oligonucleotides were deprotected under conditions recommended by the manufacturer and purified by reverse phase high performance liquid chromatography (HPLC). Characterization and determination of concentrations were determined by matrix assisted laser desorption ionization (MALDI-TOF) mass spectrometry and UV-Vis spectroscopy, respectively.

Table 3-1 DNA sequences used in this study.

#	Sequence Name	Sequence
1	polyG	5' - $(dGGT)_{10}$-phosphate - 3'
2	polyG-dye	5' - (Tamra-dT)-$(dGGT)_{10}$-phosphate - 3'

3' Phosphate refers to 3-(4,4'-Dimethoxytrityloxy)-2,2-(dicarboxymethylamido)propyl-1-O-succinoyl-long chain alkylamino-CPG (3'-CPR II CPG).

Tamra-dT refers to 5'-Dimethoxytrityloxy-5-[N-((tetramethylrhodaminyl)-aminohexyl)- 3-acrylimido]-2'-deoxyUridine-3'-[(2-cyanoethyl)-(N,N-diisopropyl)]-phosphoramidite (Tamra-dT).

DNA functionalization. DNA functionalization of MOF NPs were conducted based on our previously reported method with minor modifications.[100] In a typical DNA functionalization experiment, excess phosphate terminated nucleic acid (~ 100 nmol) was added to MOF NP colloids (~2 mg), and then left on a shaker to incubate for 4 hours. Excess oligonucleotides were removed by centrifugation (3 × 10000 rpm, 15 min), and followed by resuspension in water.

3.2.5 Degradation Profiles of DNA-NU-1000 and DNA-PCN-222

Degradation profile in simulated extracellular matrices. To simulate intravascular and interstitial fluid, MOF NPs were incubated with DMEM buffer + blood serum (pH = 7.0) at 37 °C with gentle shaking (400 rpm). Specifically, around 50 ug of DNA-NU-1000 and DNA-PCN-222 were first dispersed in 200 uL water to form the stock solution (0.25 mg/mL). Next, 7 identical samples containing 20 uL of the stock solution and 980 uL (DMEM buffer + blood serum solution) (pH=7.0) were prepared and incubated on a thermal shaker for 0.5, 1.5, 6, 12, 24, 48, and 72 hours, repectively. At each time point, one sample was collected and centrifuged (15000 rpm, 15 min) to remove remaining MOF NPs. The UV-vis absorbance of supernatant was measured and the percentage of linker release over time was calculated based on the standard curves.

Degradation profile in simulated intracellular matrices. Similar procedure was followed to measure the degradation profiles of DNA-NU-1000 and DNA-PCN-222 in 1 × PBS solution to simulate their degradation in intracellular matrices (pH=7.0, 100 mM NaCl).

3.2.6 Cell Uptake Experiments and Cytotoxicity Evaluation

Cell culture and incubation. Human ovarian cancer cells SK-OV-3(ATCC® HTB-77™) and mice melanoma cells B16-F10 (ATCC® CRL-6475) were incubated in incubators with 5% CO_2 at 37 °C. Medium for these two cell lines are McCoy's 5A medium (ATCC® 30-2007™) and Dulbecco's Modified Eagle's Medium (DMEM) (ATCC® 30-2002™), representatively, containing 10% fetal bovine serum (FBS) and 1% antibiotics. Cells are passed every 2 or 3 days to get the acceptable confluence.

Cell imaging by confocal fluorescence microscopy. Confocal fluorescence microscopy was performed on confocal laser microscope (Zeiss LSM 800) system to verify that insulin@DNA-MOF NPs were internalized by the cells. SKOV-3 cells were plated in flourishes with 5×10^4 confluence. Insulin-encapsulated MOFs and free insulin were then incubated with

cells (**Error! Reference source not found.**). After 6h, particles in medium were washed out and c ells were fixed with 4% formaldehyde. Cell skeleton actin (F-actin) was stained with AlexaFluor 488 Phalloidin (ThermoFisher A12379).

Table 3-2 DNA and insulin concentration for sequences used in this study.

#	Description	DNA concentration	Insulin concentration
1	AF647Insulin@ tamra-DNA-NU-1000	100 nM	~ 180 nM
2	AF647Insulin@tamra-DNA-PCN-222	100 nM	~ 140 nM
	Tamra-DNA	100 nM	
3	AF647Insulin		160 nM

Cellular Uptake by flow cytometry. LSR-II flow cytometry machine is used to identify the celluar uptake of both oligonucleotide and insulin. Skov-3 cells were first inculabed in flow tubes with 5×10^5 concentration. Then insulin@DNA-MOFs, and control (free insulin + free DNA) were then incubated with cells (Table S-2). After 15 min or 2h, particles were washed out and cells were fixed with 4% formaldehyde. Flow data were first gated by SSA and FSA parameter and positive gating in each channel is based on negative controls.

MTT assay. The anti-proliferative effects of insulin@DNA-MOF constructs were evaluated by MTT assay. Specifically, B16-F10 cells were seeded in a 96-well cell culture plate in DMEM medium at a density of 5×10^4 cells/mL with 10% fetal bovine serum (FBS) and 5% CO_2 at 37 °C for 24 h. Next, the culture medium was replaced by 200 μL of DMEM medium containing samples at different concentrations (with non-labelled DNA and insulin) and cultured for 72h. Then, 10 μL of 5 mg/mL MTT solution (10% SDS) was added to each cell well. The cells were further incubated for 4 h, followed by removal of the culture medium with MTT. Finally, 100 μL of 10 % SDS was added and incubated overnight at 37 °C. The absorbance of MTT at 492 nm was measured on an automatic ELISA analyzer (SPR-960), with a reference absorbance at 977nm. Each experiment was conducted for 3 times and the averaged data were presented.

3.3 Results and Discussion

NU-1000 MOF NPs [180(20) × 70(10) nm] were synthesized via a solvothermal reaction of zirconium chloride ($ZrCl_4$) with H_4- TBAPy ligands, modulated by acetic acid in N,N-dimethylfor- mamide (DMF) at 90 °C (**Figure 3-2** A). Similarly, PCN-222 NPs [210(30) × 50(10) nm] were synthesized via a solvothermal reaction between zirconyl chloride octahydrate ($ZrOCl_2 \cdot 8H_2O$) and H_4-TCPP-H_2 ligands, modulated by dichloroacetic acid in DMF at 130 °C (Figure 3-2 B). Next, the thermally activated crystals of NU-1000 were treated with a bis-tris-propane buffer (BTP, pH = 7) solution of insulin (0.4 mg/mL). The MOF NP insulin encapsulation efficiencies were determined by measuring the S (for insulin) and Zr (for MOFs) contents by inductively coupled plasma-optical emission spectroscopy. The maximum insulin loadings of 34 and 63 wt % were determined for NU-1000 and PCN-222 NPs, respectively, which are consistent with our previous report.[105] The excess insulin in the supernatant was removed by sequential washing steps with DI water.

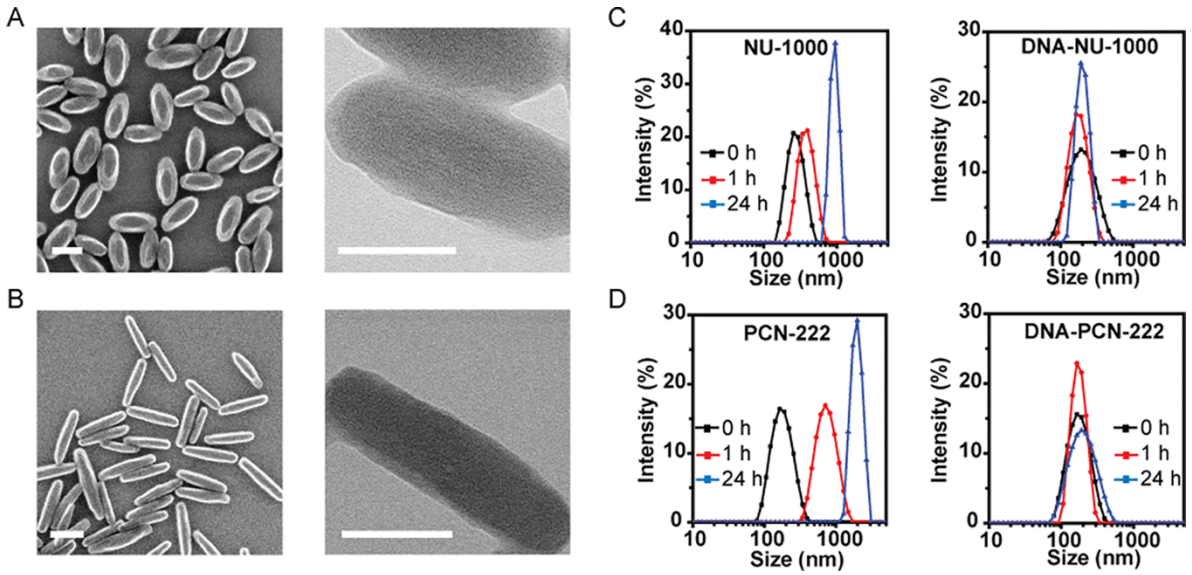

Figure 3-2 Scanning electron microscopy (left) and transmission electron microscopy (right) images of as-synthesized NU-1000 NPs (A) and PCN- 222 NPs (B). (C−D) Colloidal stability of NU-1000 and PCN-222 NPs in cell medium, as determined by DLS without (left) and with DNA surface modification (right). Scale bars = 100 nm.

The insulin@MOF NPs were functionalized with nucleic acids by coordinating the terminal phosphate-modified oligonucleotides to the surface Zr SBUs.[65, 100] The sequence used here, 5′ (dGGT)10-phosphate 3′, was chosen because it is known with SNAs that a G-rich shell, relative to poly dT shells, facilitates higher cellular uptake.[106] In a typical NP functionalization experiment, excess oligonucleotides were added to a colloidal dispersion of MOF NPs and incubated for 4 h (Supporting Information). Particle DNA coverage was quantitively determined by measuring the P to Zr ratio by ICP-OES (8 ± 1 nmol/mg for NU-1000 NPs and 10 ± 1 nmol/mg for PCN-222 NPs). Powder X-ray diffraction (PXRD) and scanning electron microscopy (SEM) confirmed that the crystallinity and morphologies of the MOF NPs were maintained, post-DNA functionalization (**Figure 3-3** and **Figure 3-4**). Importantly, dynamic light scattering (DLS) verified that DNA surface functionalization significantly increases MOF NP colloidal stability in cellular media (90% DMEM buffer +10% fetal bovine serum) for at least 24 h; for comparison, unfunctionalized NU-1000 NPs aggregated in less than 1 h, hampering further in vitro use (**Figure 3-2** C,D and EM image of aggregated NPs: **Figure 3-5**).

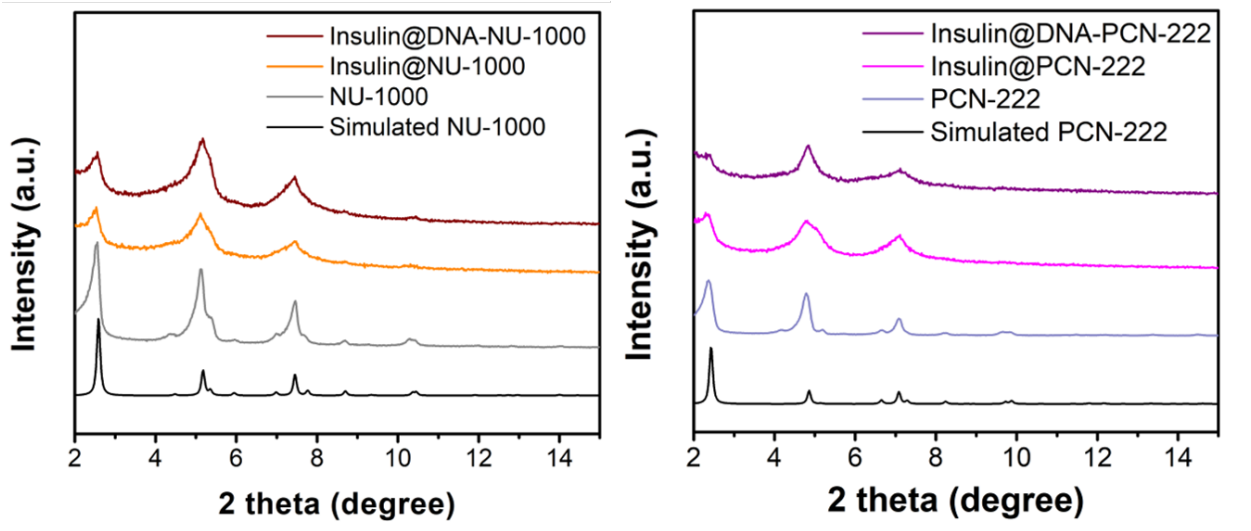

Figure 3-3 PXRD spectra of as-synthesized, insulin encapsulated, and DNA-MOF conjugates for NU-1000 and PCN-222 NPs.

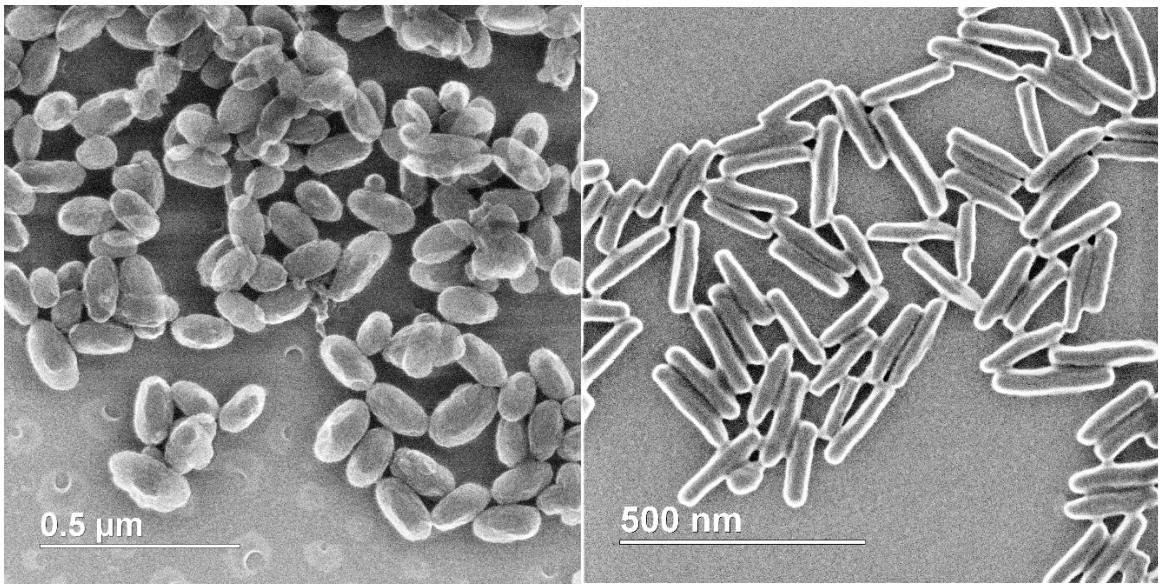

Figure 3-4 SEM images verify that the morphologies of DNA-NU-1000 (left) and DNA-PCN-222 (right) NPs are maintained post-DNA functionalization.

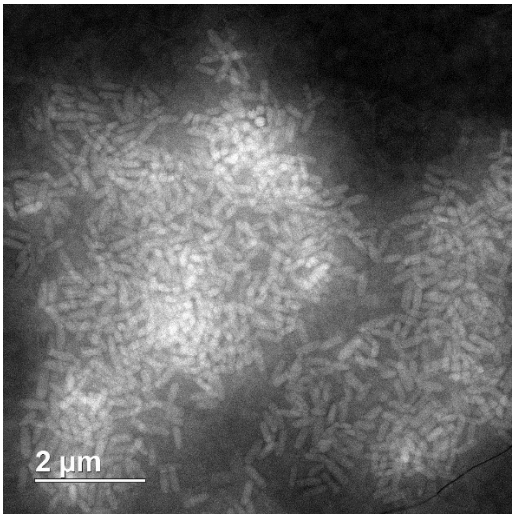

Figure 3-5 Cryo-HAADF image of insulin encapsulated PCN-222 NPs aggregated in cell medium.

In addition to colloidal stability, the intra- and extracellular stability of protein delivery vehicles in serum and serum free but biologically relevant matrices is important. Indeed, the ability to control degradation could be useful in the development of temporally controlled drug delivery applica- tions. Under physiological conditions, intracellular fluid exhibits significantly higher inorganic phosphate concentration (5−10 mM) as compared to that of serum (∼1 mM).[107-108] Therefore, the degradation profiles of insulin@DNA-NU-1000 NPs and insulin@DNA-PCN-

222 NPs were evaluated by exposing them to solutions designed to emulate both extracellular and intracellular conditions. To simulate serum, MOF NPs were incubated with 90% DMEM buffer +10% blood serum (pH = 7.0) at 37 °C with gentle shaking (400 rpm), where less than 5% of degradation occurred within 12 h for both vehicles, and less than 20% within 96 h, suggesting DNA-MOF NPs exhibit excellent stability and may be compatible with blood (**Figure 3-6** C, dashed). In contrast, when the same MOF NPs were incubated in an intracellular medium simulant (1 × phosphate buffered saline, pH = 7.0) at 37 °C with gentle shaking, the particles degrade at much faster rates (**Figure 3-6**, solid) due to the high phosphate content, which competitively binds to Zr clusters. Interestingly, DNA-PCN-222 NPs exhibit a faster degradation rate (half-life = 1 h) when compared to that of DNA-NU-1000 NPs (half-life = 40 h). Such degradation kinetics could be useful for in vivo purposes by providing a means to control the temporal release of proteins from particles, once inside cells.

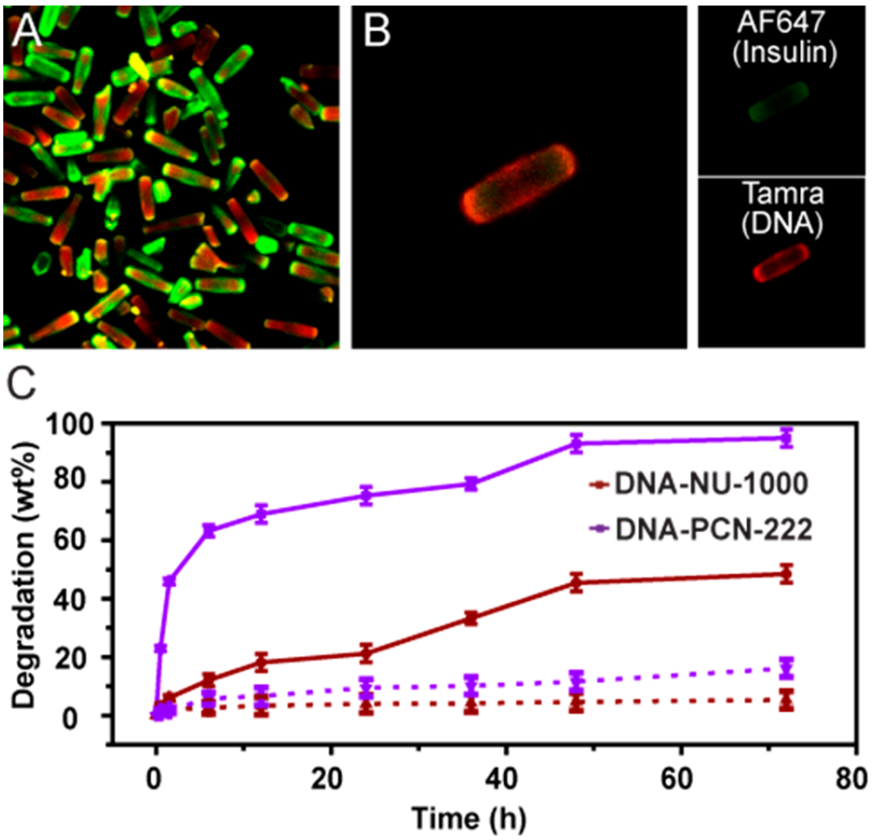

Figure 3-6 (A) Representative confocal fluorescence micrographs of 10 μm insulin@DNA-NU-1000 particles verified the colocalization of insulin (AF647 channel) and DNA (TAMRA channel). (B) Z-stack image of a single 10 μm insulin@DNA-NU-1000 crystal. (C) Degradation profiles of DNA-NU-1000 NPs and DNA-PCN-222 NPs incubated in extracellular medium (dashed lines) and in simulated intracellular medium (solid lines) at 37 °C with 400 rpm shaking.

To directly visualize nucleic acid-modified, insulin encapsulated MOF NPs, we employed confocal laser scanning microscopy to image them. Due to the resolution limits of confocal microscopy, larger particles (2.8 μm × 10 μm for NU- 1000), AlexaFluor 647 dye (AF647)-labeled insulin, and TAMRA-labeled DNA were used. With such particles, the colocalization of AF647 and TAMRA signals can be clearly observed, verifying the encapsulation of insulin and DNA surface functionalization of the MOF (**Figure 3-6** A). To obtain detailed information regarding relative distribution of insulin and DNA, Z-stack images of a single MOF particle were taken, where TAMRA signal (DNA) was observed to preferentially occupy the periphery while AF647 (insulin) was present throughout the particle (**Figure 3-6** B

and **Figure 3-7**). Brighter AF647 signals were observed at both ends of the particle as compared to the center section of the MOF, consistent with the previous observation that proteins diffuse into NU-1000 through its 1D channels.[54] Due to the large diameter of the MOF pores (3.2 nm for NU-1000 and 3.7 nm for PCN-222),[104] single stranded DNA was also expected to penetrate through the MOF pores and functionalize the internal surface, leading to fluorescence signal inside the particles. As verified by N_2 adsorption isotherms, reduced N_2 uptake capacity was observed postinsulin encapsulation for both MOFs, and further loss of porosity was observed post-DNA functionalization (**Figure 3-7**and **Figure 3-7**). Furthermore, an enzyme-linked immunosorbent assay (ELISA) was employed to determine whether insulin would leach from the MOF NP pores and/or lose catalytic activity during the DNA functionalization process. In both cases, no appreciable leaching and/or insulin activity loss was observed for insulin@DNA-NU-1000 and insulin@DNA-PCN-222 constructs (**Figure 3-7**).

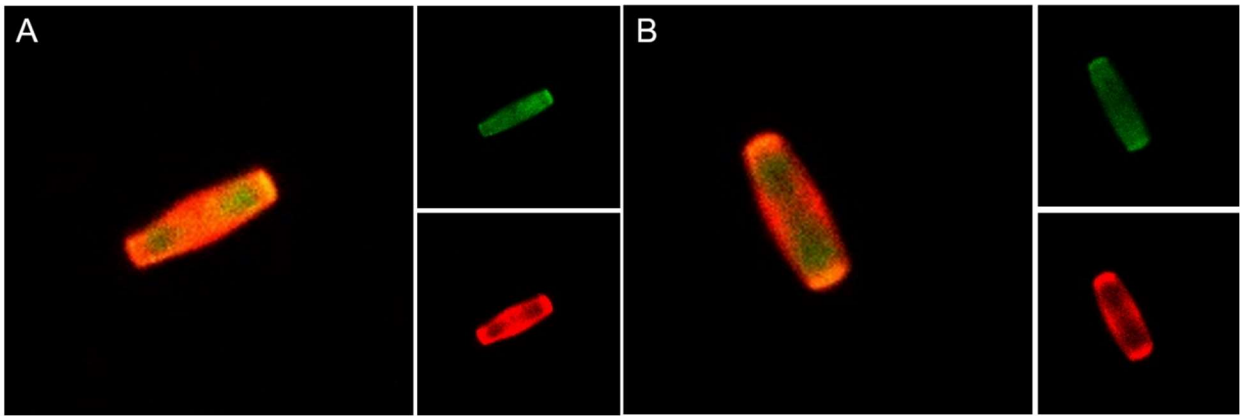

Figure 3-7 (A-B) Additional Z-stack images of individual 10 μm insulin@DNA-NU-1000 crystals. Insulin (AF647 channel: green), DNA (Tamra: red).

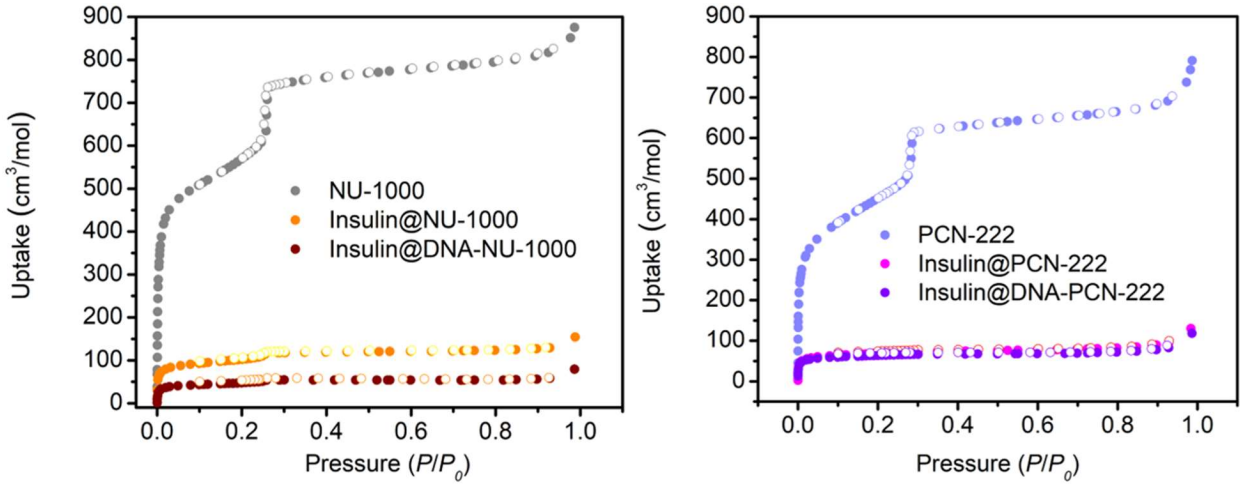

Figure 3-8 N_2 adsorption-desorption isotherms reveal significant surface area reduction post insulin encapsulation and DNA functionalization.

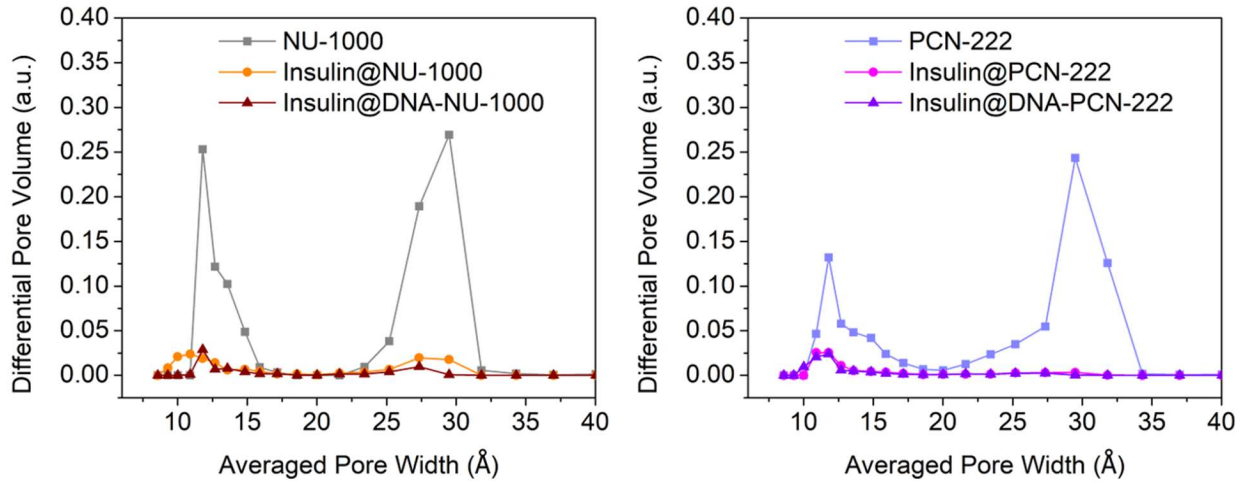

Figure 3-9 DFT pore size distributions of NU-1000 and PCN-222 suggest insulin molecules occupy both the mesopores and micropores.

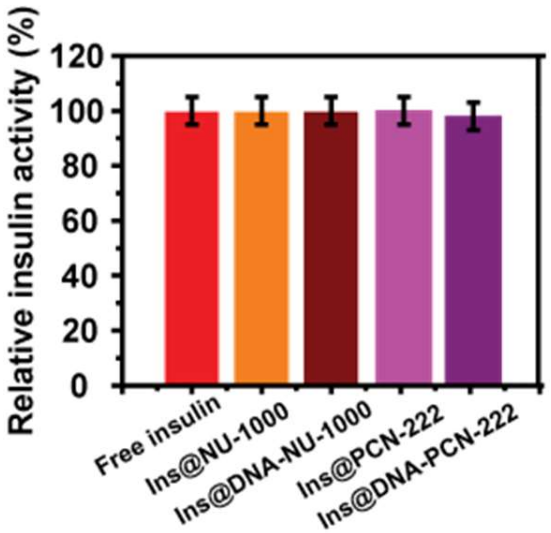

Figure 3-10 Insulin activity assay, as measured by ELISA, for native insulin (red), insulin@MOF NPs (orange for NU-1000, pink for PCN-222), and insulin@DNA-MOF NPs (brown for NU-1000, purple for PCN-222).

As previously stated, a key characteristic of SNA-NP conjugates is their ability to effectively enter cells. Therefore, we tested whether insulin@DNA-MOF NPs exhibited enhanced cellular uptake. Specifically, NU-1000 and PCN- 222 NPs were encapsulated with AF647-labeled insulin and functionalized with TAMRA-labeled DNA and incubated with human ovarian adenocarcinoma cells, SKOV-3, for 0.5, 2, 6, and 24 h. As a control group, a mixture of free TAMRA-labeled DNA and AF-647-labeled insulin was incubated with cells at the same concentration. Confocal laser scanning microscopy confirms the enrichment of insulin in cellular vesicles, as evidenced by strong colocalization of AF647 and TAMRA signals in cellular vesicles (**Figure 3-7** A−C). The Z-stack images confirm that the insulin@DNA-MOF NPs are internalized by the cells, as opposed to attached to their membranes. Consistent with this conclusion, flow cytometry showed a 10-fold increase in fluorescence in cells treated with insulin@DNA-MOF NPs as compared to those treated with the free insulin + DNA control group (**Figure 3-7** D). The insulin@DNA-MOF NPs exhibits similar levels of enhancement in cellular uptake, as compared to that of conventional SNA-NP conjugates.49 Finally, MTT assays

show that the particles result in no apparent cytotoxicity or antiproliferative effects (**Figure 3-7** E).

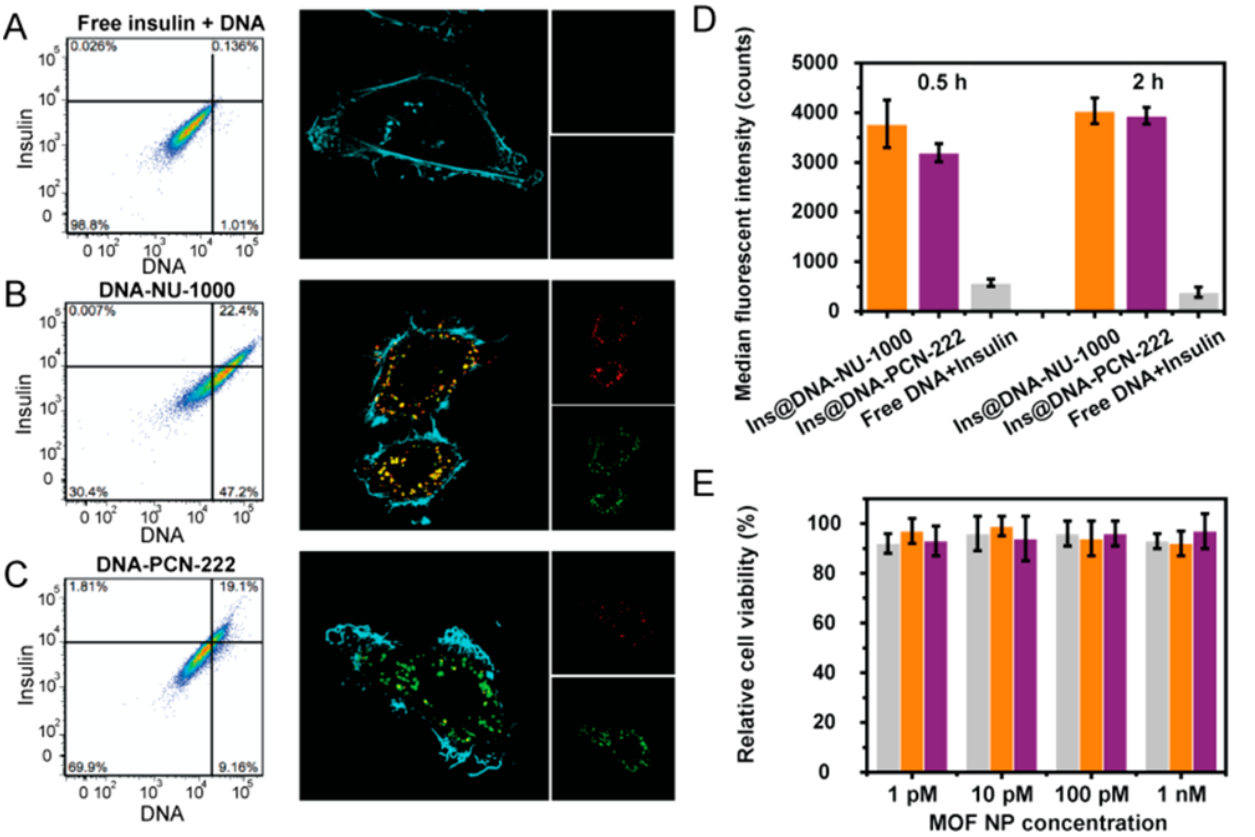

Figure 3-11 (A−C) Flow cytometry plots and confocal fluorescence micrographs of SK-OV cells after treatment with free insulin + DNA (A), insulin@DNA-NU-1000 (B), and insulin@DNA-PCN-222 (C). (D) Cellular uptake of insulin delivered in different constructs as determ ed by flow cytometry. Fluorescence at 647 nm was measured in SK-OV cells after treatment with insulin at various incubation time (0.5 and 2 h). (E) MTT assay verifies no appreciable cytotoxicity induced by insulin@DNA-PCN-222 and insulin@DNA-NU-1000 NPs. Scale bar = 10 μm.

3.4 Conclusions

In conclusion, we have developed a facile strategy for using nucleic-acid modified MOF NPs to deliver proteins across cell membranes at high payloads and negligible cytotoxicity. This work is important since it highlights how clustered surface oligonucleotides on these modular materials can be used to make them colloidally stable in physiological environments and useful for intracellular biological applications. Future design iterations will allow for encapsulating

various proteins by tuning the MOF pore sizes,[54, 58, 109] and potentially codelivery of protein and nucleic acid targets that are important for many purposes, including in vivo imaging,[69] gene regulation,[99] herapeutics,[72] and the study of fundamental cellularprocesses.

Chapter 4 . Adsorption of a catalytically accessible polyoxometalate in a mesoporous channel-type metal–organic framework

Portions of this chapter appear in the following manuscript:

Chen, Y., Li, P., Noh, H., Kung, C.W., Buru, C.T., Wang, X., Zhang, X. and Farha, O.K. Stabilization of Formate Dehydrogenase in a Metal–Organic Framework for Bioelectrocatalytic Reduction of CO_2. *Angew. Chem. Int.* **2019**, *131(23)*, 7764-7768.

4.1 Introduction

Owing to the rising awareness of environmental change, methods have been developed to combat the growing emission of greenhouse gas; the major component of which is CO_2.[110-112] Regarding the diminution of atmospheric CO_2, the primary technologies, namely physicochemical adsorption[113-115] followed by the injection into deep oceans and geological formations,[116] are limited by the poor recyclability of the currently employed adsorbents and the enormous space and cost requirements, respectively.[112, 117] Alternatively, biological fixation of CO_2 is an efficient and feasible route.[118] However, the instability of enzymes in non-biological environment and the high cost and consumption of cofactors greatly hinder the development of this technology. Thus, enhancing enzymatic reactions achieved by enzyme stabilization as well as cofactor regeneration with an economic source of energy (e.g. electrochemical, photochemical) will provide a more sustainable technology to mitigate excess CO_2.[119-122]

Enzyme stabilization through encapsulation in a porous material has been demonstrated to preserve the enzyme structure while minimizing leaching,[59, 123-126] commonly observed when enzymes are immobilized through other methods.[127-130] Metal–organic frameworks (MOFs), a class of tunable materials comprised of organic linkers and inorganic nodes,[131-137] have been demonstrated by us, among others, as porous supports to enhance the stability and, in some cases, catalytic activity of the encapsulated enzymes.[24, 49, 54, 59, 138] In particular, zirconium-based MOFs (NU-10xx series) demonstrate excellent stability in a wide range of acidic and basic pH.[105, 139] The hierarchical pore structure[140-143] allows for the inclusion of large catalytic guest molecules,[144-146] while allowing substrate diffusion through an auxiliary channel and access to the catalyst through apertures connecting the channels (**Figure 4-1** a).

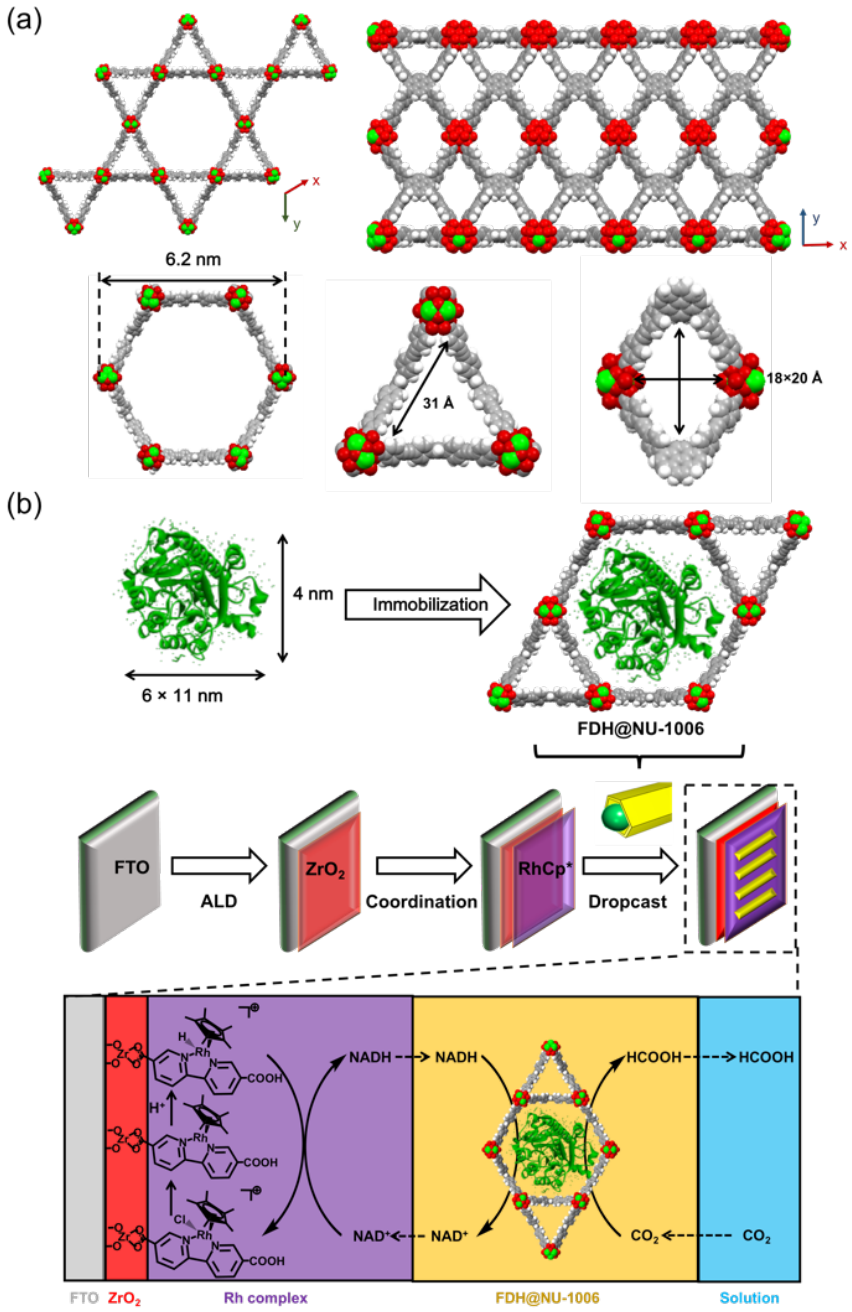

Figure 4-1 (a) Crystal structure of MOF NU-1006. (b) Schematic illustration of FTO electrode modification method and the bioelectrocatalytic reaction mechanism for CO_2 reduction.

Formate dehydrogenase (FDH) from the yeast species Candida boidinii has been widely studied not only for its ability to sequester CO_2[121, 147-148] but also to transform this carbon source into biomass for the production of biofuels.[149-151] Despite the high efficiency and selectivity, FDH reaction rate depends heavily on the environment, and FDH activity decreases significantly

when the pH is lower than 6.[152-153] Hence, the stabilization of FDH in acidic environment becomes vital to maintaining activity in concentrated CO_2 solution. To protect FDH, the enzyme was herein immobilized in NU-1006 (**Figure 4-1** b). The deposition of an electron mediator and the enzyme@MOF composite on a conductive glass electrode afforded a system which, under an applied potential, could perform the electrocatalytic generation of formic acid from CO_2 in high yield. NU-1006 was selected as the supporting material because FDH (6 nm × 4 nm × 11 nm) matched the size of the mesoporous channels (6.2 nm). The diameters are similar to promote van der Waals interactions between the FDH and the interior of the MOF in order to prevent leaching.

4.2 Experimental Methods

4.2.1 Material Syntheses

General. MOF NU-1006 was synthesized and activated following the published method.[154] Cp*Rh(2,2'-bipyridyl-5,5'-dicarboxylic acid)Cl_2 was synthesized with the reported condition.[155] All other chemicals were used as received from Fisher Scientific or Sigma Aldrich.

4.2.2 Physical Methods

Inductively coupled plasma-optical emission spectroscopy (ICP-OES) was performed three times to measure the ratio of Zr to S in FDH@NU-1006 sample. The experiment was performed on QTEGRA software v. 2.2 Thermo iCap 7600 Duo ICP-OES (Thermo Fisher Scientific, Waltham, MA, USA) operating in standard mode. HNO_3 (1.5 mL) was added to 2-3 mg FDH@NU-1006 sample in a 5 mL microwave vial for digestion followed by 0.5 mL H_2O_2. After sealing, the vial was heating in a Biotage (Uppsala, Sweden) SPX microwave reactor (software version 2.3, build 6250) at 150 °C for 15 min. The solution was then diluted by Millipore water, and the ratio of S to Zr content was quantified by calibration curve of standard

solutions. N_2 sorption isotherm measurements were performed on a Micromeritics ASAP 2020 (Micromeritics, Norcross, GA) at 77 K. Samples of 20 to 30 mg were required for each measurement. Powder X-ray diffraction (PXRD) measurements were performed on a STOE-STADI MP powder diffractometer equipped with a Cu rotating anode X-ray source. Scanning electron microscopy (SEM) images and energy dispersive X-ray spectroscopy (EDX) were collected on Hitachi SU8030. Samples were coated with 7 nm OsO_4 in a Denton Desk III TSC Sputter Coater (Moorestown, NJ) before each analysis. Gas chromatography measurement was performed by Agilent GCMS-Headspace. The sample was derivatized before each measurement (details below).

4.2.3 Electrochemical Measurements.

All electrochemical measurements were conducted with a CHI-900 electrochemical workstation. A conventional three-electrode setup was used, with a platinum wire and a Ag/AgCl/NaCl (3 M) as the counter electrode and reference electrode, respectively. The Rh complex-modified FTO electrode deposited with or without FDH@NU-1006 was served as the working electrode. Bare FTO electrode was used as the working electrode to obtain the cyclic voltammogram (CV) of NAD^+ in CO_2 saturated solution. 0.5 M Tris buffer was used as the electrolyte.

4.2.4 FDH Encapsulation.

FDH encapsulation with NU-1006. Activated NU-1006 crystals (5 mg) were treated with 1 mL FDH solution (in Tris buffer, 4.5 g/L) for 3 h at room temperature to make sure the FDH remains excess. FDH loading was then measured by ICP-OES. To remove the unencapsulated FDH, the solid sample was then washed with DI water for three times after removing the supernatant.

FDH@NU-1006 loading (in mole percent) calculation. The FDH loading in mole percent was calculated with the equation below. There are 28 S in one molecule of FDH and 6 Zr one node of NU-1006. The solvent area volume of NU-1006 is 76.28 nm^3.

$$FDH\ loading = \frac{mole\ of\ FDH}{mole\ of\ Zr\ node} \times 100\%$$

4.2.5 Rh-FTO Electrode Modification.

Before atomic layer deposition (ALD), FTO glass was cut into 2 cm × 3 cm pieces and then sonicated in soap water, ethanol and then acetone for 15 min consecutively. After the washing steps, FTO glass was dried under nitrogen flow to avoid contamination from the air. ALD was performed by Savannah 100 system. Tetrakis (dimethylamido)zirconium (IV)(TDMAZ) was used as the zirconium precursor and DI water served as oxygen source. The ALD chamber was held at 150 °C under N_2 flow for deposition. To grow zirconium oxide on FTO, Zr precursor (150 °C) was pulsed for 0.03 s, followed by 20 s N_2 purge (A half-cycle); then, water was pulsed for 0.02 s and followed by another 20 s N_2 purge (B half-cycle). The AB cycle was performed for 3 times. Then, the FTO glass after ALD was wrapped with Electron Microscopy Sciences KAPTON tape and an area of 1.1 cm × 1.4 cm was exposed for further modification. To synthesize Rh(III)-FTO electrode, 2 mg of Rh(III) complex was mixed with methanol and drop-casted on the exposed area of FTO electrode. After drying in the air, the Rh(III) on FTO electrode was further fixed with 200 μL of Nafion solution (10% Nafion in methanol). Then, 5 mg of FDH@NU-1006 was mixed with 200 μL of Nafion solution and drop-casted on the Rh(III)-FTO electrode. The resulting electrode was air-dried to prepare the FDH@NU-1006 modified Rh(III)-FTO electrode for the enzymatic reaction.

4.2.6 Derivatization before GCMS-Headspace Measurement.

To measure the formic acid concentration in the reaction solution, 100 μL of reaction solution was mixed with 100 μL methanol and followed by 5 μL of concentrated H_2SO_4 in a 10 mL glass headspace vial (Agilent Technologies, USA). Then the mixture solution in the vial was mixed by slight agitation before being placed on the auto sampler.

4.3 Results and Discussion

The MOF was synthesized and activated following the reported procedure.[154] Activated NU-1006 was soaked in FDH solution (6×10^{-3} mM in 0.5 M Tris buffer, pH=7.5) for 4 h at room temperature for the encapsulation of FDH. Then, the solid material was centrifuged down to remove the excess FDH and washed 3 times with deionized (DI) water to obtain FDH@NU-1006. The loading of FDH was determined by inductively coupled plasma-optical emission spectroscopy (ICP-OES) to be 0.04 ± 0.001 FDH/node (based on S to Zr ratio). This would equate to FDH taking up 39.4% of the hexagonal pore volume.

The N_2 sorption isotherms measured at 77 K of the support NU-1006 and the composite FDH@NU-1006 display a much lower N_2 uptake capacity after the encapsulation of FDH (**Figure 4-2** a), and the Brunauer-Emmet-Teller (BET) area dropped from 1730 to 710 m^2/g due to the incorporation of FDH in the parent framework. The density functional theory (DFT) calculated pore size distribution shows the disappearance of the mesopores, while the micropores are maintained (**Figure 4-3**), implying the FDH is located within the mesopores. Powder X-ray diffraction (PXRD) patterns verify that NU-1006 retains its crystallinity after encapsulation of FDH (**Figure 4-2** b), confirming that the decreased N_2 uptake is not a result of MOF degradation. The lower intensity of the (100) Bragg peak has been attributed previously to occupation of the mesopore with a guest molecule.[156] Furthermore, the SEM images confirm the retained morphology of NU-1006 after FDH encapsulation (**Figure 4-2** c and **Figure 4-2** d), and the

energy dispersive X-ray spectroscopy (EDX) line scan indicates that FDH is uniformly distributed in NU-1006 crystals (**Figure 4-4**).

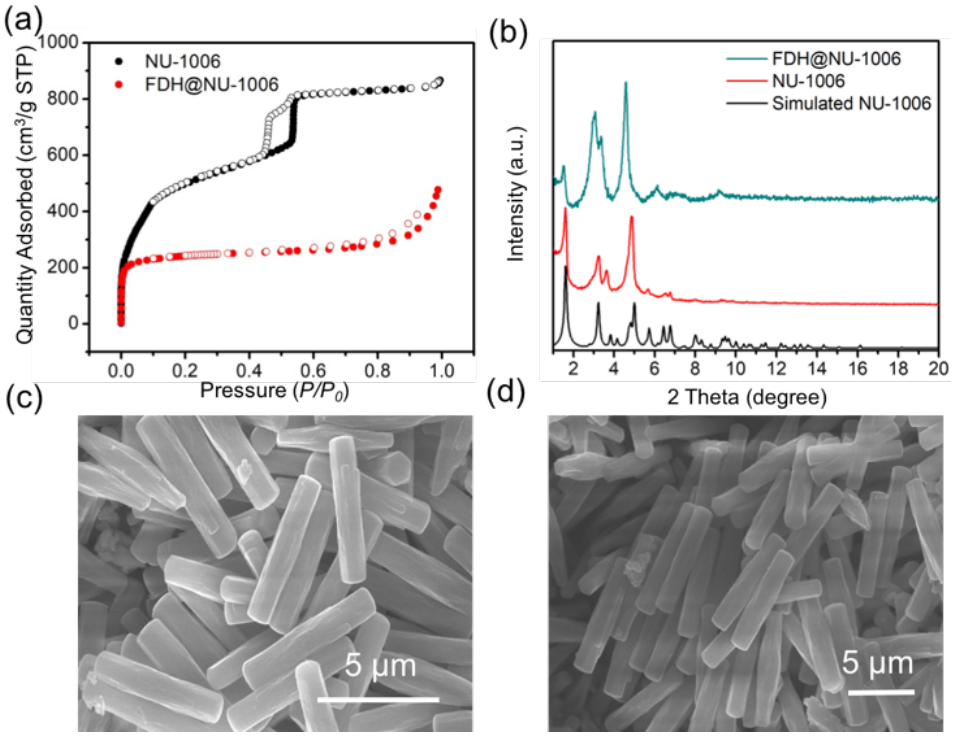

Figure 4-2 (a) N_2 sorption isotherms of NU-1006 (black) and FDH@NU-1006 (red) (b) PXRD patterns of synthesized NU-1006, simulated NU-1006, and FDH@NU-1006 (c) SEM image of NU-1006 (d) SEM image of FDH@NU-1006.

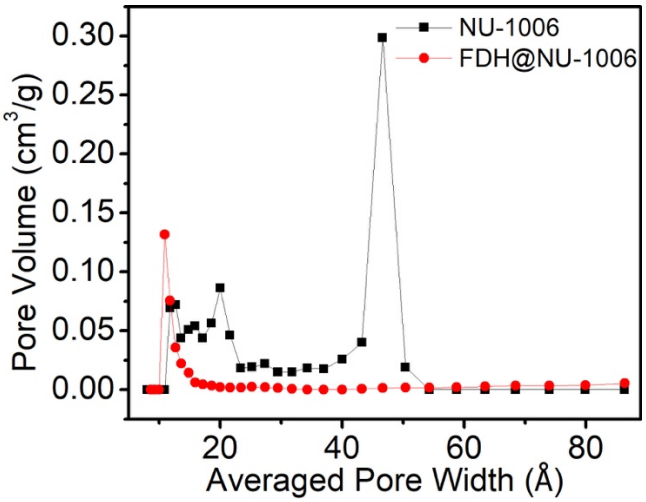

Figure 4-3 DFT Pore size distribution of NU-1006 and FDH@NU-1006.

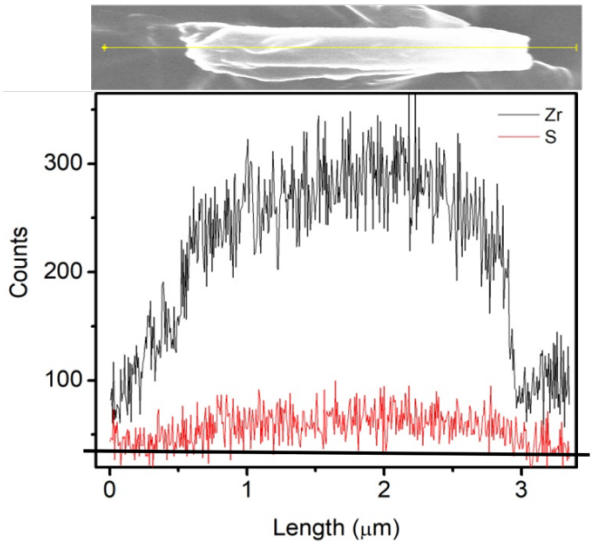

Figure 4-4 SEM-EDX line scan measured on a crystal of FDH@NU-1006.

Given the near uniformity of the MOF pore size and the kinetic diameter of FDH, we speculated that the MOF pores can effectively mitigate, or all together eliminate, the FDH deactivation by preventing enzyme exfoliation through confinement. To test this, catalytic amounts of the free FDH and FDH@NU-1006 (6×10^{-3} mM of FDH) were suspended in Tris buffer solutions at different pH. The optimal pH for FDH reaction is reported as pH = 7, and FDH activity decreases with the drop of environmental pH.[152] Once suspended, nicotinamide adenine dinucleotide (NADH, 13 Å × 11 Å × 19 Å, 1 mM) was added, and the conversion of NADH to NAD^+ was monitored by ultraviolet–visible spectroscopy (UV-vis; **Figure 4-5**). For free FDH reaction, the amount of converted NADH is significantly lower at pH = 4 Tris buffer solution (the same pH of saturated CO_2 solution) compared to that of pH = 7 (**Figure 4-6** a). In comparison, the activity of encapsulated FDH remains unchanged in acidic environment, which suggests that NU-1006 protects FDH in acidic environment. In addition, at the optimal reaction pH (pH=7), FDH@NU-1006 is approximately three-fold more efficient at converting NADH than the free FDH within the same amount of time and same amount of enzyme. To rationalize this behavior,

bare NU-1006 was added to solutions of NADH and NAD^+, and the NADH/NAD^+ concentrations were measured by UV-vis spectroscopy. With selective adsorption of NADH against NAD^+ (**Figure 4-7**), NU-1006 can realize the pre-concentration of the reaction substrate, thus leading to the observed increase of the reaction rate.

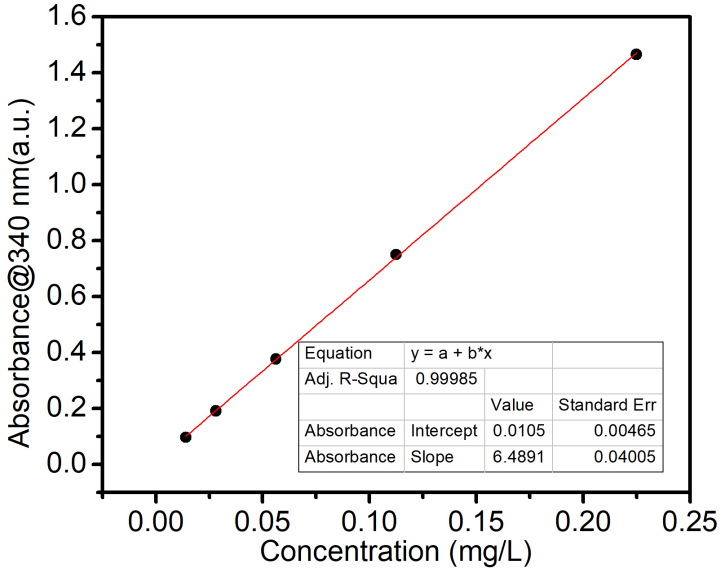

Figure 4-5 UV-vis standard curve for NADH.

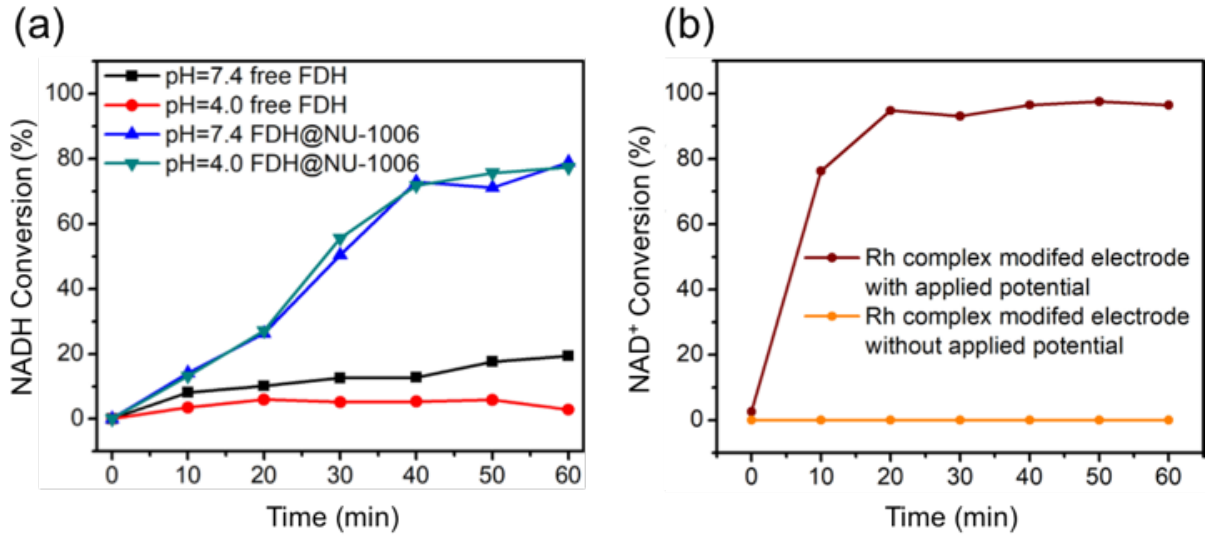

Figure 4-6 (a) Conversion of NADH by free FDH and suspended FDH@NU-1006 at pH = 7.4 and pH = 4.0 within 1 h. (b) NAD^+ conversion to NADH using Rh-FTO glass electrode with and without an applied potential.

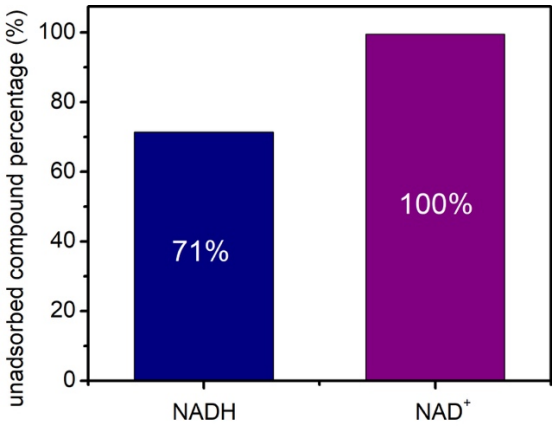

Figure 4-7 The percentage of NADH and NAD+ left in the supernatant after adding 5 mg of NU-1006 to the 10 mL solution. The starting concentrations of NADH and NAD^+ were 1 mM.

To avoid using NADH as a stoichiometric reagent, NAD^+ can react with a hydride donor to yield NADH, a process which can be catalyzed electrochemically. The electrochemical NADH regeneration was accomplished by using a modified electrode. Briefly, the surface of a conductive fluorine-doped tin oxide (FTO) glass slide was coated with ZrO_2 via atomic layer deposition (ALD). The zirconia layer allowed for coordination to the carboxylic acid moieties on the Rh complex (Cp*Rh(2,2'-bipyridyl-5,5'-dicarboxylic acid)Cl_2), a reported hydride transfer agent which will prevent the formation of undesired byproduct NAD_2 dimer (**Figure 4-1**).[119] To decide the potential applied to the electrode, the cyclic voltammograms (CV) of the Rh complex-modified FTO electrode and NAD^+ were measured and a potential of -1.1 V vs. Ag/AgCl was chosen to be applied to realize the regeneration process (**Figure 4-8** and

). The electrode coated with the Rh complex (1×10^{-2} mM) was immersed in a 1 mM solution of NAD^+, and the NADH concentration was quantified by UV-vis by monitoring the absorbance of the supernatant at 340 nm. After applying a −1.1 V vs. Ag/AgCl potential for 1 h, the reaction reached equilibrium in 20 min with more than 90% of the NAD+ converted to NADH (**Figure 4-6** b). The color of the Rh-FTO glass electrode turned from yellow to brown when the potential was

applied during the reaction, which corresponds to the reduction of Rh(III) to Rh(I) (**Figure 4-10**),[157-158] and the color of the electrode reverts back to yellow when the potential was removed. Without an applied potential, NADH is not observed in the presence of the Rh(III) complex on FTO glass electrode.

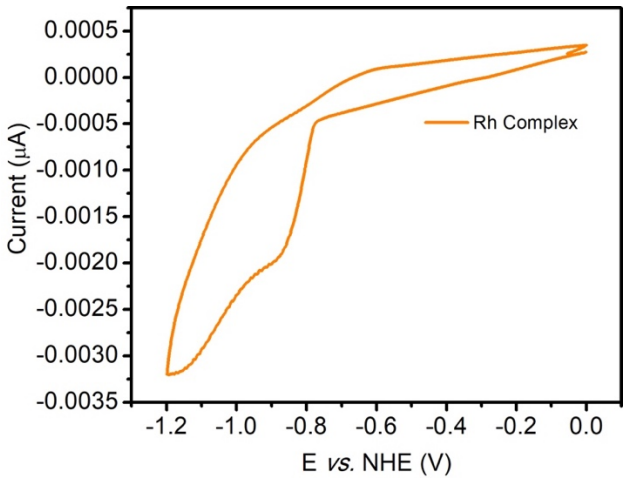

Figure 4-8 CV of Rh complex-modified FTO electrode measured in CO_2 saturated 0.5 M Tris buffer. Scan rate: 50 mV/s.

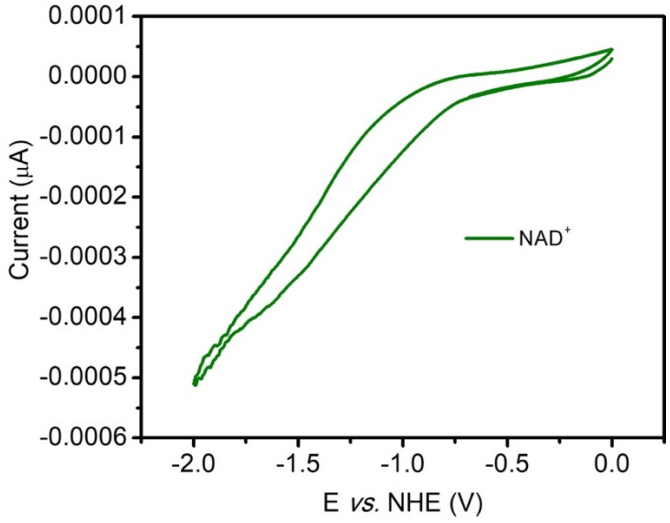

Figure 4-9 CV of NAD^+ (1 mM) with bare FTO electrode measured in CO_2 saturated 0.5 M Tris buffer. Scan rate: 50 mV/s.

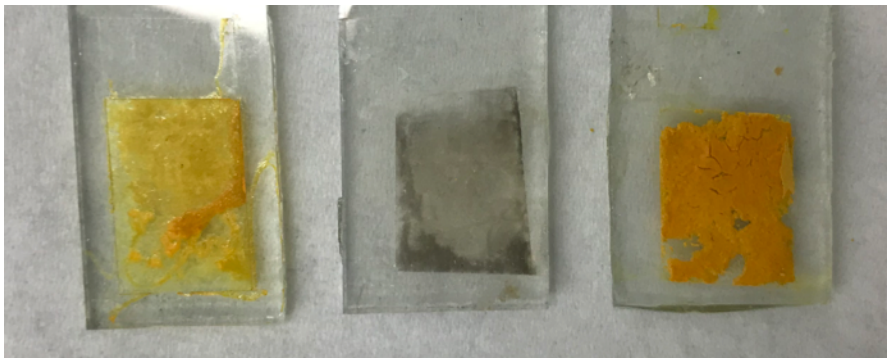

Figure 4-10 Photos of Rh(III)-FTO electrode before (left) and immediately after (middle) NADH regeneration reaction and FDH@NU-1006 modified Rh(III)-FTO electrode (right).

After determining that the enzyme@MOF could oxidize NADH and the Rh complex could reduce NAD^+, we sought to verify that the regenerated NADH can be utilized by FDH for CO2 fixation reaction to further realize the bioelectrocatalytic reaction system, using NAD^+ as the coenzyme. Formic acid in excess of 1 turnover would be produced by FDH@NU-1006 if the enzyme is able to use the NADH regenerated by the Rh-FTO electrode. For this system, FDH@NU-1006 (6×10^{-3} mM of FDH) crystallites were drop-casted from a Nafion solution onto an Rh-FTO electrode to limit the effect of diffusion on the accessibility of the regenerated NADH to the encapsulated enzyme. The modified electrode was then immersed in 10 mL of a CO2 saturated 0.5 M Tris buffered solution, and 1 mM of NAD^+ was added. The concentration of formic acid in solution was measured by headspace gas chromatography (GC-Headspace) after derivatization with methanol (**Figure 4-11**). After 1 h at -1.1 V applied potential, the concentration of formic acid reaches 79 ± 3 mM (**Figure 4-12**), which corresponds to a turnover number of 1.3×10^4 and also suggests that each NADH was regenerated an average of 79 times during the reaction, comparing with the starting NAD+ concentration at 1 mM. During the reaction, the concentration of NADH increases gradually and eventually reached saturation after 60 min (**Figure 4-13**). The Rh-FTO electrode modified by drop-casting of free FDH with Nafion

solution shows a lower reaction rate by producing around 25 mM of formic acid in 1 h under the same condition (**Figure 4-14**). Without applying a potential, NADH is unable to be regenerated, and consequently, there is no obvious change in formic acid concentration in solution which confirms that only NADH, instead of NAD^+, can be utilized in the production of formic acid. The Rh-FTO electrode with NU-1006 crystallites (no FDH) drop casted on does not increase the formic acid concentration with increasing exposure time, indicating that formic acid in solution is not introduced by the MOF crystals. Additionally, Rh-FTO electrode without enzyme@MOF does not produce formic acid without FDH in 1 h.

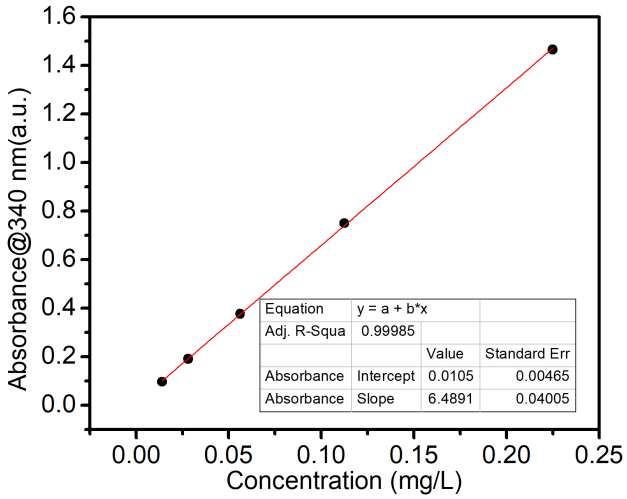

Figure 4-11 UV-vis standard curve for NADH.

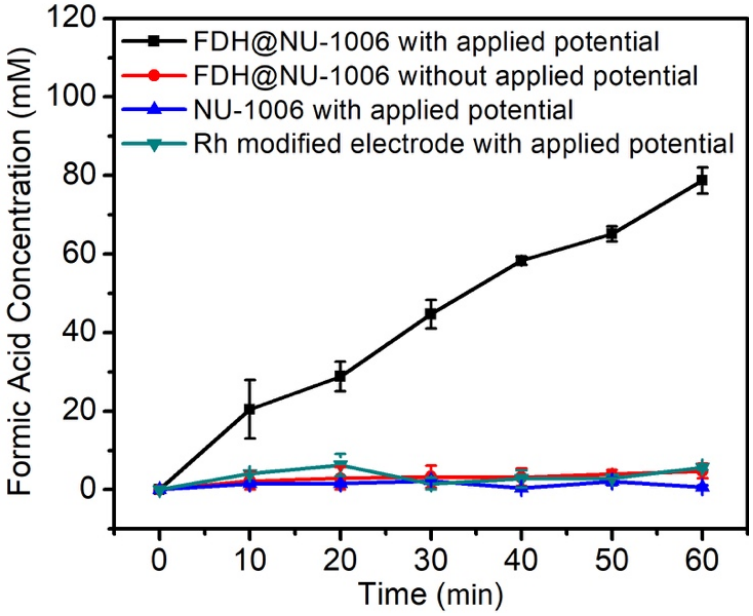

Figure 4-12 The concentration of formic acid generated by FDH with NAD^+ in Tris buffer solution with saturated CO_2.

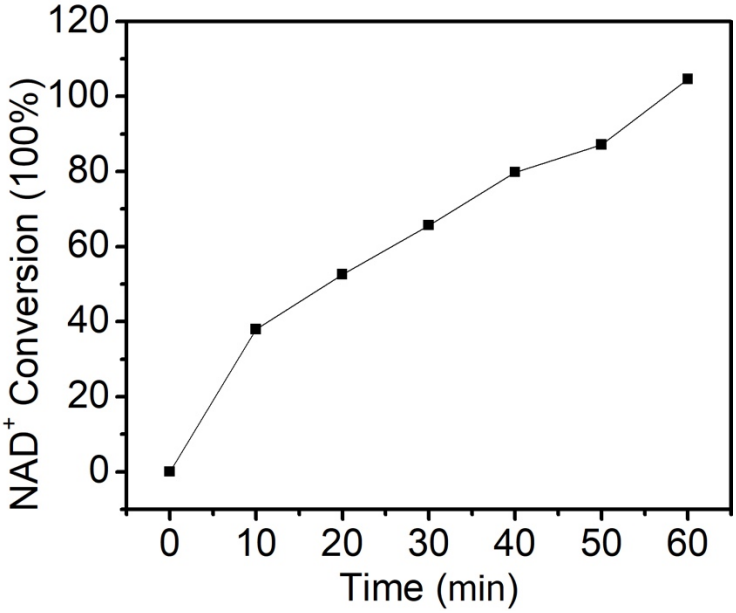

Figure 4-13 NAD^+ conversion during bioelectrocatalytic reduction of CO_2.

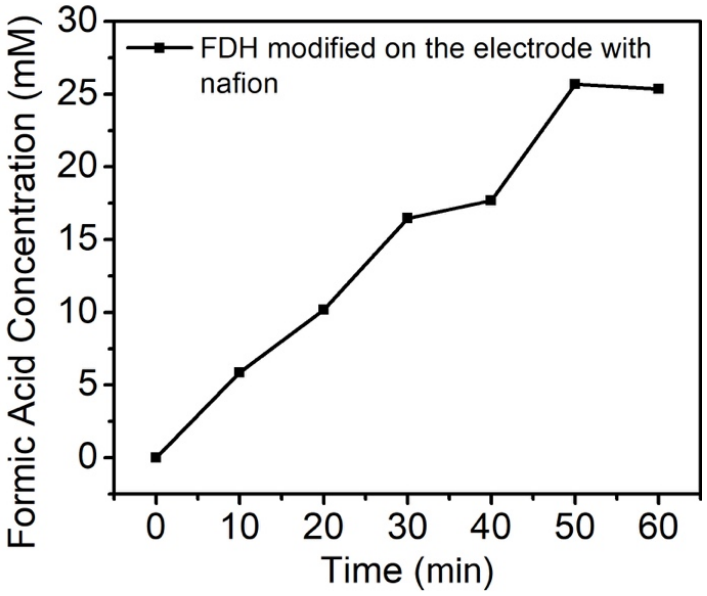

Figure 4-14 The concentration of formic acid generated by FDH with NAD^+ in Tris buffer solution with saturated CO_2.

4.4 Conclusions

In conclusion, we successfully stabilized FDH for CO_2 fixation within the mesoporous MOF, NU-1006, in an acidic environment. The encapsulated FDH exhibited enhanced activity for the generation of NAD^+ from NADH, even at the enzyme's optimal reaction pH. Importantly, the NADH can be regenerated using Rh-FTO glass electrode. Coupling these reactions, formic acid was produced using catalytic amount of NAD^+ and enzyme over an applied potential, which can realize the simple separation of enzyme from the reaction system as well as the high efficiency CO_2 fixation with recyclable co-factor. These results have paved the way for the design of highly efficient and sustainable electro-enzymatic reaction systems for carbon fixation.

Chapter 5 . Integration of Enzymes and Photosensitizers in a Hierarchical Mesoporous Metal–Organic Framework for Light-Driven CO_2 Reduction

Portions of this chapter appear in the following manuscript:

Chen, Y., Li, P., Zhou, J., Buru, C. T., Đorđević, L., Li, P., Zhang, X., Cetin, M.M., Stoddart, J.F., Stupp, S.I., Wasielewski, M.R., Farha, O. K. Integration of Enzymes and Photosensitizers in A Hierarchical Mesoporous Metal–Organic Framework for Light-driven CO_2 Reduction. *JACS.* **2020**, *142(4)*, 1768-1773.

5.1 Introduction

The increasing demands for clean, renewable and sustainable fuels have stimulated the fast evolution of technologies to harvest natural resources like solar energy.[159] Though synthetic multi-junction solar cells achieve nearly 48% quantum efficiencies for electricity generation,[160] systems that convert solar irradiation directly to high-value chemicals remain elusive.[161] As a consequence of the multi-step processes involved in solar-to-chemical conversion, biological-based approaches, such as those employing photosynthesis, would be ideal candidates for this complicated process; these systems, however, suffer from low efficiencies as a result of poor light harvesting.[162-164] Thus, the development of semi-artificial systems interfacing the highly efficient synthetic light harvesters with sophisticated biological processes capable of biomass production is a highly desirable combination, which can efficiently take advantage of the abundant solar radiation with minimal waste generation.[165]

In formate dehydrogenase (FDH)-based photosystems, the enzyme requires a coenzyme, nicotinamide adenine dinucleotide (NAD^+/NADH) to produce formic acid from CO_2. As a consequence of the energy mismatch between an excited state photosensitizer and NAD^+, an electron mediator which does match the excited state photosensitizer is often employed.[166-167] to regenerate the coenzyme so that the reaction is not stoichiometric in NADH A rhodium-based complex, Cp*Rh(bpy)Cl (RhCp*, Cp* = pentamethylcyclodienyl; bpy = bipyridine)[168] and its derivatives, have proven[122, 169] to be efficient electron mediators for this process. The fabrication of a semi-artificial photosynthetic (SAP) system, which can access efficiently all the components involved, requires precise atomic arrangements,[170] close proximity,[171] and high chemical stability[105, 172]. Previously reported inorganic-organic-biological hybrid systems for solar-to-chemical conversions include (i) coupling FDH CO_2 reduction with a graphene-based

photocatalyst,[121] (ii) a water-soluble zinc porphyrin,[173] (iii)a Mg chlorophyll-a photosensitizer[174] and (iv) a viologen skeleton.[175] While these SAP systems are able to generate value-added products utilizing light-harvesting molecules, redox enzymes, and coenzymes, they tend to suffer from low reaction rates and system stability.

Metal-organic frameworks (MOFs) are highly crystalline, porous materials with diverse customizable components that make it possible to access a wide variety of structures and functionalities to target applications, including, but not limited to, gas storage[176-177] and separation,[178-179] catalysis,[140, 146, 180] and light harvesting.[162, 181] Incorporation of photosensitizing molecules as the struts in MOFs can assemble the chromophores into well-isolated and structurally ordered arrays for efficient light harvesting.[162, 182-184] The separation of these chromophores allows for effective energy transfer and antenna behavior, while preventing[185] excited state quenching through self-association. The water-stable zirconium-based MOF, NU-1000, bearing pyrene-based linkers has already been demonstrated[186] by us as an effective photosensitizer capable of producing singlet oxygen under LED irradiation. As an addition to NU-1000, our group has recently reported[154] the de novo synthesis of the isoreticular series NU-100x (x = 2 to 7), all composed of tetracarboxylate-based linkers with a pyrene core. The large mesopores (3.1 to 6.5 nm) of these MOFs have been utilized to anchor a wide variety of large redox active compounds such as molecular switches,[187] C60[188-189] and even a range of enzymes.[58, 190]

In this chapter, we selected the hierarchical mesoporous MOF, NU-1006, for the incorporation of electron mediators and FDH to assemble (**Figure 5-1** a) a prototypical SAP system. Upon excitation of the scaffold MOF, a series of electron transfers allows for the generation of NADH from NAD^+. Most importantly of all, when the FDH enzyme is

encapsulated in the MOF scaffold, the system, driven by white light, utilizes (**Figure 5-1** b) the photochemically generated NADH to convert CO_2 to formic acid.

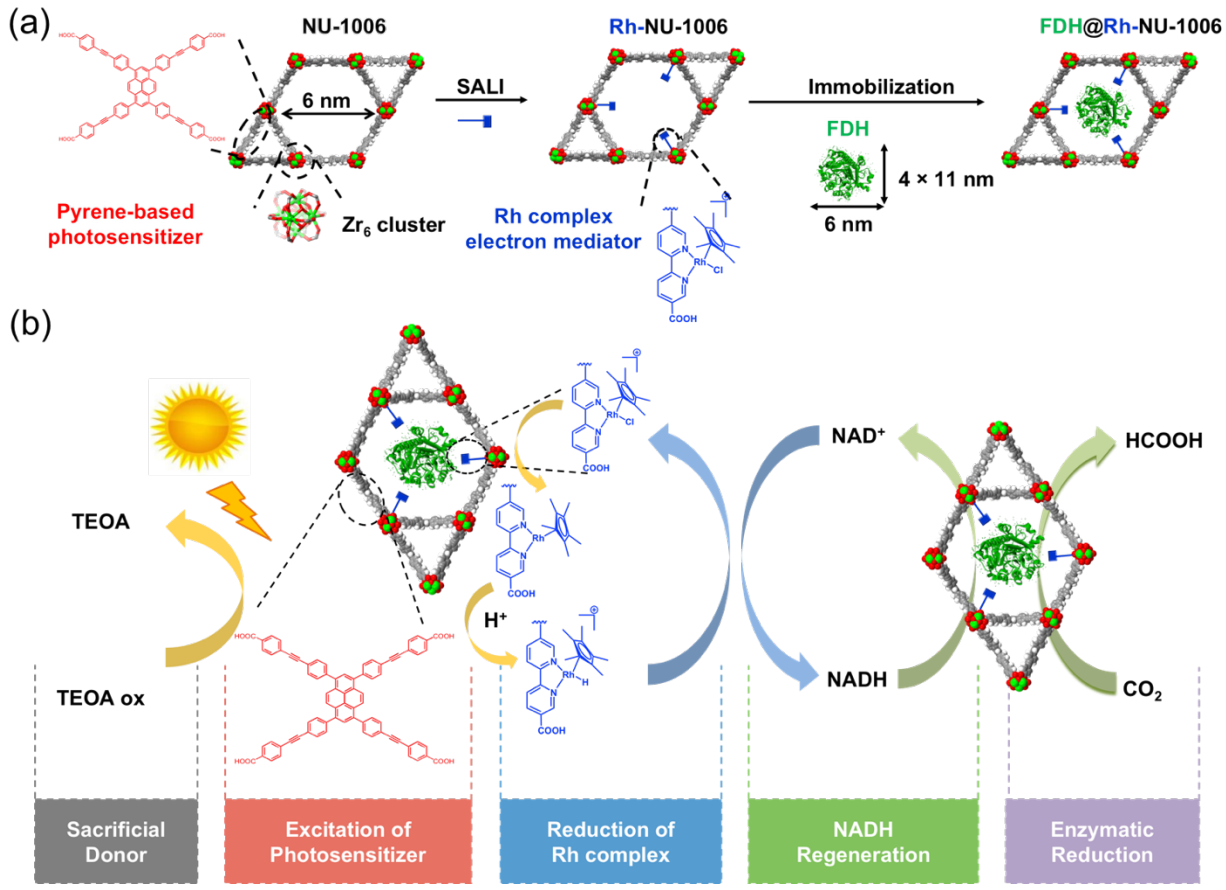

Figure 5-1 (a) Schematic representation of the de novo assembly of pyrene-based photosensitizers and Zr6 clusters in NU-1006 (left), Solvent-Assisted Ligand Incorporation (SALI) of electron mediators on the node (middle) to obtain Rh-NU-1006, and encapsulation of the FDH enzyme to form FDH@Rh-NU-1006; (b) illustration of the primary catalytic cycle, where photochemical NADH regeneration with modified MOF is coupled with enzymatic CO2 reduction (red spheres = O, green spheres = Zr, gray spheres = C, white spheres = H).

5.2 Experimental Methods

5.2.1 Material Syntheses

Tris-HCl solution (pH=7) was prepared by adding HCl to the purchased Tris buffer solution until the pH value dropped to 7. MOF NU-1006 was synthesized and activated following the published method.[154] Cp*Rh(2,2'-bipyridyl-5,5'-dicarboxylic acid)Cl_2 (RhCp*) was synthesized

with the reported condition.[155] All other chemicals were used as received from Fisher Scientific or Sigma Aldrich.

5.2.2 Physical Methods

Powder X-ray diffraction was measured at room temperature on a STOE-STADI P powder diffractometer equipped with an asymmetric curved Germanium monochromator (CuKα1 radiation, λ = 1.54056 Å) and a one-dimensional silicon strip detector (MYTHEN2 1K from DECTRIS). The line focused Cu X-ray tube was operated at 40 kV and 40 mA. Ar sorption isotherm measurements were performed on a Micromeritics ASAP-2020 (Micromeritics, Norcross, GA) at 87 K. The data points between 0.03 and 0.14 P/P_0 were chosen for the BET surface area calculation to minimize the error for consistency criteria (R^2=0.9997). Between 30 and 50 mg of material was used for each measurement. The pore size distribution analysis was obtained by fitting the 2D-NLDFT model to the argon adsorption isotherms measured at 87 K. Inductively coupled plasma-optical emission spectroscopy (ICP-OES) was performed three times to measure the quantify the loading of Rh complex in NU-1006. The experiment was performed on QTEGRA software v. 2.2 Thermo iCap 7600 Duo ICP-OES (Thermo Fisher Scientific, Waltham, MA, USA) operating in standard mode. HNO_3 (1.5 mL) was added to 2-3 mg Rh-NU-1006 in a 5 mL microwave vial for digestion followed by 0.5 mL H_2O_2. After sealing, the vial was heating in a Biotage (Uppsala, Sweden) SPX microwave reactor (software version 2.3, build 6250) at 150 °C for 15 min. The solution was then diluted by Millipore water, and the ratio of Zr to Rh was determined by calibration curve of standard solutions. Diffuse reflectance UV-vis spectra of the solid MOF samples were recorded with a Shimadzu UV-3600 with a Harrick Praying Mantis diffuse reflectance accessory. Teflon was used as a perfect reflector for baseline collection and the samples were diluted with Teflon for the measurements. The obtained reflectance spectra were

converted to absorption spectra by using Kubelka–Munk function. $\alpha/S = (1 - R)^2(2R)^{-1}$ where R is the reflectance, α and S are the absorption and scattering coefficients, respectively. Scanning electron microscopy (SEM) images and energy dispersive X-ray spectroscopy (EDX) were collected on Hitachi SU8030. Samples were coated with 7 nm OsO_4 in a Denton Desk III TSC Sputter Coater (Moorestown, NJ) before each analysis. Gas chromatography measurement was performed by Agilent GCMS-Headspace. The sample was derivatized before each measurement (details below). Steady-state and time-resolved photoluminescence (TRPL) spectra were acquired using HORIBA Fluorolog-3 equipped with a 450 W xenon lamp and a TCSPC module (diode laser excitation at $\lambda = 375$ nm).

5.2.3 Electrochemical Measurements

All electrochemical measurements were conducted with a CHI-900 electrochemical workstation. A conventional three-electrode setup was used, with a platinum wire and a Ag/AgCl/NaCl (3 M) as the counter electrode and reference electrode, respectively. Bare FTO electrode was used as the working electrode to obtain the cyclic voltammogram (CV) of RhCp in 0.5 M Tris buffer containing 0.1 M TEOA. For photocurrent-time (I-T) measurements, FTO glass electrode deposited with NU-1006 or Rh-NU-1006 was used as the working electrode, the scan rate was set as 50 mV s^{-1}.

5.2.4 Rh Complex Incorporation

In order to execute the SALI process, NU-1006 (0.46 mM in MeOH) was mixed with the Rh-complex at 1:1 gravimetric ratio to ensure excess of the Rh-complex. The mixture was stored in an oven at 60 °C for 24 h before the Rh-NU-1006 was centrifuged down and washed three times with MeOH.

5.2.5 FDH Encapsulation

5.6 mg of activated Rh-NU-1006 crystals (same molecular ratio of MOF to FDH as the previously published procedure[3]) were treated with 1 mL FDH solution (in Tris buffer, 4.5 g/L) for 3 h at room temperature to make sure the FDH remains excess. To remove the unencapsulated FDH, the solid sample was then washed with DI water for three times after removing the supernatant.

5.2.6 Deposition of MOFs on FTO

FTO glass was cut into 3 cm × 3 cm pieces and sonicated in soap water, ethanol and acetone for 15 min consecutively to remove dust and other possible contamination. After the washing steps, FTO glass was dried under nitrogen flow to prevent the dust from air. Then, the FTO glass was wrapped with Electron Microscopy Sciences KAPTON tape and left an area of 0.5 cm × 0.5 cm was exposed. 5 mg of NU-1006 or NU-1006-RhCp was mixed with 200 μL of Nafion solution (10% Nafion in ethanol) and drop-casted on the exposed area of FTO electrode. The resulting electrode was air-dried and used as working electrode for electrochemical measurements.

5.2.7 Irradiation Setup

We used 2DR borosilicate glass vials (17 × 60 mm, 03-338C, Fisher scientific) equipped with screw caps (open top, TS-13216, Thermo scientific) and Teflon disc (TS-12713, Thermo scientific). After closing, vials were flushed with stream of Ar (5 min) followed by CO_2 (10 min), using steel needles as inlet and outlet, inserted through the cap. The inlet (long needle) was placed inside the solution, while the outlet (short needle) was placed above the solution. Irradiation of the vials was done with a halogen lamp (150 W EKE bulb, 400-700 nm) mounted on a Schott DCR III light source and equipped with fiber optic goosenecks (Schott Quad calibrated bundle). The samples were suspended and irradiated from the bottom, approximately 0.5 cm from the fiber optic light source (power output ~250 $W \cdot cm^{-2}$). Furthermore, the samples rack and the goosenecks were

placed on top of an orbital shaker, which ensured mixing during the irradiation of the samples. Considering that the reduction of CO_2 to HCOOH is a two-electron process, the overall quantum yield of the process (Φ_{HCOOH}) was calculated using the following equation:

$$\Phi_{HCOOH} = \frac{\text{number of HCOOH molecules} \times 2}{\text{number of photons absorbed}} \times 100$$

The number of HCOOH molecules can be determined from the moles of HCOOMe in the solution (obtained by derivatization and GC-MS measurements as described above) and Avogadro's number (6.022×10^{23}). The number of photons (7.95×10^{17} s^{-1}) was estimated by measuring the incident light power that is reaching the vial (447 nm LED at 200 $mW \cdot cm^{-2}$, measured using an optical power meter PM100D with optical sensor S120VC from Thorlabs) and considering the illuminated area of the bottom of the vial. The obtained quantum yield is $\Phi_{HCOOH} = 6.3 \times 10^{-2}$ % (at 4 hours of irradiation).

5.2.8 Derivatization before GCMS-Headspace Measurement

To measure the formic acid concentration in the reaction solution, 100 μL of reaction solution was mixed with 100 μL methanol and followed by 5 μL of concentrated H_2SO_4 in a 10 mL glass headspace vial (Agilent Technologies, USA). Then the mixture solution in the vial was mixed by slight agitation before being placed on the auto sampler.

5.2.9 NADH Regeneration Experiments Sample Preparation

In 4 vials of 2 ml Tris buffered solution (1 mM of NAD^+, 0.5 mM of TEOA), 0.89 mM of Rh-NU-1006, NU-1006, NU-1006 mixed with Rh complex and NU-1006 linker were added respectively to ensure the equivalent amount of light-harvesting source (linker). In Tris buffer (2 mL) containing NAD^+ (1 mM) and TEOA (0.5 mM) were measured to get the background absorbance at 340 nm at 0 min. When Rh complex was added to system, its final concentration

was controlled to be 0.029 mM (same as that in Rh-NU-1006).

5.2.10 Formic Acid Generation Sample Preparation

A white light (150 W EKE bulb, 400-700 nm), equipped with fiber optic goosenecks, was chosen as a mimic for sunlight to irradiate the samples and generate electrons for photochemical regeneration of NADH. In order to maintain the suspension of the samples during irradiation, vials containing different samples were placed on a shaker and irradiated from the bottom, approximately 0.5 cm from the fiber optic light source. FDH@Rh-NU-1006 (1.8×10^{-3} M) was dispersed in Tris buffer solution (2 mL) containing 0.5 mM TEOA and 1 mM NAD^+ in a 2-dram vial. In the experiment, 5 vials were sealed and purged with Ar for 3 times to exclude the effect of air in the reaction. After that, 4 of the vials were further purged with CO_2 the time points and 1 vial were used as a control experiment to test if the FDH@Rh-NU-1006 itself can generate formate without CO_2.

5.2.11 Chromatographic Detection of Gases

The samples were prepared in the same way as described above, but with the pressure of CO_2 being 1 atm inside the vial. The gases generated during the photolysis were quantified by GC (Shimadzu GC-2014) thermal conductivity detector (TCD) and flame ionization detector (FID) measurements of 500 μL injections from the reaction vial headspaces. The experiments were performed at least in duplicate (errors <10%). It was found that the FDH@Rh-NU-1006 (1.8×10^{-3} M, dispersed in 2 mL Tris buffer solution, containing 0.5 mM TEOA and 1 mM NAD^+) generates small amounts of CO gas. No H_2 or CH_4 were detected. After four hours of irradiation with white light (250 W/cm^2) the total amount of CO produced was 48.4 nmol. For comparison, the amount of HCOOH produced in the same amount of time is 3.17±0.001 μmol.

5.2.12 ^{13}C NMR of Reaction Solution

The samples were prepared in the same way and were irradiated with white light (250 W/cm^2). After 4 hours, 500 μL of the reaction solution were transferred to an NMR tube, 3-(trimethylsilyl)propionic-2,2,3,3-d_4 acid sodium salt (TSP) standard was added (10 μL of 0.23 M solution in D_2O), followed by 50 μL of D_2O. The quantitative ^{13}C NMR spectrum (Figure S13) was obtained with Bruker Avance III 500 MHz system (equipped with DCH CryoProbe). The TSP signals are at 54.90, 19.66, 15.56 and −2.04 ppm (*Organometallics* **2010**, *29*, 2176–2179, 10.1021/om100106e). The NMR spectrum shows a small peak at 49.5 ppm, which indicates the presence of a small amount of CH_3OH in the solution.

5.3 Results and Discussion

In order to assemble the semi-artificial system, the Rh-complex, Cp*Rh(bpydc)Cl (bpydc = bipyridine-2,10-dicarboxylic acid), is first of all incorporated into NU-1006 by solvent-assisted-ligand-incorporation (SALI), which replaces a pair of terminal OH/OH_2 ligands on the 8-connected node with a carboxylate group appended to the molecule of interest which has proven[191] effective for the incorporation of carboxylate-functionalized organic ligands on the Zr-nodes of MOFs. After incorporating Rh complex, Rh loading was measured by inductively coupled plasma-optical emission spectroscopy (ICP-OES) to be 1.2±0.1 Rh/node, based on Rh-to-Zr ratio. The ^1H nuclear magnetic resonance (^1H NMR) spectrum (**Figure 5-2**) of Rh-NU-1006 was collected after MOF digestion. Comparing the ^1H NMR spectrum of NU-1006 with that of the Rh complex alone, the spectrum of the post-SALI MOF confirmed that Rh complex had been incorporated into the MOF. FDH was then immobilized in Rh-NU-1006, following a previously reported[190] method.

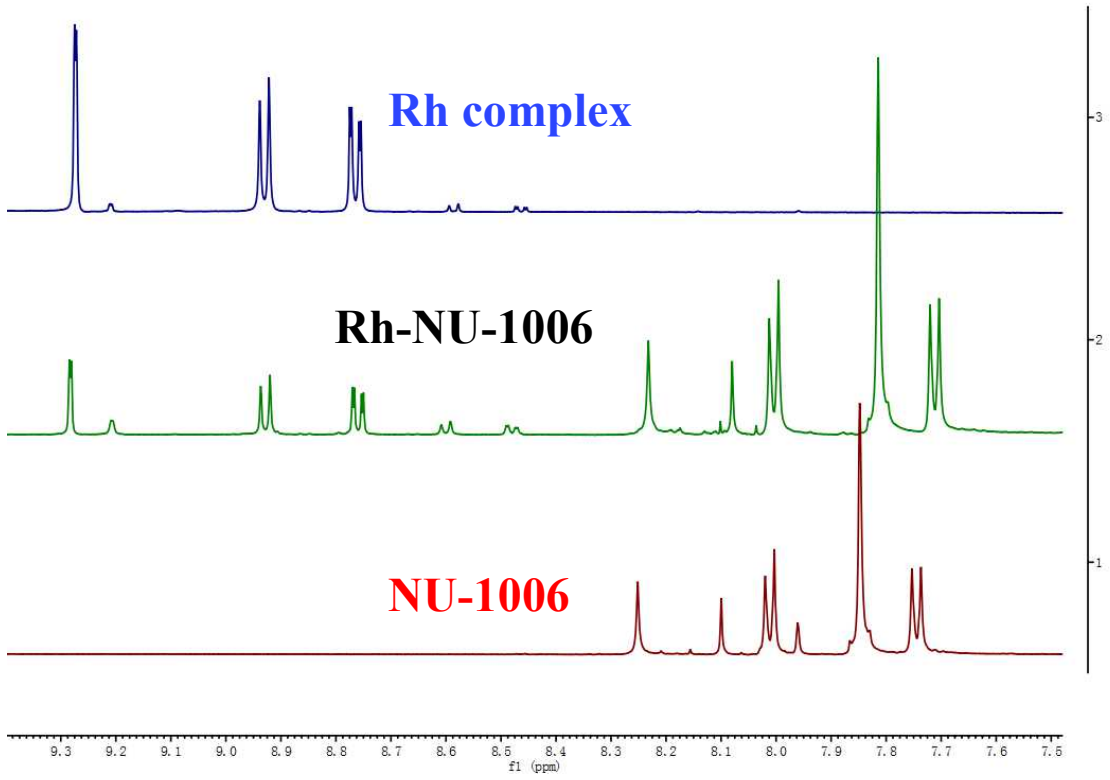

Figure 5-2 ^{1}H NMR spectrum of Rh Complex, digested NU-1006, and digested Rh-NU-1006.

Powder X-ray diffraction (PXRD) patterns indicate (**Figure 5-3** a) that the bulk crystallinity of NU-1006 is retained after SALI of Rh-complex, as well as after the immobilization of FDH. Ar sorption isotherms at 87 K show two-steps for NU-1006, confirming (**Figure 5-3** b) the existence of the two mesoporous channels in its structure.[154] The decrease in Ar uptakes for Rh-NU-1006 and FDH@Rh-NU-1006 indicates the incorporation of the Rh complex in NU-1006 and the existence of the enzyme in the sample, respectively. Compared to that of the parent NU-1006, the pore size distribution (**Figure 5-4**) of Rh-NU-1006 suggests a decreased in volume for both the hexagonal mesopore (pore width= 6.2 nm) and the triangular channels (pore width= 3.1 nm), indicating that the Rh-complex is located inside both pores. For FDH@Rh-NU-1006, the hexagonal mesopores of NU-1006 are occupied by the enzymes, while the triangular channel and the orthogonal windows between the channels (2.0 nm) remain accessible to the co-enzymes. The

retention of the rod-shaped morphology in Rh-NU-1006 is confirmed (**Figure 5-5**) with scanning electronic microscopy (SEM) images. No obvious degradation of the MOF crystals is observed after SALI. Energy dispersive X-ray spectroscopy (EDX) line scans of Rh-NU-1006 show (**Figure 5-6**) that the Rh complex is well-distributed in NU-1006 crystallites.[102, 141]

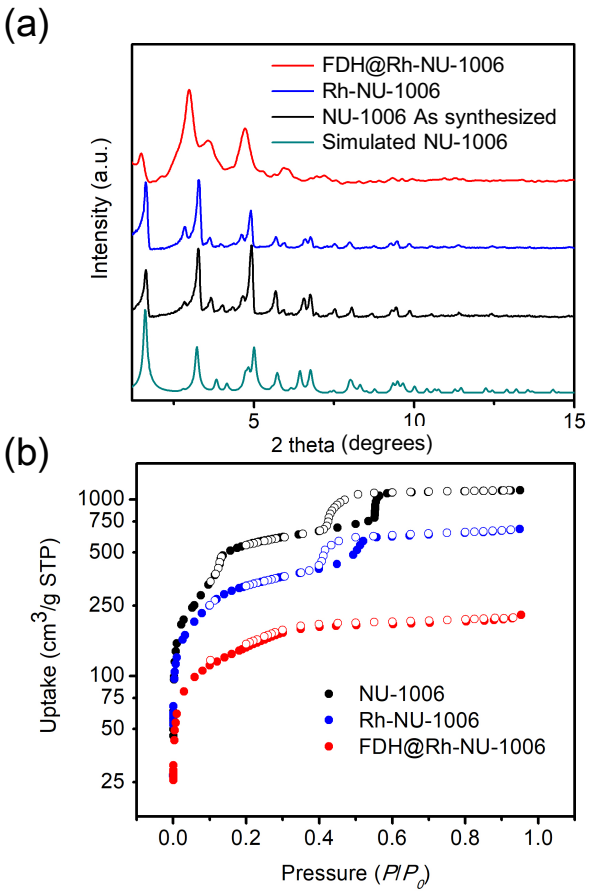

Figure 5-3 (a) PXRD patterns of FDH@Rh-NU-1006, Rh-NU-1006, as synthesized NU-1006 and simulated NU-1006 (b) Ar isotherms of NU-1006, Rh-NU-1006, and FDH@NU-1006.

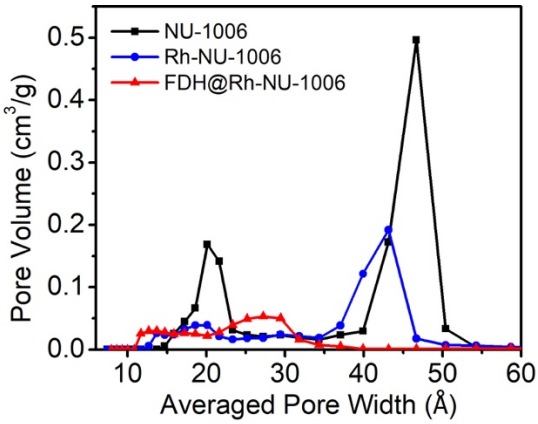

Figure 5-4 Pore size distribution of NU-1006, Rh-NU-1006 and FDH@Rh-NU-1006.

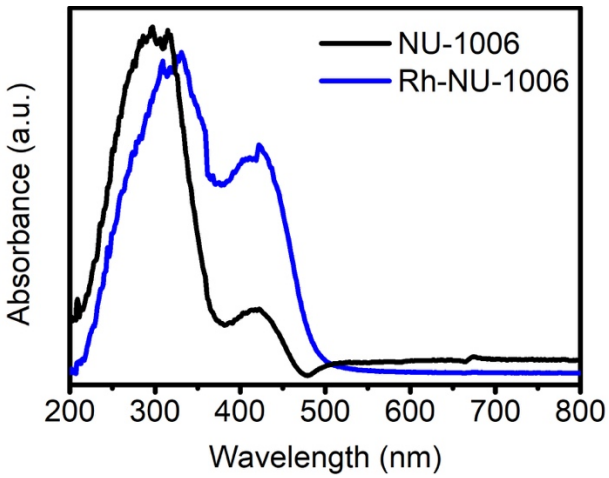

Figure 5-5 Diffuse reflectance UV-vis absorption measurement of Rh-NU-1006.

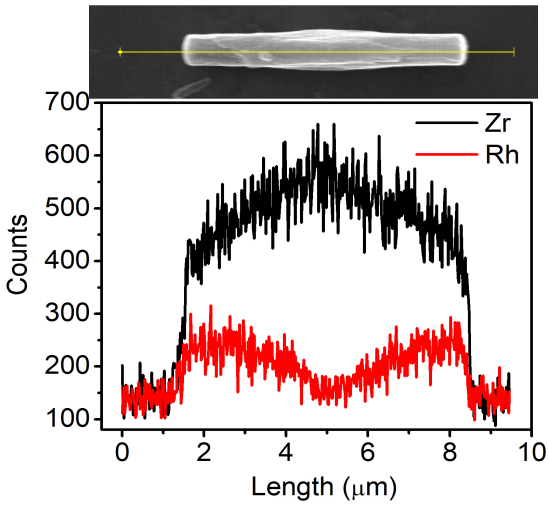

Figure 5-6 Energy dispersive X-ray spectroscopy (EDX) line scans of Rh-NU-1006.

Diffuse reflectance UV-Vis measurements of Rh-NU-1006 shows (**Figure 5-7**) two strong absorption peaks at 300 and 420 nm, respectively, which are consistent with that of NU-1006. In order to probe the electron transfer process between the photo-excited pyrene-based linkers and the incorporated Rh-complex, the transient photocurrent was measured under high density blue LED light illumination - λ_{max} = 420 nm, 36 W, Kessil H150 Blue grow light. In this experiment, NU-1006 and Rh-NU-1006 were each mixed in Nafion solutions (90 g/L in EtOH), and the mixtures were drop-casted on fluorine-doped tin oxide (FTO) glass (0.5 cm × 0.5 cm) (**Figure 5-8**). The photo-response of Rh-NU-1006 decreased in intensity significantly compared with that (**Figure 5-9** a) of NU-1006, suggesting that some of the electrons are transferred within the sample instead of being measured by the working electrode. In order to confirm the electron transfer within Rh-NU-1006, a static fluorescence measurement (**Figure 5-10**) and time-resolved fluorescence decay analysis (**Figure 5-9** b) were carried out. The results of time-resolved emission kinetics display that the emission lifetime of Rh-NU-1006 is the shortest - within the 0.1 ns time resolution for the streak camera at this time range - as compared to that of (i) the NU-1006 (0.5 ± 0.1 ns), (ii) the physically mixed pyrene linker and Rh complex (1.4 ± 0.1 ns), (iii) the physical mixture of NU-1006 and the Rh complex (0.6 ± 0.1 ns), and (iv) the free pyrene-based linker (1.4 ± 0.1 ns). The results confirm that electron transfer is facilitated when the linker and Rh complex are assembled within the MOF.

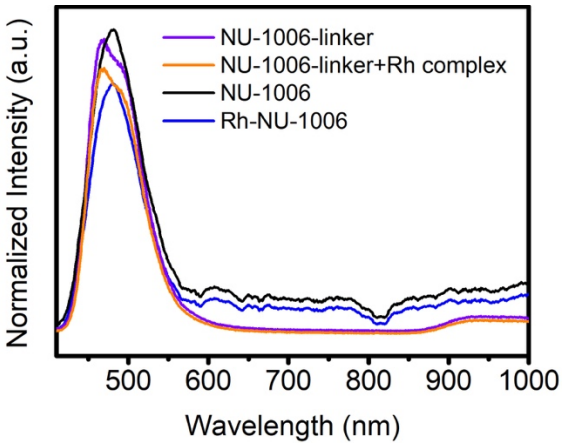

Figure 5-7 Static fluorescence spectrum of NU-1006 linker, NU-1006 with Rh complex, NU-1006 and Rh-NU-1006.

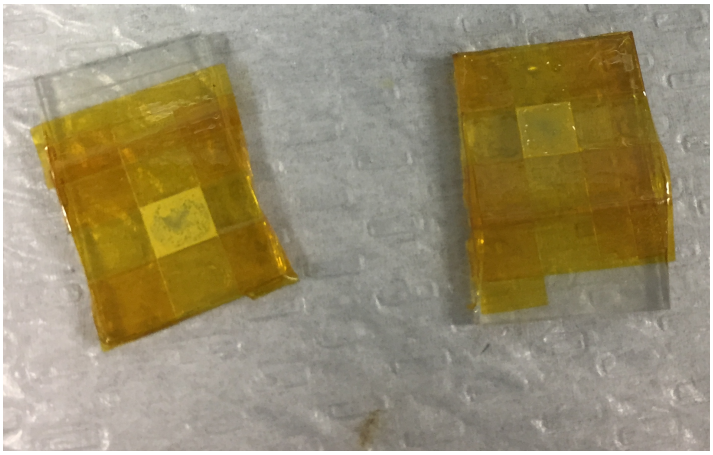

Figure 5-8 Photos of FTO electrodes deposited with NU-1006 (left) and Rh-NU-1006 (right).

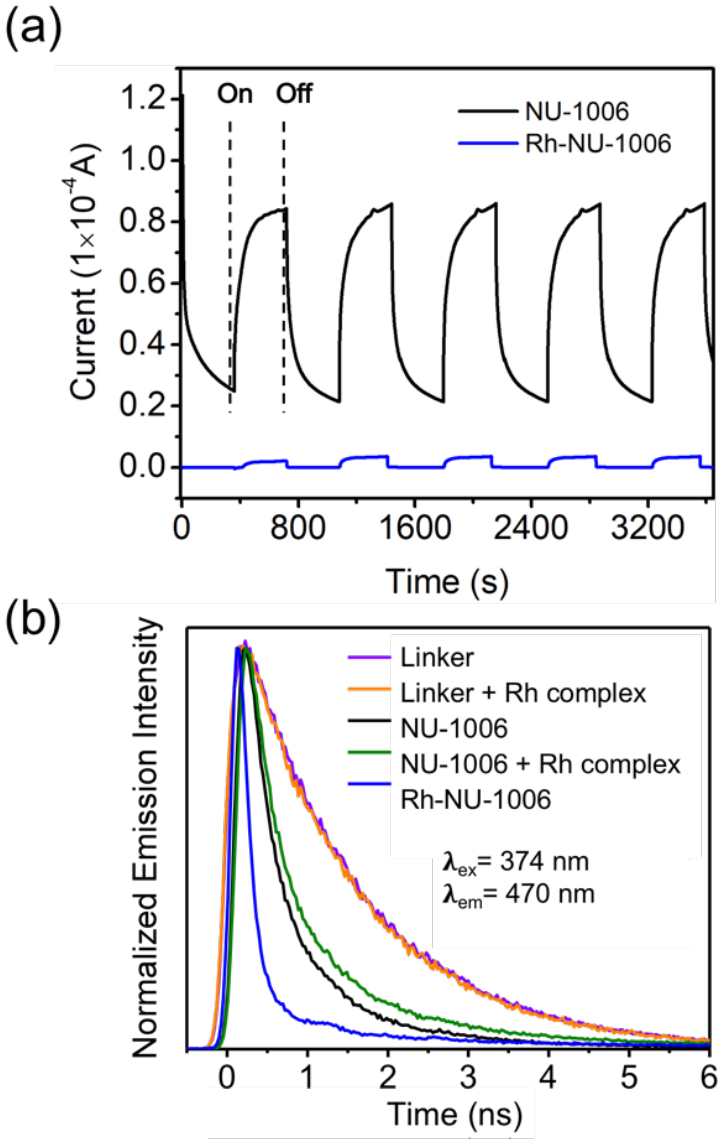

Figure 5-9 (a) Photocurrent-time profiles of NU-1006 and Rh-NU-1006 under illumination of blue LED light at the potential of -0.2 V vs. Ag/AgCl. (b) Time-resolved fluorescence intensity of NU-1006-linker, NU-1006 linker mixed with Rh complex, NU-1006, and Rh-NU-1006.

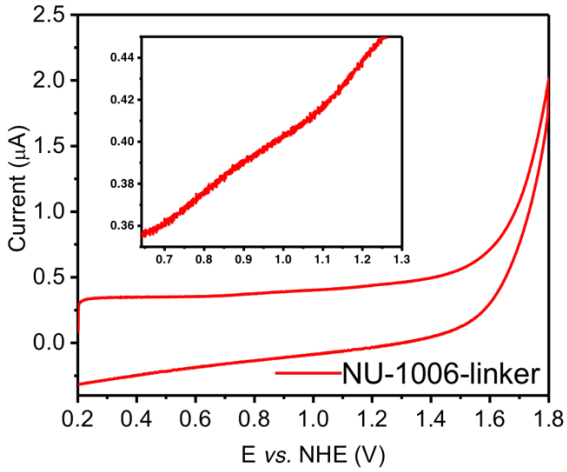

Figure 5-10 CV of NU-1006 linker in Tris buffer. Scan rate: 50 mV/s.

In an attempt to illustrate the photochemical NADH regeneration process, the energy diagram is shown (**Figure 5-11**) for the reactions. The linker and Rh complex reduction potentials were observed (**Figure 5-12** and **Figure 5-13**) at −1.09and −0.86 V vs. Ag^{+}/AgCl, respectively, by cyclic voltammetry (CV). The highest occupied molecular orbital (HOMO) (E≈ −7.09 eV) and lowest unoccupied molecular orbital (LUMO) (E≈ −3.31 eV) of the pyrene-based linker were calculated from CV.[192] Visible-light driven electron transfer from the pyrene linkers to the electrochemical mediator results in the activation of the Rh complex. Thereafter, the activated electron mediator can deliver[190, 193] one further hydride to NAD^{+}. Meanwhile, the sacrificial electron donor, triethanolamine (TEOA), reduces the oxidized pyrene core of the linker to avoid photodegradation.

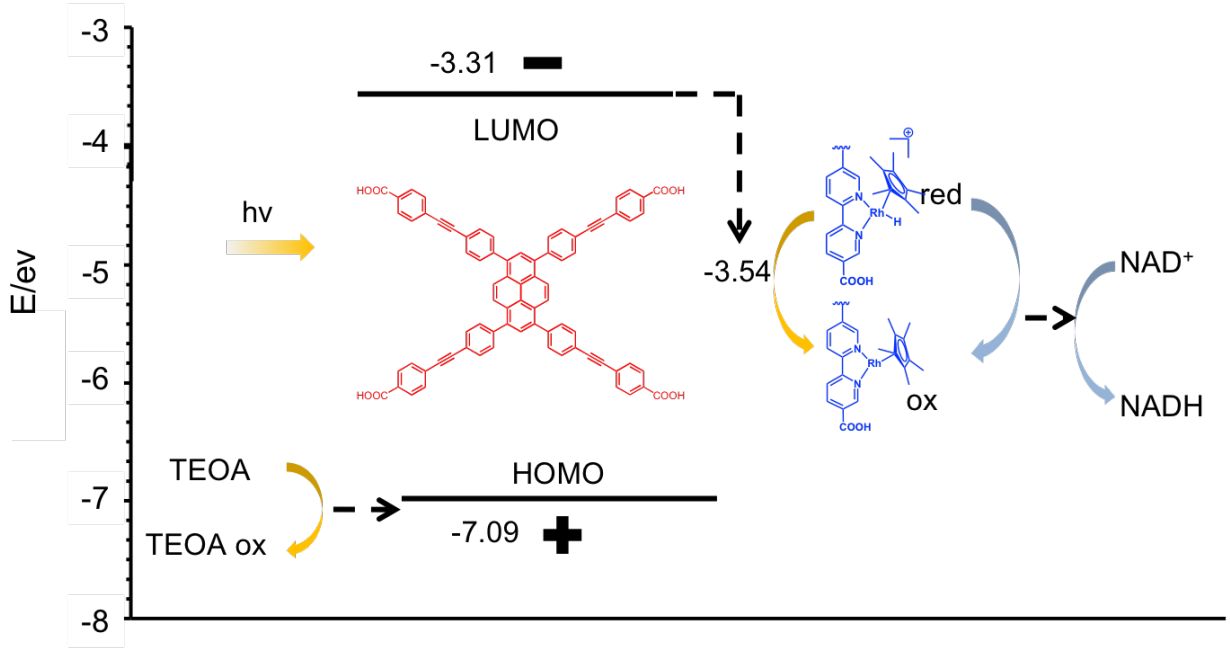

Figure 5-11 Energy diagram of photochemical regeneration of NADH in NU-1006.

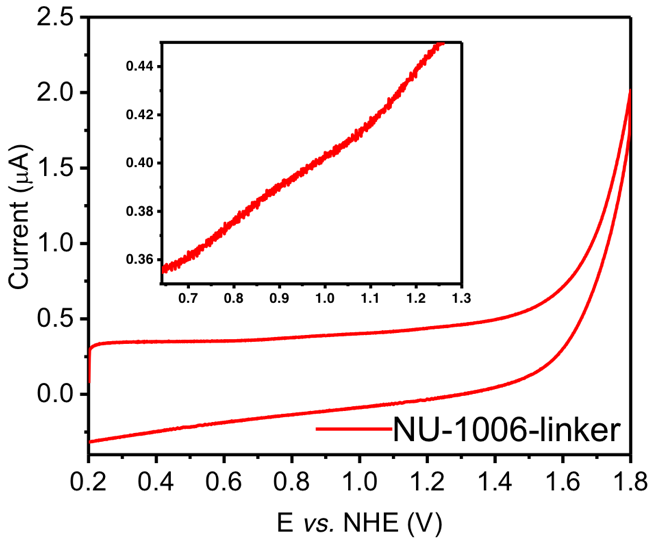

Figure 5-12 CV of NU-1006 linker in Tris buffer. Scan rate: 50 mV/s.

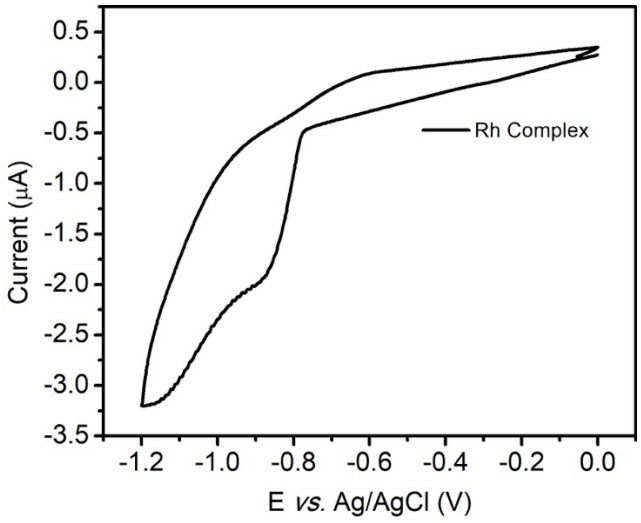

Figure 5-13 CV of Rh complex measured in Tris buffer. Scan rate: 50 mV/s.

In order to verify that Rh-NU-1006 is able to generate the coenzyme NADH with NAD^+ as depicted (**Figure 5-14**) in the energy diagram, the concentration of generated NADH in the solution was measured by UV-Vis spectra. A white light was chosen as a mimic for sunlight to irradiate the samples. The physical mixture of the Rh complex and NU-1006 is able to convert 10% of NAD^+ to NADH in 2 h, when compared with the starting NAD^+ concentration (1mM). Similarly, the Rh complex mixed with the linker is able to convert 8% of starting NAD^+, suggesting the combination of electron mediator and photosensitizer are able to realize the conversion of NAD^+. Without the Rh complex being an electron mediator, NU-1006 by itself is not able to convert a significant amount of NAD^+. With the close proximity of Rh complex to the pyrene-based linkers, Rh-NU-1006 is able to converts 28% of the starting NAD^+ after 2 h, which is about three times as much as the physical mixture of MOF and the electron mediator (**Figure 5-14** a). After 24 h, quantitative of the initial NAD^+ was converted to NADH.

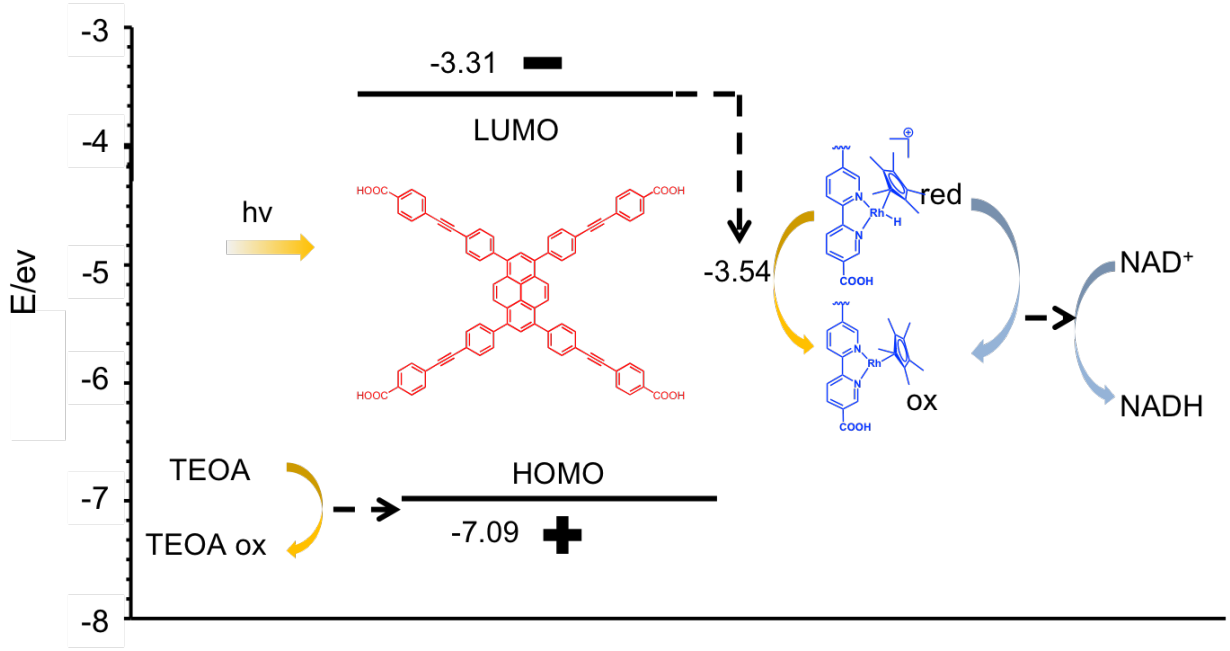

Figure 5-14 Energy diagram of photochemical regeneration of NADH in NU-1006.

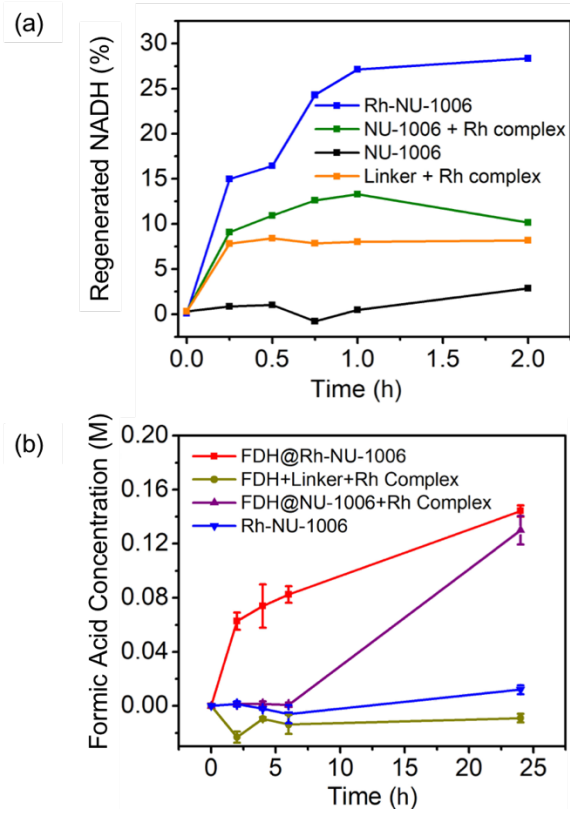

Figure 5-15 Energy diagram of photochemical regeneration of NADH in NU-1006.

After verifying that Rh-NU-1006 is able to regenerate NADH from NAD^+ with white light irradiation, FDH was then immobilized with Rh-NU-1006 through post-synthetic encapsulation. The loading of FDH was determined to be 0.042 ± 0.001 FDH/node by ICP-OES. The concentration of formate was measured by headspace gas chromatography (GC-Headspace) after derivatization with MeOH. Under the irradiation with white light, FDH@Rh-NU-1006 was able to generate (**Figure 5-14** b) 0.144 ± 0.003 M formate from CO_2 after 24 h, resulting in a turnover frequency of 865 h^{-1} in 24 hours, a performance which is far superior compared (**Table 5-1**) with these previously reported FDH immobilized system.[121, 173-175, 189] In order to test the benefit of MOF-encapsulation of FDH in the reaction, a homogeneous mixture of NU-1006 linker, FDH and Rh complex was measured. After 24 h of irradiation with the same light source, no obvious increase of formate concentration was detected, confirming that the close proximity of electron mediator and the photosensitizer is crucial for this solar-to-chemical conversion system. The Rh-NU-1006 alone is not able to generate a significant amount of formic acid (0.013 ± 0.01 M), confirming that FDH is the main contributor to CO_2 reduction. The physical mixture of FDH@NU-1006 with Rh complex does not generate any formic acid in the first 6 hours; however, after 24 h, 0.144 ± 0.003 M of formic acid was generated. We believe that the incorporation of Rh complex within/on the surface of MOF crystals via SALI allows for the reaction to proceed.

Table 5-1 Turnover frequencies of FDH immobilized with different materials with photochemical substrate regeneration.

Support Material Type	Turnover Frequency
Graphene-based Photocatalyst (CCGCMAQSP)[121]	1.69 h^{-1} (in 2 h)
Zinc tetrakis(4-methylpyridyl) porphyrin (ZnTMPyP)[173]	0.10 h^{-1} (in 3 h)

Photosensitisation of Mg chlorophyll-a (Mg Chl-a)[174]	4.64 h^{-1} (in 1 h)
Viologen Skeleton[175]	9.38 h^{-1} (in 10 min)
Rh-NU-1000 (this work)	**865 h^{-1} (in 24 h)**

5.4 Conclusions

In conclusion, a modified mesoporous MOF, based on NU-1006, with pre-installed Rh-based electron mediators, was employed for the encapsulation of FDH in order to realize a highly efficient CO_2 fixation system. The utilization of solar energy in coenzyme regeneration was achieved by anchoring an electron mediator, Rh complex, into the hierarchical mesoporous MOF which contains pyrene-based linkers. Upon immobilization in Rh-NU-1006, FDH is able to convert CO_2 to formate using NAD^+ under white light within the same MOF crystal. By coupling the photochemical coenzyme regeneration with enzymatic CO_2 reduction, we are able to minimize the diffusion of regenerated substrate to enzyme as well as cofactor-regeneration with an environmental-friendly source of energy. These results open the way for the design of SAP systems for high efficiency CO_2 reduction with recyclable coenzyme.

Chapter 6 . Insights into the Enhanced Catalytic Activity of Cytochrome c When Encapsulated in a Metal–Organic Framework

Portions of this chapter appear in the following manuscript:

Chen, Y., Jiménez-Ángeles, F., Qiao, B., Krzyaniak, M.D., Sha, F., Kato, S., Gong, X., Buru, C.T., Chen, Z., Zhang, X., Gianneschi, N.C., Wasielewski, M.R., Olvera de la Cruz, M. & Farha, O. K.. Insights into the Enhanced Catalytic Activity of Cytochrome c When Encapsulated in a Metal–Organic Framework. *JACS.* **2020**, *142(43)*, 18576-18582.

6.1 Introduction

Enzymes are biocatalysts with intricate three-dimensional structures that nature has perfected over millions of years. With the increasing demand in green chemistry, enzymes have received widespread attention because of their high reaction selectivity, as well as, activity under mild reaction conditions.[194] However, incompatible conditions such as high temperature, unfavorable pH, and the presence of organic solvents can easily result in the destruction of enzyme structures, which often manifests as a decline in their activity. This fragile nature of enzymes consequently limits their industrial utilization. To improve their long-term stability and recyclability, various methods have been investigated, including enzyme immobilization,[126, 195] protein engineering, to name a few,[196] among these, physical entrapment has gained widespread attention with its relatively straightforward immobilization process with minimal alteration on enzyme structures, leading to improved stability and preserved, and sometimes even enhanced, enzymatic activity.[195, 197]

Various supporting materials such as silica matrix,[198-199] organic polymers,[195, 200-202] and protein-based compartments[125, 203] have been explored for enzyme encapsulation. As a class of highly porous materials, metal–organic frameworks (MOFs), composed of tunable organic linkers and inorganic nodes, have been extensively studied for various applications, including gas storage/separation,[204-206] drug delivery,[105, 207-208] catalysis,[140, 209-210] and chemical sensing.[211] Most recently, MOFs have also been investigated as promising enzyme supports. Apart from the high loading capacity MOFs can provide, the tunability of MOFs also allows enzyme/MOF systems to act as nanoreactors that can combine enzymatic reactions with other types of reactions simultaneously or in tandem.[212-213] In addition, with their atomically-precise, highly-ordered crystalline structures, MOFs can be characterized with a variety of physical methods such as X-

ray diffraction. This ease in structural characterization provides MOFs with tremendous advantages over the traditional materials in the fundamental understanding of the interactions between the encapsulated enzymes and the host matrix.

To encapsulate enzymes within MOFs, two major strategies are used: 1. *de novo* encapsulation, where MOFs are assembled around enzymes, and 2. post-synthetic encapsulation, where enzymes are introduced into pre-synthesized MOFs.[59] In many cases, especially when enzymes are encapsulated post-synthetically with MOFs that have large pores[214] or when mesoporous defects were created within enzyme@microporous MOF aggregates,[60, 215-217] immobilized enzymes exhibit higher apparent catalytic activity compared with the activity of free enzymes.[60, 212, 214-215] Three possible hypotheses have been proposed for this enhanced reaction rate. Firstly, the rigid MOF structure limits the unfolding of encapsulated enzymes and improve their stability under harsh conditions, such as organic solvents, high temperatures, as well as, unfavorable pH.[105, 124, 172, 218] Secondly, MOFs provide elevated concentration of reaction substrate inside pores around the enzymes and further facilitate the reaction.[214, 219] Lastly, it has been hypothesized that the structure of enzymes change when entering MOFs[63] and this process might be beneficial for their catalytic performance. However, the structural and conformational changes of enzymes immobilized inside the pores of MOFs remain largely elusive because of the difficulties in characterizing the structure of encapsulated enzymes.

Herein, we reported the structural characterization of encapsulated Cytochrome c (Cyt c) in a mesoporous MOF, NU-1000, through a combination of experimental and computational methods. The composite's catalytic activity was evaluated by probing the change in absorbance and heat during the oxidation of 2,2'-azino-bis(3-ethylbenzothiazoline-6-sulfonic acid) (ABTS) (**Figure 6-1**).

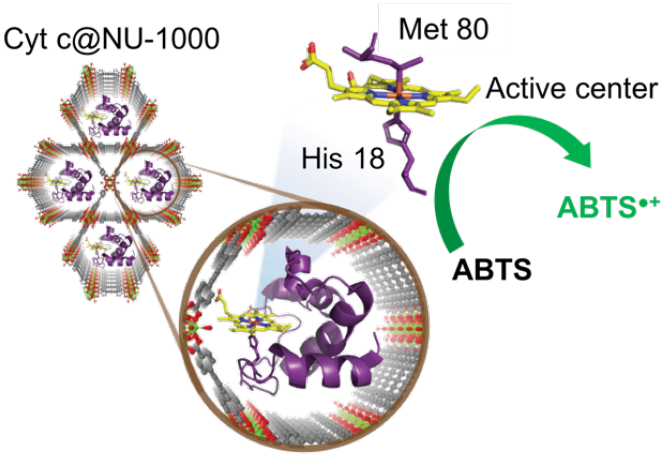

Figure 6-1 Schematic illustration of Cyt c encapsulated in the mesopores of MOF NU-1000 and its oxidation of ABTS. The atoms color code is as follows: yellow, C; orange, S; red, Fe; blue, N; purple, protein region.

Cyt c is a transmembrane protein isolated from mitochondrial membrane and possesses a heme Fe active center among several α-helices in its structure.[220] In this chapter, we selected Cyt c as a model enzyme to investigate its structural and catalytic behavior upon the encapsulation with MOF because of its small size (12 kDa, 3.2 nm × 2.7 nm × 3.8 nm), well-characterized and relatively simple structure, and extensively studied catalysis. The structurally well-defined, water-stable, channel-type MOF, NU-1000, was used as a platform for Cyt c encapsulation. NU-1000 is a zirconium-based MOF consists of 8-connected Zr_6 nodes and 4-connected tetratopic 1,3,6,8-tetrakis(p-benzoate)pyrene linkers. Its hierarchical structure which contains both mesopores (3.2 nm in diameter) and micropores (1.3 nm) enables the accommodation of the enzyme. The composite of Cyt c in NU-1000 is denoted as Cyt c@NU-1000.

6.2 Experimental Methods

6.2.1 Materials Syntheses

General MOF NU-1000 was synthesized and activated following the published method.[221] 20 mg NU-1000 crystals were soaked in 7mg/ml Cyt c solution for 5 hours to ensure its

encapsulation and Cyt c@NU-1000 crystals were then centrifuged down and washed for 3 times with deionized (DI) water to remove the excess enzymes. All other reagents were purchased from Fisher Scientific or Sigma Aldrich and used as received.

6.2.2 Physical Methods

Powder X-ray diffraction was measured at room temperature on a STOE-STADI P powder diffractometer equipped with an asymmetric curved Germanium monochromator (CuKα1 radiation, λ = 1.54056 Å) and a one-dimensional silicon strip detector (MYTHEN2 1K from DECTRIS). The line focused Cu X-ray tube was operated at 40 kV and 40 mA. Ar sorption isotherm measurements were performed on a Micromeritics ASAP-2020 (Micromeritics, Norcross, GA) at 87 K. The data points between 0.03 and 0.14 P/P0 were chosen for the BET surface area calculation to minimize the error for consistency criteria (R^2=0.9997). Between 30 and 50 mg of material was used for each measurement. The pore size distribution analysis was obtained by fitting the 2D-NLDFT model to the argon adsorption isotherms measured at 87 K. Inductively coupled plasma-optical emission spectroscopy (ICP-OES) was performed three times to measure the quantify the loading of Cyt c in NU-1000. The experiment was performed on QTEGRA software v. 2.2 Thermo iCap 7600 Duo ICP-OES (Thermo Fisher Scientific, Waltham, MA, USA) operating in standard mode. HNO_3 (1.5 mL) was added to 2-3 mg Cyt c@NU-1000 in a 5 mL microwave vial for digestion followed by 0.5 mL H_2O_2. After sealing, the vial was heating in a Biotage (Uppsala, Sweden) SPX microwave reactor (software version 2.3, build 6250) at 150 °C for 15 min. The solution was then diluted by Millipore water, and the ratio of Zr to S was determined by calibration curve of standard solutions. Diffuse reflectance UV-vis spectra of the solid MOF samples were recorded with a Shimadzu UV-3600 with a Harrick Praying Mantis diffuse reflectance accessory. Teflon was used as a perfect reflector for baseline

collection and the samples were diluted with Teflon for the measurements. The obtained reflectance spectra were converted to absorption spectra by using Kubelka–Munk function. $\alpha/S = (1 - R)^2(2R)^{-1}$ where R is the reflectance, α and S are the absorption and scattering coefficients, respectively. ITC experiments were performed using a VP-ITC titration microcalorimeter (MicroCal Inc.). [222] STEM-EDX analysis was performed using EPIC TEM JEOL ARM200CF operated at 200 keV and were acquired with probe size 8C and camera length 20 cm.

6.2.3 Sample Preparation for UV-Vis Measurements

To prepare the free Cyt c reaction mixture, 5 µL Cyt c solution (1g/L in tris buffer) and 27 µL ABTS solution (1g/L in tris buffer) were diluted with 995 µL of tris buffer. The reaction mixture was then transferred into quartz cuvette with an addition of 3 µL of 3% H_2O_2 solution before the measurement.

For Cyt c@NU-1000 reaction, 5 µL Cyt c solution (1g/L in tris buffer) was added to 0.5 mL NU-1000 suspension (0.06 g/L in Tris buffer) solution for 5 hours to ensure the encapsulation. Then 495 µL tris buffer and 27 µL ABTS solution (1g/L in tris buffer) were also added to form the Cyt c@NU-1000 reaction mixture. After the reaction mixture was transferred to the cuvette and loaded on the UV-Vis spectrometer, 3 µL of 3% H_2O_2 solution was added before the start of measurement.

6.2.4 Sample Preparation for Titration

Prior to the titration experiment, Cyt c@MOF (7.2 mg) and ABTS (0.6 mg) were mixed in 5 ml Tris buffer for 5 hours. All samples were degassed properly on a vacuum pump for 20 mins. Titrations were performed by injecting a solution of H_2O_2 into the ITC sample cell containing Cyt c@NU-1000 suspensions or Cyt c solutions. All titrations were carried out at pH 7.5 ± 0.1 in tris buffer under the following measurement conditions: reference power (10 µcal s^{-}

[1]), initial injection delay (600 s), stirring speed (307 rpm), feedback mode gain (high feedback), spacing between injections (500 s), and filter period (10 s). All titration experiments were performed in triplicate. Heats of dilution for H_2O_2 were determined in control experiments, and these were subtracted from the integrated data before obtaining heat flux. The transform of raw ITC results reaction rates was performed following the reported method.[222]

6.2.5 All-atom Explicit Solvent Molecular Dynamics Simulations

Free Cyt c was simulated by placing it in a cubic simulation box of approximately 9 nm per side and containing 24000 water molecules. The Cyt c charge (+6e) was balanced by 6 Cl^- counterions. The structure of cytochrome c (2b4z) was taken from the protein data bank.[223] The molecular interactions were modeled using the CHARMM36m force field parameters.[224] The system was equilibrated for 1 ns at T = 298 K and P = 1 bar using the Berendsen thermostat (τ_T = 0.5 ps) and barostat (τ_P = 1 ps). Then a production run was performed for a duration of 200 ns using the Nosé–Hoover thermostat (reference temperature 298 K, τ_T = 2 ps) and the Parrinello–Rahman barostat (reference pressure 1 bar, τP = 1 ps) to control the temperature and pressure, respectively. Similar results were found when the simulation was performed in the NVT (constant number of particles, volume and temperature) ensemble. A time-step of 2 fs was used to integrate Newton's equation of motion. Short-range interactions were truncated at 1.2 nm, and long-range electrostatic interactions were computed using the smooth particle mesh Ewald summation.[225-226] Three-dimensional periodic boundary conditions were applied. The simulations were performed using the Gromacs open source code.[227-228]

For confined Cyt c we employed the setup shown in (**Figure 6-2**) consisting of a slab of NU1000 MOF immersed in an aqueous solution. The slab was made of 2 × 2 × 4-unit cells of MOF NU-1000. We employed a box of rhombic symmetry in the x-y plane; the cell parameters

are a = 8 nm, b = 6.9 nm, c = 18.6 nm, α = 90, β = 90, and γ = 120 (**Figure 6-2** a). The NU-1000 slab thickness in the z-direction was approximately 6.6 nm but the simulation box was extended to 18.6 nm to include the aqueous solution and vacuum region, as demonstrated in **Figure 6-2** b. Cyt c was placed inside the NU-1000 nanopore before the system was solvated. The water phase was formed by 17000 water molecules which distributed inside the nanopores and formed two water layers adjacent to the MOF structure of at least 5 nm and a big empty space. The system was simulated employing 2D periodic boundary conditions in the x- and y- directions in the NVT ensemble. The atomic partial charge of the oxygen atoms (-0.667*e*) of $[Zr_6(\mu_3\text{-}O)_4(\mu_3\text{-}OH)_4(OH)_4]^{8+}$ was taken from the Zr6_MIX_node_S model in an earlier work.[229] The atomic partial charge of Zr was assigned to 2.169 *e*, and -0.65 *e* and 0.42 *e* for hydroxyl oxygen and hydrogen, respectively, to create the net charge of +8 *e* for one $[Zr_6(\mu_3\text{-}O)_4(\mu_3\text{-}OH)_4(OH)_4]^{8+}$ ion. The Lennard-Jones parameters of the Zr element were taken from the AMBER force field,[188] since they were missing from the CHARMM force field and the AMBER force field shares the same Lorentz-Berthelot combination rule for the nonbonded interactions with the CHARMM force field. The equilibrium bond lengths and angles of the $[Zr_6(\mu_3\text{-}O)_4(\mu_3\text{-}OH)_4(OH)_4]^{8+}$ ion were obtained from the crystal structure.

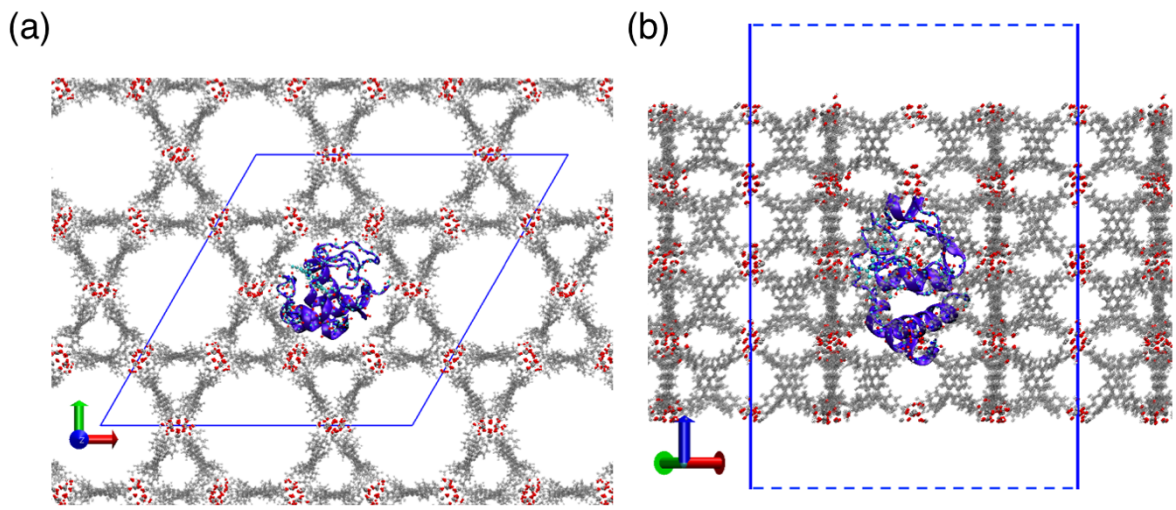

Figure 6-2 (a) Top and (b) side views of the simulation setup for Cyt c encapsulated inside MOF NU-1000. The MOF linkers are colored in grey whereas the protein backbone is in purple.

6.3 Results and Discussion

NU-1000 was synthesized and activated following the reported procedure.[221] The apparent Brunauer–Emmett–Teller (BET) surface area of the synthesized NU-1000 is estimated to be 2210 m^2/g, which is consistent with reported values.[221] The MOF crystals (~5 μm in length, **Figure 6-3**) were then soaked in Cyt c solution for 5 hours to ensure its encapsulation. Subsequently, the loading of Cyt c was measured with inductively coupled plasma-optical emission spectroscopy (ICP-OES) and found to be 6.4 wt% (based on the ratio of S to Zr). The N_2 uptake of Cyt c@NU-1000 decreases significantly comparing with that of the parent NU-1000, indicating the presence of Cyt c in the MOF (**Figure 6-4** a). The pore size distribution calculated via density function theory (DFT) also shows a decrease in the mesopore volume due to the presence of the enzyme within the mesopore (**Figure 6-5**). Powder X-ray diffraction (PXRD) patterns confirm that the bulk crystallinity of NU-1000 is retained after Cyt c encapsulation (**Figure 6-4** b). The change in relative intensity of the low angle peaks at 2.5° and

5° also indicates the occupancy of large guest molecules in the mesopores of the MOF.[156, 214] Elemental mappings of S and Fe by scanning transmission electron microscopy with energy dispersive X-ray spectroscopy (STEM-EDX) illustrate the uniform distribution of Cyt c through the MOF particle (**Figure 6-4** c).

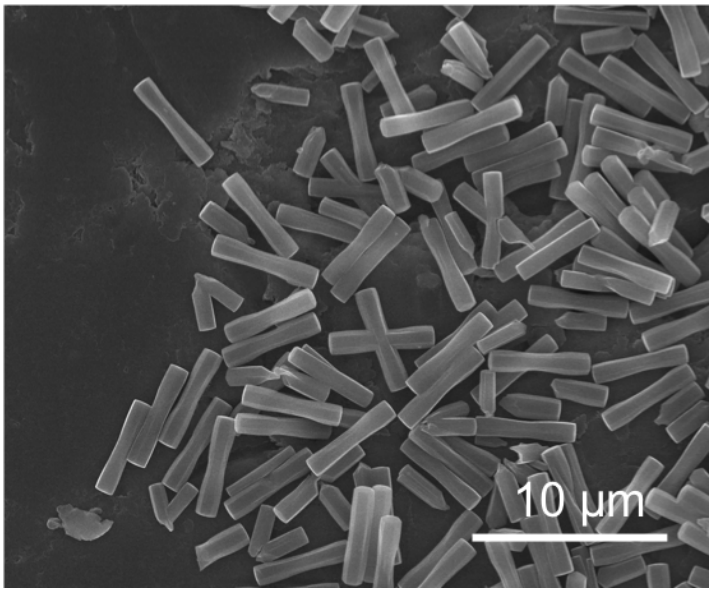

Figure 6-3 SEM image of NU-1000.

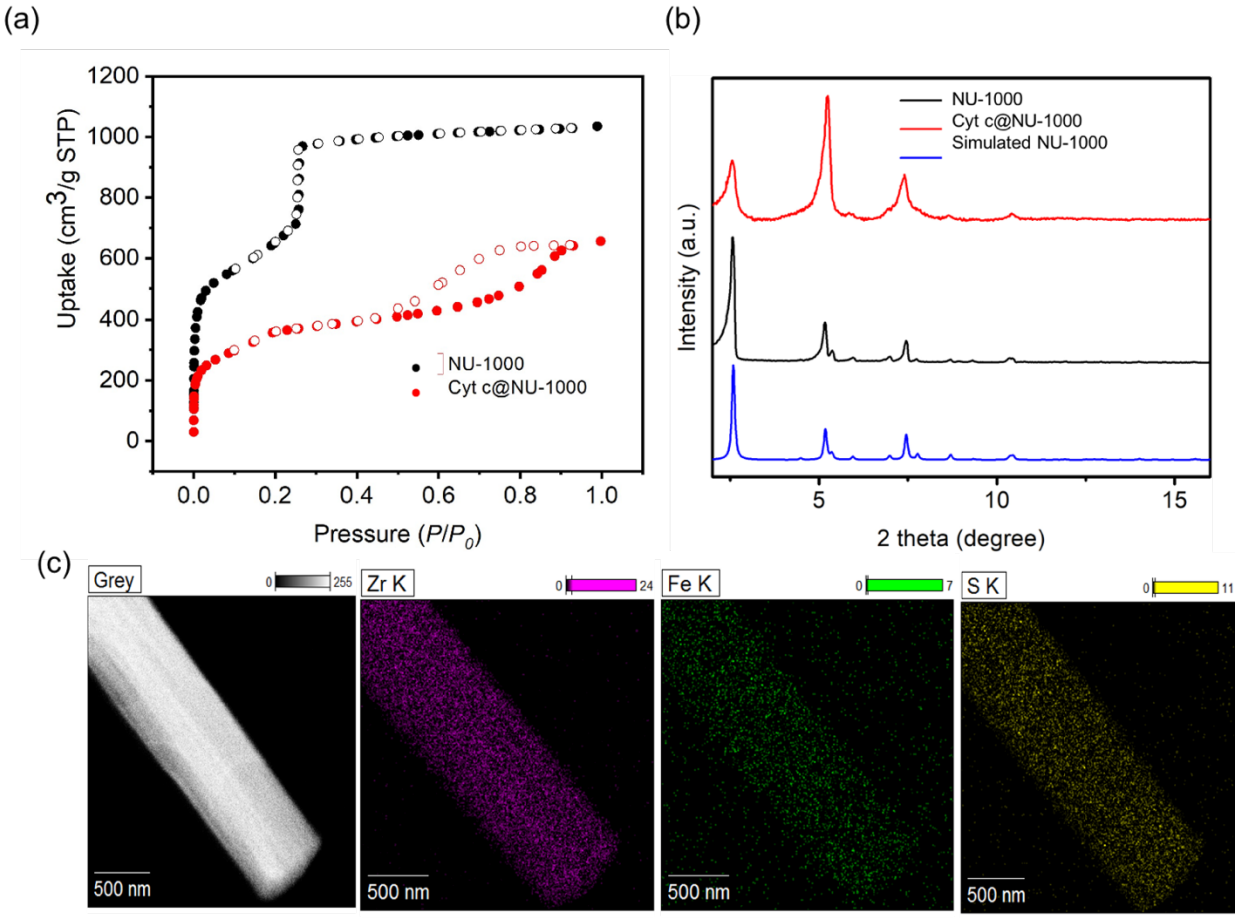

Figure 6-4 (a) N_2 isotherms of NU-1000 and Cyt c@NU-1000. (b) PXRD patterns of simulated NU-1000, NU-1000 and Cyt c@NU-1000. (c) STEM-EDX elemental mappings of Zr from NU-1000 and Fe, S from Cyt c in Cyt c@NU-1000.

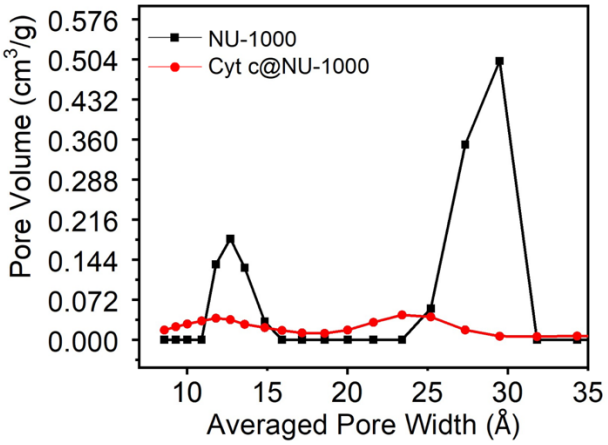

Figure 6-5 Pore size distribution of NU-1000 and Cyt c@NU-1000.

After confirming Cyt c was encapsulated within the mesopores of NU-1000, the oxidation rate of ABTS with hydrogen peroxide, catalyzed by free Cyt c, was compared with that by Cyt c@NU-1000 using ultraviolet–visible spectroscopy (UV-Vis) and isothermal titration calorimetry (ITC).[230-231] In the UV-Vis measurement, the remaining ABTS in reaction mixture was quantified by measuring the absorbance at 341 nm. The light scattering effect of MOF particles (0.03 g/L) does not affect the accuracy of ABTS quantification condition by UV-Vis under these dilute conditions (**Figure 6-6** and **Figure 6-7**).[232] After adding H_2O_2 to the reaction mixture, the oxidation of ABTS catalyzed by Cyt c@NU-1000 is approximately twice as fast as that of free Cyt c (**Figure 6-8** a), even after subtraction of the background adsorption of ABTS in NU-1000 suspension as a blank control. We have also determined the Michaelis−Menten kinetics of free Cyt c and Cyt c@NU-1000. (**Figure 6-9**). Cyt c shows a significant decrease in K_m value (from 123 mM to 20 mM) after being encapsulated within MOF NU-1000, suggesting that the encapsulated Cyt c has a higher substrate affinity. The k_{cat}/K_m value of Cyt c@NU-1000 (0.010 $mM^{-1}s^{-1}$) is also larger than that of free Cyt c (0.008 $mM^{-1}s^{-1}$), indicating a better enzyme catalytic performance. To confirm the high reaction rate of Cyt c@NU-1000, ABTS oxidation rates of the catalysts were also measured with ITC (**Figure 6-8** b). During this measurement, H_2O_2 (3.4 mM) was injected into pre-mixed ABTS and Cyt c/Cyt c@NU-1000 solutions, and the changes in heat flow were monitored. Injection of H_2O_2 into an ABTS solution was measured and subtracted as background. The thermodynamic information gained by ITC results suggest that after injecting the same amount of H_2O_2 within the period time, the ABTS oxidation catalyzed by Cyt c@NU-1000 releases more heat than free Cyt c. The heat release of H_2O_2 injecting into ABTS solution contains bare NU-1000 was subtracted as background when calculating the heat release of Cyt c@NU-1000. These results agree with the reaction rates

observed with UV-Vis measurements, indicating that after being encapsulated with NU-1000, Cyt c shows a better catalytic performance.

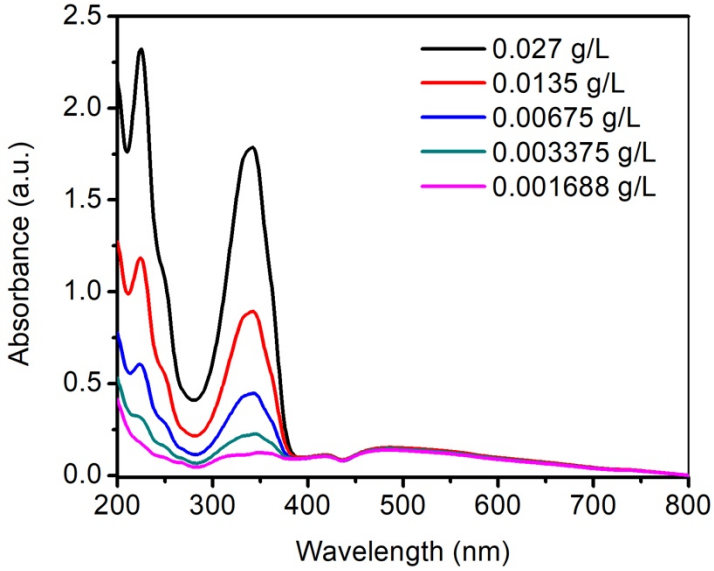

Figure 6-6 Absorption spectrum of ABTS at different concentrations.

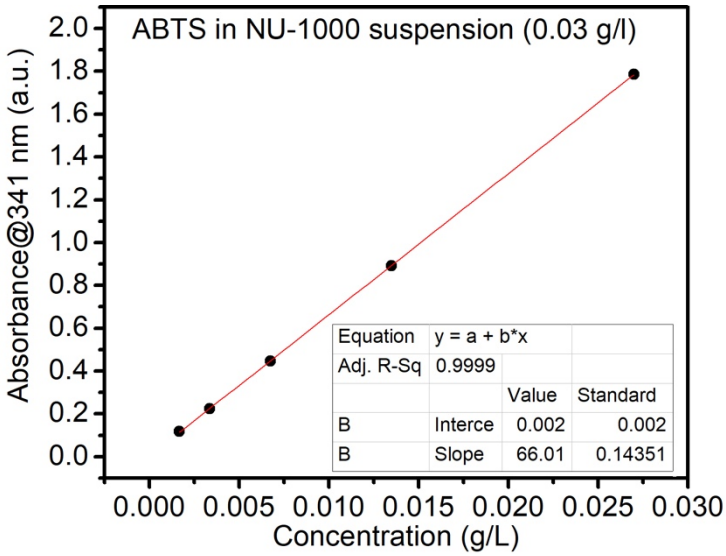

Figure 6-7 Standard curve of ABTS in 0.03 g/L MOF suspension measured by UV-vis.

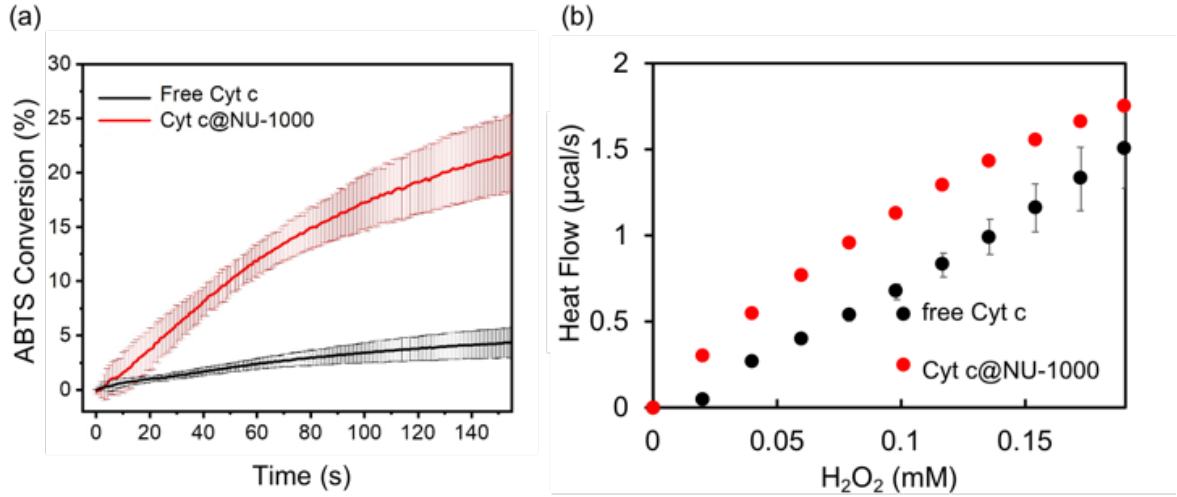

Figure 6-8. (a) The converted ABTS in solution after oxidation reaction catalyzed by Cyt c and Cyt c@NU-1000 measured by disappearance of 341 nm band in the UV-Vis. All experiments are triplicated, and the standard deviation of each time point is shown as error bar. (b) The analyzed calorimetric data for the multiple injections of H_2O_2 into ABTS solutions that contain Cyt c or Cyt c@NU-1000.

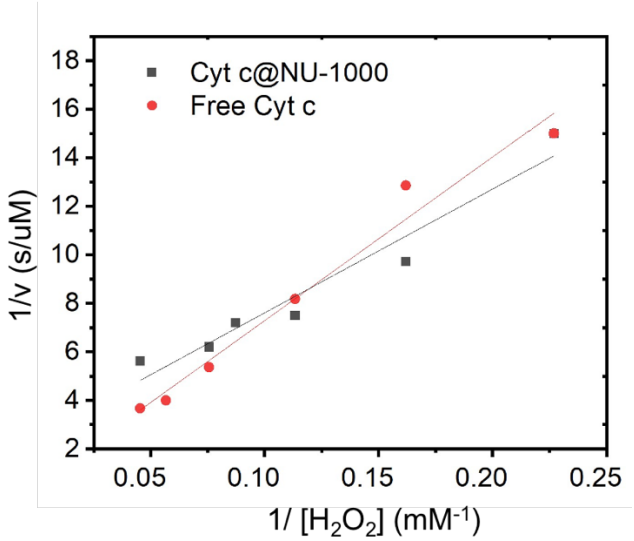

Figure 6-9 Double reciprocal plots of H_2O_2 concentrations with activities of Cyt c@NU-1000 and free Cyt c.

To investigate if the enhanced reaction rate is resulted from the structural change of Cyt c upon encapsulation, the coordination environment of the active centers of free Cyt c and Cyt c@NU-1000 was investigated by electron paramagnetic resonance (EPR) spectroscopy. The native enzyme shows a feature at g = 6 (115 mT), corresponding to a high spin ferric heme and

low spin ferric heme with g-values [3.0 2.2, 2.0], these agree well with literature (**Figure 6-10** a).[233] Upon encapsulation with NU-1000, there is a loss of the signal associated with the low spin heme species and a new feature at g = 4.3. Ferric iron with a g-value of 4.3 is commonly associated with non-heme iron or iron in a rhombic, low symmetry environment.[233] This result indicates that the coordination environment of the iron in Cyt c is significantly perturbed upon encapsulation in NU-1000. This change in active center spin configuration of Cyt c confined in pores of NU-1000 could result in the enhanced activity because the active centers of enzymes are highly related to an enzyme's catalytic performance. Solid-state UV-Vis was also utilized to elucidate of the structure of encapsulated Cyt c. The red shift in Soret band (~410 nm) of Cyt c@NU-1000 from Cyt c indicates the change in microenvironment of the heme active center induced by MOF adsorption (**Figure 6-10** b). On the other hand, this shift is not observed in the physical mixture of Cyt c and NU-1000 powder, ruling out the interference of the absorbance from NU-1000. In addition, increase in the charge transfer band (~ 700 nm) and the band at 620 nm has been observed in the encapsulated Cyt c, which can also be attributed to the increased amount of high spin Fe species in the immobilized sample, corroborating our observation in the EPR studies.[234]

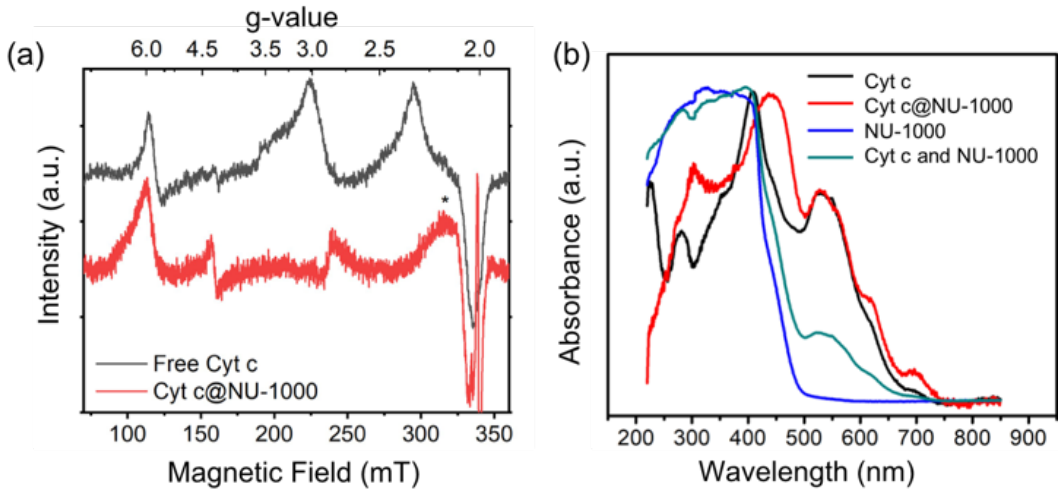

Figure 6-10 (a) The EPR spectra of free Cyt c and Cyt c@NU-1000 collected at 20 K. The copper background is denoted with an asterisk. (b) Normalized diffuse reflective UV-Vis of free Cyt c, Cytc@NU-1000, NU-1000 and the physical mixture of Cyt c and NU-1000.

All-atom explicit solvent molecular dynamics (MD) simulations were also performed to provide a deeper understanding of the structural changes in Cyt c upon encapsulation in the mesopores of NU-1000. The coordination environment of the heme active center of free Cyt c and Cyt c@NU-1000 was determined by tracking the change in distances between the designated atoms N (His 18), S (Met 80), C (Pro 30) and Fe. Specifically, we calculated the probability distribution function P(D), which shows the probability of the specified atom at a distance D from the Fe active site. When looking at the structure of free Cyt c, the distances between Fe to N (His 18), to S (Met 80) and to C (Pro 30) are 0.21 ± 0.03 nm, 0.46 ± 0.03 and 0.73 ± 0.06 nm, respectively (**Figure 6-11** a). The sharp distributions (and the corresponding small standard deviations) of N (His80) and S (Met80) suggest that their positions are highly localized, whereas C (Pro 30) is more delocalized. The coordination of these atoms changed significantly when Cyt c was encapsulated inside the NU-1000 (**Figure 6-11** b). The N (His 18) and S (Met 80) atoms are distributed farther from the heme Fe site in Cyt c@NU-1000, comparing with the free state; the average distance between Fe to N (His 18) and to S (Met 80) have increased to 0.56 ± 0.05

nm and 0.58 ± 0.06 nm, respectively. Additionally, the N (His 18) and S (Met 80) atoms in Cyt c@NU-1000 are more delocalized than those in the free Cyt c, as evidenced by the larger standard deviations. On the other hand, C (Pro 30) atom is more localized and becomes closer to Fe in the confined Cyt c with the distance of 0.34 ± 0.04 nm. The snapshots of Cyt c in the free state and encapsulated inside NU-1000 portray the region around the heme cofactor featuring the His 18, Met 80, and Pro 30 amino acids in Cyt c (**Figure 6-11** c & **Figure 6-11** d). In the free Cyt c, the N (His 18) atom is found on a different side of the heme active center from the S (Met 80) atom. The C (Pro 30) is located farther from the active center and on the same side as N (His 18). When Cyt c is encapsulated in NU-1000, the N (His 18) and S (Met 80) atoms are displaced farther away from the Fe site, whereas the C (Pro 30) atom becomes closer to the Fe atom. The configurational changes observed in the MD simulations agree with the EPR spectra changes as well as the DR-UV-Vis results; however, what we have observed is different from the conventional hypothesis that the replacing of Met 80 with a water molecule is the structural change in encapsulated Cyt c that results in the change of spin state of the Fe in its active center.[235-236]

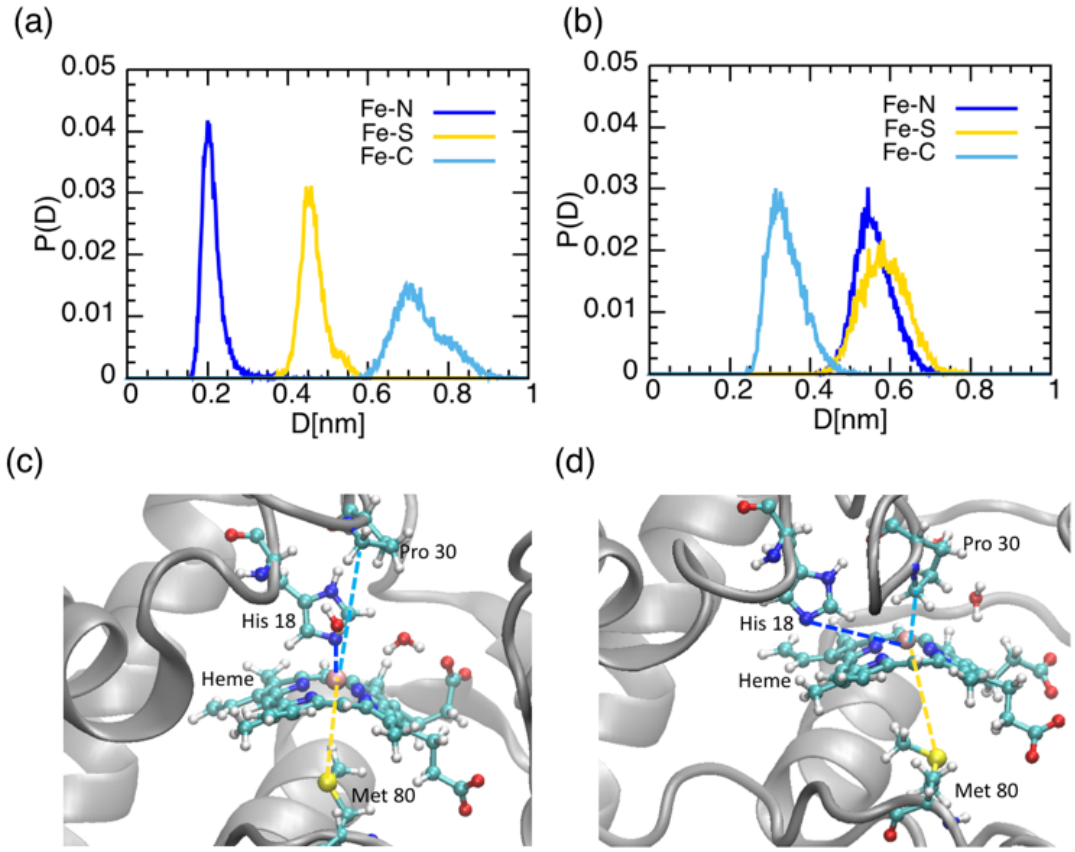

Figure 6-11 NU-1000 encapsulation changes the coordination of the Cyt c heme active site. Probability distributions, P(D), of N (His 18), S (Met 80), and C (Pro 30) distances relative to Fe, (a) in bulk and (b) inside MOF NU-1000. The configurations of Cyt C in water (c) and inside MOF NU-1000 (d); the snapshots show the protein's backbone (gray), the heme cofactor (Heme), the amino acids His 18, Met 80, Pro 30 and the nearby water molecules. The atomic color code is as follows: blue, N; pink, Fe; cyan, C; yellow, S; red, O; white, H.

The distribution and quantity of water molecules are also found to be different in free Cyt c and encapsulated Cyt (**Figure 6-11**). In the free state, the radial distribution function g(r) of the water oxygen atoms as a function of the distance to Fe site shows a well-defined peak at r = 0.4 nm as an indication of the water molecules localized nearby the active site. The peak, however, is not observed when Cyt c is inside the MOF, indicating the diffusive feature of neighboring water molecules. The calculation of the total number of neighboring water molecules implies that more

water molecules are found within 1 nm from the Fe site in the confined Cyt c than in the free Cyt c. The better access of water to the heme active site is caused by a partial unfolding of the protein's backbone due to the non-polar interaction of Cyt c and NU1000 (**Figure 6-11**). Polar amino acids stabilize the interaction of the heme cofactor and water .[237] The increased amount of water molecules located at inner protein region of encapsulated Cyt c may indicate a better accessibility of the water-soluble reaction substrate (such as ABTS and H_2O_2) to the active center and consequently facilitate catalysis, agreeing with the decreased K_m values of encapsulated Cyt c.

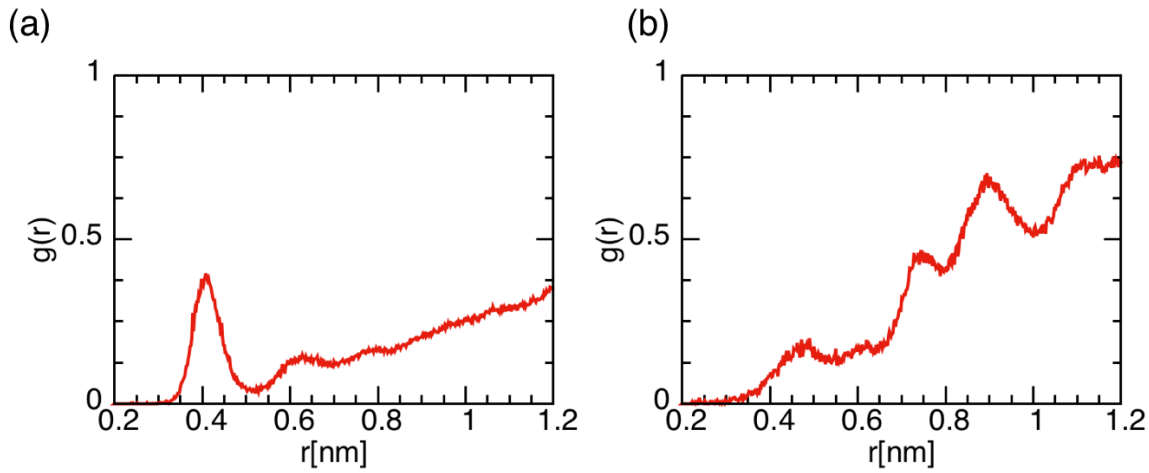

Figure 6-12 Radial distribution function g(r) of the water oxygen atoms as a function of the distance to heme Fe atom for Cyt c (a) free and (b) inside the NU-1000.

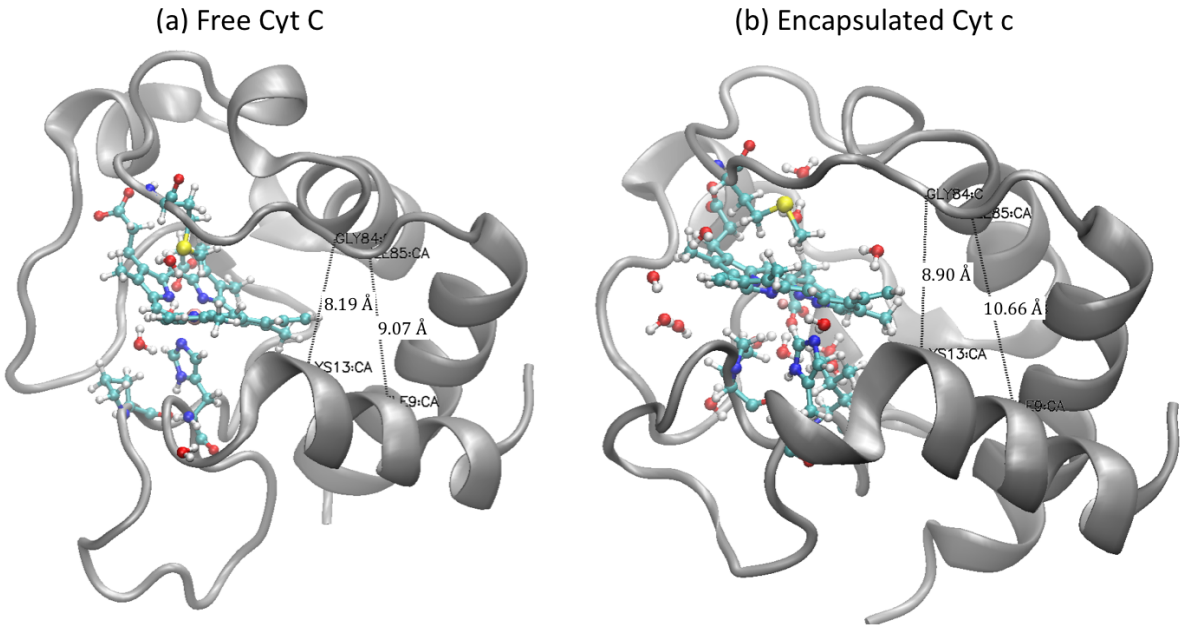

Figure 6-13. Instantaneous snapshots showing that the entrance to the Cyt c heme active site widens upon encapsulation by NU-1000. The separation distance between the backbone atoms Lys13:Cα to Gly84:C and between Ile85:Cα to ILE9:CA of Cyt c (a) free and (b) inside the NU-1000. Confinement increases of the separation distances (partial unfolding of Cyt c) allowing a better access of water into the heme region. The water molecules are shown within 8 Å of Fe.

6.4 Conclusions

In conclusion, we have employed Cyt c as a model to investigate the structures and behaviors of encapsulated enzymes in MOFs with a combination of experimental and computational techniques. Upon encapsulation, Cyt c@NU-1000 catalyzes the oxidation of ABTS at a faster rate than free Cyt c, verified by both UV-Vis and ITC. After comparing the structures of encapsulated Cyt c with its native state using EPR, solid-state UV-Vis and MD simulation, we have discovered that the enzyme structure around its active center is different when the enzyme is encapsulated, likely resulting in enhanced accessibility of the active center to reaction substrates. It is possible that the alteration in enzyme strucuture and enhanced catalytic performance could result from the hydrophilic/hydrophobic interactions between the

organic linker and the enzyme. In short, we have taken advantage of the crystalline nature of MOFs to elucidate the structure of a complex enzyme and exploited these structural changes that improved its catalytic activity. This work sheds light on the complex relationship between enzyme structures and porous supports and provides new opportunities in designing other supported enzymatic systems with enhanced catalytic activity and stability.

References

1. Manning, M. C.; Chou, D. K.; Murphy, B. M.; Payne, R. W.; Katayama, D. S., Stability of protein pharmaceuticals: an update. *Pharmaceutical research* **2010,** *27* (4), 544-575.
2. Wilcox, G., Insulin and insulin resistance. *Clinical biochemist reviews* **2005,** *26* (2), 19.
3. Chudakov, D. M.; Matz, M. V.; Lukyanov, S.; Lukyanov, K. A., Fluorescent proteins and their applications in imaging living cells and tissues. *Physiological reviews* **2010,** *90* (3), 1103-1163.
4. Kirk, O.; Borchert, T. V.; Fuglsang, C. C., Industrial enzyme applications. *Current opinion in biotechnology* **2002,** *13* (4), 345-351.
5. Jiskoot, W.; Randolph, T. W.; Volkin, D. B.; Middaugh, C. R.; Schöneich, C.; Winter, G.; Friess, W.; Crommelin, D. J.; Carpenter, J. F., Protein instability and immunogenicity: roadblocks to clinical application of injectable protein delivery systems for sustained release. *Journal of pharmaceutical sciences* **2012,** *101* (3), 946-954.
6. Rabe, M.; Verdes, D.; Seeger, S., Understanding protein adsorption phenomena at solid surfaces. *Advances in colloid and interface science* **2011,** *162* (1-2), 87-106.
7. Wong, L. S.; Khan, F.; Micklefield, J., Selective covalent protein immobilization: strategies and applications. *Chem. Rev.* **2009,** *109* (9), 4025-4053.
8. Hartmann, M.; Kostrov, X., Immobilization of enzymes on porous silicas–benefits and challenges. *Chem. Soc. Rev.* **2013,** *42* (15), 6277-6289.
9. Branco, M. C.; Pochan, D. J.; Wagner, N. J.; Schneider, J. P., The effect of protein structure on their controlled release from an injectable peptide hydrogel. *Biomaterials* **2010,** *31* (36), 9527-9534.
10. Lee, F.; Chung, J. E.; Kurisawa, M., An injectable hyaluronic acid–tyramine hydrogel system for protein delivery. *Journal of Controlled Release* **2009,** *134* (3), 186-193.
11. Tu, J.; Boyle, A. L.; Friedrich, H.; Bomans, P. H.; Bussmann, J.; Sommerdijk, N. A.; Jiskoot, W.; Kros, A., Mesoporous silica nanoparticles with large pores for the encapsulation and release of proteins. *ACS applied materials & interfaces* **2016,** *8* (47), 32211-32219.
12. Urabe, Y.; Shiomi, T.; Itoh, T.; Kawai, A.; Tsunoda, T.; Mizukami, F.; Sakaguchi, K., Encapsulation of hemoglobin in mesoporous silica (FSM)—enhanced thermal stability and resistance to denaturants. *ChemBioChem* **2007,** *8* (6), 668-674.
13. Kumari, A.; Kayastha, A. M., Immobilization of soybean (Glycine max) α-amylase onto Chitosan and Amberlite MB-150 beads: Optimization and characterization. *J. Mol. Catal. B Enzym.* **2011,** *69* (1-2), 8-14.
14. Labus, K.; Turek, A.; Liesiene, J.; Bryjak, J., Efficient Agaricus bisporus tyrosinase immobilization on cellulose-based carriers. *Biochemical engineering journal* **2011,** *56* (3), 232-240.
15. Kirchon, A.; Feng, L.; Drake, H. F.; Joseph, E. A.; Zhou, H.-C., From fundamentals to applications: a toolbox for robust and multifunctional MOF materials. *Chem. Soc. Rev.* **2018,** *47* (23), 8611-8638.
16. Alezi, D.; Belmabkhout, Y.; Suyetin, M.; Bhatt, P. M.; Weseliński, Ł. J.; Solovyeva, V.; Adil, K.; Spanopoulos, I.; Trikalitis, P. N.; Emwas, A.-H., MOF crystal chemistry paving the way to gas storage needs: aluminum-based soc-MOF for CH4, O2, and CO2 storage. *J. Am. Chem. Soc.* **2015,** *137* (41), 13308-13318.

17. Fu, J.; Das, S.; Xing, G.; Ben, T.; Valtchev, V.; Qiu, S., Fabrication of COF-MOF composite membranes and their highly selective separation of H2/CO2. *J. Am. Chem. Soc.* **2016,** *138* (24), 7673-7680.
18. Hamon, L.; Llewellyn, P. L.; Devic, T.; Ghoufi, A.; Clet, G.; Guillerm, V.; Pirngruber, G. D.; Maurin, G.; Serre, C.; Driver, G., Co-adsorption and separation of CO2− CH4 mixtures in the highly flexible MIL-53 (Cr) MOF. *J. Am. Chem. Soc.* **2009,** *131* (47), 17490-17499.
19. Kato, S.; Otake, K.-i.; Chen, H.; Akpinar, I.; Buru, C. T.; Islamoglu, T.; Snurr, R. Q.; Farha, O. K., Zirconium-based metal–organic frameworks for the removal of protein-bound uremic toxin from human serum albumin. *J. Am. Chem. Soc.* **2019,** *141* (6), 2568-2576.
20. Gu, J.; Fan, H.; Li, C.; Caro, J.; Meng, H., Robust superhydrophobic/superoleophilic wrinkled microspherical MOF@ rGO composites for efficient oil–water separation. *Angew. Chem. Int. Ed.* **2019,** *58* (16), 5297-5301.
21. Shen, K.; Chen, X.; Chen, J.; Li, Y., Development of MOF-derived carbon-based nanomaterials for efficient catalysis. *ACS Catal.* **2016,** *6* (9), 5887-5903.
22. Wang, Q.; Astruc, D., State of the art and prospects in metal–organic framework (MOF)-based and MOF-derived nanocatalysis. *Chem. Rev.* **2019,** *120* (2), 1438-1511.
23. Tchalala, M.; Bhatt, P.; Chappanda, K.; Tavares, S.; Adil, K.; Belmabkhout, Y.; Shkurenko, A.; Cadiau, A.; Heymans, N.; De Weireld, G., Fluorinated MOF platform for selective removal and sensing of SO 2 from flue gas and air. *Nat. Commun.* **2019,** *10* (1), 1-10.
24. Lian, X.; Fang, Y.; Joseph, E.; Wang, Q.; Li, J.; Banerjee, S.; Lollar, C.; Wang, X.; Zhou, H.-C., Enzyme–MOF (metal–organic framework) composites. *Chem. Soc. Rev.* **2017,** *46* (11), 3386-3401.
25. Wang, H.; Han, L.; Zheng, D.; Yang, M.; Andaloussi, Y. H.; Cheng, P.; Zhang, Z.; Ma, S.; Zaworotko, M. J.; Feng, Y., Protein-structure-directed metal–organic zeolite-like networks as biomacromolecule carriers. *Angew. Chem. Int. Ed.* **2020,** *59* (15), 6263-6267.
26. Datta, S.; Christena, L. R.; Rajaram, Y. R. S., Enzyme immobilization: an overview on techniques and support materials. *3 Biotech* **2013,** *3* (1), 1-9.
27. Reusch, J. E.; Manson, J. E., Management of type 2 diabetes in 2017: getting to goal. *Jama* **2017,** *317* (10), 1015-1016.
28. Luo, J.; Gellad, W. F., Origins of the crisis in insulin affordability and practical advice for clinicians on using human insulin. *Current Diabetes Reports* **2020,** *20* (1), 2.
29. Care, D., Economic costs of diabetes in the US in 2012. **2013**.
30. Alberti, K. G. M. M.; Zimmet, P. Z., Definition, diagnosis and classification of diabetes mellitus and its complications. Part 1: diagnosis and classification of diabetes mellitus. Provisional report of a WHO consultation. *Diabetic medicine* **1998,** *15* (7), 539-553.
31. Reaven, G. M., Role of insulin resistance in human disease. *Diabetes* **1988,** *37* (12), 1595-1607.
32. Bourbon, A. I.; Pinheiro, A. C.; Cerqueira, M. A.; Vicente, A. A., Influence of chitosan coating on protein-based nanohydrogels properties and in vitro gastric digestibility. *Food Hydrocolloids* **2016,** *60*, 109-118.
33. Malmberg, K., Prospective randomised study of intensive insulin treatment on long term survival after acute myocardial infarction in patients with diabetes mellitus. *Bmj* **1997,** *314* (7093), 1512.

34. Guggi, D.; Krauland, A. H.; Bernkop-Schnürch, A., Systemic peptide delivery via the stomach: in vivo evaluation of an oral dosage form for salmon calcitonin. *Journal of controlled release* **2003,** *92* (1-2), 125-135.
35. Zhang, Y.; Wei, W.; Lv, P.; Wang, L.; Ma, G., Preparation and evaluation of alginate–chitosan microspheres for oral delivery of insulin. *European Journal of pharmaceutics and biopharmaceutics* **2011,** *77* (1), 11-19.
36. Silva, C. M.; Ribeiro, A. J.; Figueiredo, I. V.; Gonçalves, A. R.; Veiga, F., Alginate microspheres prepared by internal gelation: Development and effect on insulin stability. *International journal of pharmaceutics* **2006,** *311* (1-2), 1-10.
37. Sarmento, B.; Martins, S.; Ferreira, D.; Souto, E. B., Oral insulin delivery by means of solid lipid nanoparticles. *International journal of nanomedicine* **2007,** *2* (4), 743.
38. Gu, Z.; Dang, T. T.; Ma, M.; Tang, B. C.; Cheng, H.; Jiang, S.; Dong, Y.; Zhang, Y.; Anderson, D. G., Glucose-responsive microgels integrated with enzyme nanocapsules for closed-loop insulin delivery. *ACS nano* **2013,** *7* (8), 6758-6766.
39. Yaoi, Y.; Hashimoto, K.; Takahara, K.; Kato, I., Insulin binds to type V collagen with retention of mitogenic activity. *Experimental cell research* **1991,** *194* (2), 180-185.
40. Chen, M.-C.; Sonaje, K.; Chen, K.-J.; Sung, H.-W., A review of the prospects for polymeric nanoparticle platforms in oral insulin delivery. *Biomaterials* **2011,** *32* (36), 9826-9838.
41. Khafagy, E.-S.; Morishita, M.; Onuki, Y.; Takayama, K., Current challenges in non-invasive insulin delivery systems: a comparative review. *Advanced drug delivery reviews* **2007,** *59* (15), 1521-1546.
42. Islamoglu, T.; Goswami, S.; Li, Z.; Howarth, A. J.; Farha, O. K.; Hupp, J. T., Postsynthetic tuning of metal–organic frameworks for targeted applications. *Accounts of chemical research* **2017,** *50* (4), 805-813.
43. Farha, O. K.; Yazaydın, A. Ö.; Eryazici, I.; Malliakas, C. D.; Hauser, B. G.; Kanatzidis, M. G.; Nguyen, S. T.; Snurr, R. Q.; Hupp, J. T., De novo synthesis of a metal–organic framework material featuring ultrahigh surface area and gas storage capacities. *Nature chemistry* **2010,** *2* (11), 944-948.
44. Liao, Y.; Zhang, L.; Weston, M. H.; Morris, W.; Hupp, J. T.; Farha, O. K., Tuning ethylene gas adsorption via metal node modulation: Cu-MOF-74 for a high ethylene deliverable capacity. *Chem. Commun.* **2017,** *53* (67), 9376-9379.
45. Goswami, S.; Miller, C. E.; Logsdon, J. L.; Buru, C. T.; Wu, Y.-L.; Bowman, D. N.; Islamoglu, T.; Asiri, A. M.; Cramer, C. J.; Wasielewski, M. R., Atomistic approach toward selective photocatalytic oxidation of a mustard-gas simulant: A case study with heavy-chalcogen-containing PCN-57 analogues. *ACS applied materials & interfaces* **2017,** *9* (23), 19535-19540.
46. Noh, H.; Cui, Y.; Peters, A. W.; Pahls, D. R.; Ortuño, M. A.; Vermeulen, N. A.; Cramer, C. J.; Gagliardi, L.; Hupp, J. T.; Farha, O. K., An exceptionally stable metal–organic framework supported molybdenum (VI) oxide catalyst for cyclohexene epoxidation. *J. Am. Chem. Soc.* **2016,** *138* (44), 14720-14726.
47. Li, P.; Klet, R. C.; Moon, S.-Y.; Wang, T. C.; Deria, P.; Peters, A. W.; Klahr, B. M.; Park, H.-J.; Al-Juaid, S. S.; Hupp, J. T., Synthesis of nanocrystals of Zr-based metal–organic frameworks with csq-net: significant enhancement in the degradation of a nerve agent simulant. *Chem. Commun.* **2015,** *51* (54), 10925-10928.

48. Bae, Y.-S.; Spokoyny, A. M.; Farha, O. K.; Snurr, R. Q.; Hupp, J. T.; Mirkin, C. A., Separation of gas mixtures using Co (II) carborane-based porous coordination polymers. *Chem. Commun.* **2010,** *46* (20), 3478-3480.
49. Teplensky, M. H.; Fantham, M.; Li, P.; Wang, T. C.; Mehta, J. P.; Young, L. J.; Moghadam, P. Z.; Hupp, J. T.; Farha, O. K.; Kaminski, C. F., Temperature treatment of highly porous zirconium-containing metal–organic frameworks extends drug delivery release. *J. Am. Chem. Soc.* **2017,** *139* (22), 7522-7532.
50. Horcajada, P.; Chalati, T.; Serre, C.; Gillet, B.; Sebrie, C.; Baati, T.; Eubank, J. F.; Heurtaux, D.; Clayette, P.; Kreuz, C., Porous metal–organic-framework nanoscale carriers as a potential platform for drug delivery and imaging. *Nature materials* **2010,** *9* (2), 172-178.
51. Zheng, H.; Zhang, Y.; Liu, L.; Wan, W.; Guo, P.; Nyström, A. M.; Zou, X., One-pot synthesis of metal–organic frameworks with encapsulated target molecules and their applications for controlled drug delivery. *J. Am. Chem. Soc.* **2016,** *138* (3), 962-968.
52. Dong, Z.; Sun, Y.; Chu, J.; Zhang, X.; Deng, H., Multivariate metal–organic frameworks for dialing-in the binding and programming the release of drug molecules. *J. Am. Chem. Soc.* **2017,** *139* (40), 14209-14216.
53. Della Rocca, J.; Liu, D.; Lin, W., Nanoscale metal–organic frameworks for biomedical imaging and drug delivery. *Accounts of chemical research* **2011,** *44* (10), 957-968.
54. Li, P.; Modica, J. A.; Howarth, A. J.; Vargas, E.; Moghadam, P. Z.; Snurr, R. Q.; Mrksich, M.; Hupp, J. T.; Farha, O. K., Toward design rules for enzyme immobilization in hierarchical mesoporous metal-organic frameworks. *Chem* **2016,** *1* (1), 154-169.
55. Wu, X.; Hou, M.; Ge, J., Metal–organic frameworks and inorganic nanoflowers: a type of emerging inorganic crystal nanocarrier for enzyme immobilization. *Catalysis Science & Technology* **2015,** *5* (12), 5077-5085.
56. Shieh, F.-K.; Wang, S.-C.; Yen, C.-I.; Wu, C.-C.; Dutta, S.; Chou, L.-Y.; Morabito, J. V.; Hu, P.; Hsu, M.-H.; Wu, K. C.-W., Imparting functionality to biocatalysts via embedding enzymes into nanoporous materials by a de novo approach: size-selective sheltering of catalase in metal–organic framework microcrystals. *J. Am. Chem. Soc.* **2015,** *137* (13), 4276-4279.
57. Deng, H.; Grunder, S.; Cordova, K. E.; Valente, C.; Furukawa, H.; Hmadeh, M.; Gándara, F.; Whalley, A. C.; Liu, Z.; Asahina, S., Large-pore apertures in a series of metal-organic frameworks. *science* **2012,** *336* (6084), 1018-1023.
58. Li, P.; Chen, Q.; Wang, T. C.; Vermeulen, N. A.; Mehdi, B. L.; Dohnalkova, A.; Browning, N. D.; Shen, D.; Anderson, R.; Gómez-Gualdrón, D. A., Hierarchically engineered mesoporous metal-organic frameworks toward cell-free immobilized enzyme systems. *Chem* **2018,** *4* (5), 1022-1034.
59. Majewski, M. B.; Howarth, A. J.; Li, P.; Wasielewski, M. R.; Hupp, J. T.; Farha, O. K., Enzyme encapsulation in metal–organic frameworks for applications in catalysis. *CrystEngComm* **2017,** *19* (29), 4082-4091.
60. Lyu, F.; Zhang, Y.; Zare, R. N.; Ge, J.; Liu, Z., One-pot synthesis of protein-embedded metal–organic frameworks with enhanced biological activities. *Nano Lett.* **2014,** *14* (10), 5761-5765.
61. Liang, K.; Ricco, R.; Doherty, C. M.; Styles, M. J.; Bell, S.; Kirby, N.; Mudie, S.; Haylock, D.; Hill, A. J.; Doonan, C. J., Biomimetic mineralization of metal-organic frameworks as protective coatings for biomacromolecules. *Nat. Commun.* **2015,** *6* (1), 1-8.

62. Chen, Y.; Lykourinou, V.; Hoang, T.; Ming, L.-J.; Ma, S., Size-selective biocatalysis of myoglobin immobilized into a mesoporous metal–organic framework with hierarchical pore sizes. *Inorganic chemistry* **2012,** *51* (17), 9156-9158.
63. Lykourinou, V.; Chen, Y.; Wang, X.-S.; Meng, L.; Hoang, T.; Ming, L.-J.; Musselman, R. L.; Ma, S., Immobilization of MP-11 into a mesoporous metal–organic framework, MP-11@ mesoMOF: a new platform for enzymatic catalysis. *J. Am. Chem. Soc.* **2011,** *133* (27), 10382-10385.
64. Howarth, A. J.; Liu, Y.; Li, P.; Li, Z.; Wang, T. C.; Hupp, J. T.; Farha, O. K., Chemical, thermal and mechanical stabilities of metal–organic frameworks. *Nature Reviews Materials* **2016,** *1* (3), 1-15.
65. Deria, P.; Bury, W.; Hupp, J. T.; Farha, O. K., Versatile functionalization of the NU-1000 platform by solvent-assisted ligand incorporation. *Chem. Commun.* **2014,** *50* (16), 1965-1968.
66. Deria, P.; Chung, Y. G.; Snurr, R. Q.; Hupp, J. T.; Farha, O. K., Water stabilization of Zr 6-based metal–organic frameworks via solvent-assisted ligand incorporation. *Chem. Sci.* **2015,** *6* (9), 5172-5176.
67. Wang, T. C.; Vermeulen, N. A.; Kim, I. S.; Martinson, A. B.; Stoddart, J. F.; Hupp, J. T.; Farha, O. K., Scalable synthesis and post-modification of a mesoporous metal-organic framework called NU-1000. *Nature protocols* **2016,** *11* (1), 149-162.
68. D'Astolfo, D. S.; Pagliero, R. J.; Pras, A.; Karthaus, W. R.; Clevers, H.; Prasad, V.; Lebbink, R. J.; Rehmann, H.; Geijsen, N., Efficient intracellular delivery of native proteins. *Cell* **2015,** *161* (3), 674-690.
69. Hoffman, R. M., Green fluorescent protein imaging of tumour growth, metastasis, and angiogenesis in mouse models. *The lancet oncology* **2002,** *3* (9), 546-556.
70. Torchilin, V., Intracellular delivery of protein and peptide therapeutics. *Drug Discovery Today: Technologies* **2008,** *5* (2-3), e95-e103.
71. Desnick, R. J.; Schuchman, E. H., Enzyme replacement and enhancement therapies: lessons from lysosomal disorders. *Nature Reviews Genetics* **2002,** *3* (12), 954-966.
72. Leader, B.; Baca, Q. J.; Golan, D. E., Protein therapeutics: a summary and pharmacological classification. *Nature reviews Drug discovery* **2008,** *7* (1), 21-39.
73. Petros, R. A.; DeSimone, J. M., Strategies in the design of nanoparticles for therapeutic applications. *Nature reviews Drug discovery* **2010,** *9* (8), 615-627.
74. Ghosh, P.; Yang, X.; Arvizo, R.; Zhu, Z.-J.; Agasti, S. S.; Mo, Z.; Rotello, V. M., Intracellular delivery of a membrane-impermeable enzyme in active form using functionalized gold nanoparticles. *J. Am. Chem. Soc.* **2010,** *132* (8), 2642-2645.
75. Gu, Z.; Biswas, A.; Zhao, M.; Tang, Y., Tailoring nanocarriers for intracellular protein delivery. *Chem. Soc. Rev.* **2011,** *40* (7), 3638-3655.
76. Xu, X.; Costa, A.; Burgess, D. J., Protein encapsulation in unilamellar liposomes: high encapsulation efficiency and a novel technique to assess lipid-protein interaction. *Pharmaceutical research* **2012,** *29* (7), 1919-1931.
77. Schwarze, S. R.; Ho, A.; Vocero-Akbani, A.; Dowdy, S. F., In vivo protein transduction: delivery of a biologically active protein into the mouse. *Science* **1999,** *285* (5433), 1569-1572.
78. Lawrence, M. S.; Phillips, K. J.; Liu, D. R., Supercharging proteins can impart unusual resilience. *J. Am. Chem. Soc.* **2007,** *129* (33), 10110-10112.

79. Cronican, J. J.; Thompson, D. B.; Beier, K. T.; McNaughton, B. R.; Cepko, C. L.; Liu, D. R., Potent delivery of functional proteins into Mammalian cells in vitro and in vivo using a supercharged protein. *ACS chemical biology* **2010,** *5* (8), 747-752.
80. Brodin, J. D.; Sprangers, A. J.; McMillan, J. R.; Mirkin, C. A., DNA-mediated cellular delivery of functional enzymes. *J. Am. Chem. Soc.* **2015,** *137* (47), 14838-14841.
81. Fu, A.; Tang, R.; Hardie, J.; Farkas, M. E.; Rotello, V. M., Promises and pitfalls of intracellular delivery of proteins. *Bioconjugate chemistry* **2014,** *25* (9), 1602-1608.
82. Mirkin, C. A.; Letsinger, R. L.; Mucic, R. C.; Storhoff, J. J., A DNA-based method for rationally assembling nanoparticles into macroscopic materials. *Nature* **1996,** *382* (6592), 607-609.
83. Patel, P. C.; Giljohann, D. A.; Daniel, W. L.; Zheng, D.; Prigodich, A. E.; Mirkin, C. A., Scavenger receptors mediate cellular uptake of polyvalent oligonucleotide-functionalized gold nanoparticles. *Bioconjugate chemistry* **2010,** *21* (12), 2250-2256.
84. Choi, C. H. J.; Hao, L.; Narayan, S. P.; Auyeung, E.; Mirkin, C. A., Mechanism for the endocytosis of spherical nucleic acid nanoparticle conjugates. *Proc. Natl. Acad. Sci. U.S.A.* **2013,** *110* (19), 7625-7630.
85. Shih, Y. H.; Lo, S. H.; Yang, N. S.; Singco, B.; Cheng, Y. J.; Wu, C. Y.; Chang, I. H.; Huang, H. Y.; Lin, C. H., Trypsin-immobilized metal–organic framework as a biocatalyst in proteomics analysis. *ChemPlusChem* **2012,** *77* (11), 982-986.
86. Li, P.; Moon, S.-Y.; Guelta, M. A.; Harvey, S. P.; Hupp, J. T.; Farha, O. K., Encapsulation of a nerve agent detoxifying enzyme by a mesoporous zirconium metal–organic framework engenders thermal and long-term stability. *J. Am. Chem. Soc.* **2016,** *138* (26), 8052-8055.
87. Doonan, C.; Riccò, R.; Liang, K.; Bradshaw, D.; Falcaro, P., Metal–organic frameworks at the biointerface: synthetic strategies and applications. *Accounts of chemical research* **2017,** *50* (6), 1423-1432.
88. Gkaniatsou, E.; Sicard, C.; Ricoux, R.; Mahy, J.-P.; Steunou, N.; Serre, C., Metal–organic frameworks: a novel host platform for enzymatic catalysis and detection. *Materials Horizons* **2017,** *4* (1), 55-63.
89. Liu, W.-L.; Lo, S.-H.; Singco, B.; Yang, C.-C.; Huang, H.-Y.; Lin, C.-H., Novel trypsin–FITC@ MOF bioreactor efficiently catalyzes protein digestion. *Journal of Materials Chemistry B* **2013,** *1* (7), 928-932.
90. Cao, Y.; Wu, Z.; Wang, T.; Xiao, Y.; Huo, Q.; Liu, Y., Immobilization of Bacillus subtilis lipase on a Cu-BTC based hierarchically porous metal–organic framework material: a biocatalyst for esterification. *Dalton transactions* **2016,** *45* (16), 6998-7003.
91. Lian, X.; Erazo-Oliveras, A.; Pellois, J.-P.; Zhou, H.-C., High efficiency and long-term intracellular activity of an enzymatic nanofactory based on metal-organic frameworks. *Nat. Commun.* **2017,** *8* (1), 1-10.
92. Sindoro, M.; Yanai, N.; Jee, A.-Y.; Granick, S., Colloidal-sized metal–organic frameworks: synthesis and applications. *Accounts of chemical research* **2014,** *47* (2), 459-469.
93. Morris, W.; Wang, S.; Cho, D.; Auyeung, E.; Li, P.; Farha, O. K.; Mirkin, C. A., Role of modulators in controlling the colloidal stability and polydispersity of the UiO-66 metal–organic framework. *ACS applied materials & interfaces* **2017,** *9* (39), 33413-33418.
94. Fröhlich, E., The role of surface charge in cellular uptake and cytotoxicity of medical nanoparticles. *International journal of nanomedicine* **2012,** *7*, 5577.

95. Baati, T.; Njim, L.; Neffati, F.; Kerkeni, A.; Bouttemi, M.; Gref, R.; Najjar, M. F.; Zakhama, A.; Couvreur, P.; Serre, C., In depth analysis of the in vivo toxicity of nanoparticles of porous iron (III) metal–organic frameworks. *Chem. Sci.* **2013,** *4* (4), 1597-1607.
96. He, C.; Liu, D.; Lin, W., Nanomedicine applications of hybrid nanomaterials built from metal–ligand coordination bonds: nanoscale metal–organic frameworks and nanoscale coordination polymers. *Chem. Rev.* **2015,** *115* (19), 11079-11108.
97. Ruyra, À.; Yazdi, A.; Espín, J.; Carné-Sánchez, A.; Roher, N.; Lorenzo, J.; Imaz, I.; Maspoch, D., Synthesis, culture medium stability, and in vitro and in vivo zebrafish embryo toxicity of metal–organic framework nanoparticles. *Chemistry–A European Journal* **2015,** *21* (6), 2508-2518.
98. Morris, W.; Briley, W. E.; Auyeung, E.; Cabezas, M. D.; Mirkin, C. A., Nucleic acid–metal organic framework (MOF) nanoparticle conjugates. *J. Am. Chem. Soc.* **2014,** *136* (20), 7261-7264.
99. He, C.; Lu, K.; Liu, D.; Lin, W., Nanoscale metal–organic frameworks for the co-delivery of cisplatin and pooled siRNAs to enhance therapeutic efficacy in drug-resistant ovarian cancer cells. *J. Am. Chem. Soc.* **2014,** *136* (14), 5181-5184.
100. Wang, S.; McGuirk, C. M.; Ross, M. B.; Wang, S.; Chen, P.; Xing, H.; Liu, Y.; Mirkin, C. A., General and direct method for preparing oligonucleotide-functionalized metal–organic framework nanoparticles. *J. Am. Chem. Soc.* **2017,** *139* (29), 9827-9830.
101. Wang, Z.; Fu, Y.; Kang, Z.; Liu, X.; Chen, N.; Wang, Q.; Tu, Y.; Wang, L.; Song, S.; Ling, D., Organelle-specific triggered release of immunostimulatory oligonucleotides from intrinsically coordinated DNA–metal–organic frameworks with soluble exoskeleton. *J. Am. Chem. Soc.* **2017,** *139* (44), 15784-15791.
102. Mondloch, J. E.; Bury, W.; Fairen-Jimenez, D.; Kwon, S.; DeMarco, E. J.; Weston, M. H.; Sarjeant, A. A.; Nguyen, S. T.; Stair, P. C.; Snurr, R. Q., Vapor-phase metalation by atomic layer deposition in a metal–organic framework. *J. Am. Chem. Soc.* **2013,** *135* (28), 10294-10297.
103. Morris, W.; Volosskiy, B.; Demir, S.; Gándara, F.; McGrier, P. L.; Furukawa, H.; Cascio, D.; Stoddart, J. F.; Yaghi, O. M., Synthesis, structure, and metalation of two new highly porous zirconium metal–organic frameworks. *Inorganic chemistry* **2012,** *51* (12), 6443-6445.
104. Feng, D.; Gu, Z. Y.; Li, J. R.; Jiang, H. L.; Wei, Z.; Zhou, H. C., Zirconium-metalloporphyrin PCN-222: mesoporous metal–organic frameworks with ultrahigh stability as biomimetic catalysts. *Angew. Chem. Int. Ed.* **2012,** *51* (41), 10307-10310.
105. Chen, Y.; Li, P.; Modica, J. A.; Drout, R. J.; Farha, O. K., Acid-Resistant Mesoporous Metal–Organic Framework toward Oral Insulin Delivery: Protein Encapsulation, Protection, and Release. *J. Am. Chem. Soc.* **2018,** *140* (17), 5678-5681.
106. Narayan, S. P.; Choi, C. H. J.; Hao, L.; Calabrese, C. M.; Auyeung, E.; Zhang, C.; Goor, O. J.; Mirkin, C. A., The Sequence-Specific Cellular Uptake of Spherical Nucleic Acid Nanoparticle Conjugates. *Small* **2015,** *11* (33), 4173-4182.
107. Libanati, C. M.; Tandler, C. J., THE DISTRIBUTION OF THE WATER-SOLUBLE INORGANIC ORTHOPHOSPHATE IONS WITHIN THE CELL: ACCUMULATION IN THE NUCLEUS: Electron Probe Microanalysis. *The Journal of cell biology* **1969,** *42* (3), 754-765.
108. Bansal, V. K., Serum inorganic phosphorus. *Clinical methods: The History, Physical, and Laboratory Examinations. 3rd edition* **1990**.
109. Feng, D.; Liu, T.-F.; Su, J.; Bosch, M.; Wei, Z.; Wan, W.; Yuan, D.; Chen, Y.-P.; Wang, X.; Wang, K., Stable metal-organic frameworks containing single-molecule traps for enzyme encapsulation. *Nat. Commun.* **2015,** *6* (1), 1-8.

110. Ducat, D. C.; Way, J. C.; Silver, P. A., Engineering cyanobacteria to generate high-value products. *Trends Biotechnol.* **2011,** *29* (2), 95-103.
111. Tranvik, L. J.; Downing, J. A.; Cotner, J. B.; Loiselle, S. A.; Striegl, R. G.; Ballatore, T. J.; Dillon, P.; Finlay, K.; Fortino, K.; Knoll, L. B.; Kortelainen, P. L.; Kutser, T.; Larsen, S.; Laurion, I.; Leech, D. M.; McCallister, S. L.; McKnight, D. M.; Melack, J. M.; Overholt, E.; Porter, J. A.; Prairie, Y.; Renwick, W. H.; Roland, F.; Sherman, B. S.; Schindler, D. W.; Sobek, S.; Tremblay, A.; Vanni, M. J.; Verschoor, A. M.; Wachenfeldt, E. V.; Weyhenmeyer, G. A., Lakes and reservoirs as regulators of carbon cycling and climate. *Limnol Oceanogr* **2009,** *54* (6part2), 2298-2314.
112. Mikkelsen, M.; Jørgensen, M.; Krebs, F. C., The teraton challenge. A review of fixation and transformation of carbon dioxide. *Energy Environ. Sci.* **2010,** *3* (1), 43-81.
113. Samanta, A.; Zhao, A.; Shimizu, G. K.; Sarkar, P.; Gupta, R., Post-combustion CO2 capture using solid sorbents: a review. *Ind. Eng. Chem. Res.* **2011,** *51* (4), 1438-1463.
114. Abanades, J. C.; Rubin, E. S.; Anthony, E. J., Sorbent cost and performance in CO2 capture systems. *Ind. Eng. Chem. Res.* **2004,** *43* (13), 3462-3466.
115. Trickett, C. A.; Helal, A.; Al-Maythalony, B. A.; Yamani, Z. H.; Cordova, K. E.; Yaghi, O. M., The chemistry of metal–organic frameworks for CO 2 capture, regeneration and conversion. *Nat. Rev. Mater.* **2017,** *2* (8), 17045.
116. Root, T. L.; Price, J. T.; Hall, K. R.; Schneider, S. H.; Rosenzweig, C.; Pounds, J. A., Fingerprints of global warming on wild animals and plants. *Nature* **2003,** *421* (6918), 57.
117. Yang, H.; Xu, Z.; Fan, M.; Gupta, R.; Slimane, R. B.; Bland, A. E.; Wright, I., Progress in carbon dioxide separation and capture: A review. *Journal of environmental sciences* **2008,** *20* (1), 14-27.
118. Kumar, A.; Ergas, S.; Yuan, X.; Sahu, A.; Zhang, Q.; Dewulf, J.; Malcata, F. X.; Van Langenhove, H., Enhanced CO2 fixation and biofuel production via microalgae: recent developments and future directions. *Trends Biotechnol.* **2010,** *28* (7), 371-380.
119. Walcarius, A.; Nasraoui, R.; Wang, Z.; Qu, F.; Urbanova, V.; Etienne, M.; Göllü, M.; Demir, A. S.; Gajdzik, J.; Hempelmann, R., Factors affecting the electrochemical regeneration of NADH by (2, 2′-bipyridyl)(pentamethylcyclopentadienyl)-rhodium complexes: Impact on their immobilization onto electrode surfaces. *Bioelectrochemistry* **2011,** *82* (1), 46-54.
120. Ali, I.; Gill, A.; Omanovic, S., Direct electrochemical regeneration of the enzymatic cofactor 1, 4-NADH employing nano-patterned glassy carbon/Pt and glassy carbon/Ni electrodes. *Chem. Eng. J.* **2012,** *188*, 173-180.
121. Yadav, R. K.; Baeg, J.-O.; Oh, G. H.; Park, N.-J.; Kong, K.-j.; Kim, J.; Hwang, D. W.; Biswas, S. K., A photocatalyst–enzyme coupled artificial photosynthesis system for solar energy in production of formic acid from CO2. *J. Am. Chem. Soc.* **2012,** *134* (28), 11455-11461.
122. Liu, J.; Antonietti, M., Bio-inspired NADH regeneration by carbon nitride photocatalysis using diatom templates. *Energy Environ. Sci.* **2013,** *6* (5), 1486-1493.
123. Yan, M.; Ge, J.; Liu, Z.; Ouyang, P., Encapsulation of single enzyme in nanogel with enhanced biocatalytic activity and stability. *J. Am. Chem. Soc.* **2006,** *128* (34), 11008-11009.
124. Liang, K.; Coghlan, C. J.; Bell, S. G.; Doonan, C.; Falcaro, P., Enzyme encapsulation in zeolitic imidazolate frameworks: a comparison between controlled co-precipitation and biomimetic mineralisation. *Chem. Commun.* **2016,** *52* (3), 473-476.

125. Sutter, M.; Boehringer, D.; Gutmann, S.; Günther, S.; Prangishvili, D.; Loessner, M. J.; Stetter, K. O.; Weber-Ban, E.; Ban, N., Structural basis of enzyme encapsulation into a bacterial nanocompartment. *Nat. Struct. Mol. Biol.* **2008,** *15* (9), 939.
126. Sheldon, R. A., Enzyme immobilization: the quest for optimum performance. *Adv. Synth. Catal.* **2007,** *349* (8-9), 1289-1307.
127. Mateo, C.; Fernández-Lorente, G.; Abian, O.; Fernández-Lafuente, R.; Guisán, J. M., Multifunctional epoxy supports: a new tool to improve the covalent immobilization of proteins. The promotion of physical adsorptions of proteins on the supports before their covalent linkage. *Biomacromolecules* **2000,** *1* (4), 739-745.
128. Hirsh, S.; Bilek, M.; Nosworthy, N.; Kondyurin, A.; Dos Remedios, C.; McKenzie, D., A comparison of covalent immobilization and physical adsorption of a cellulase enzyme mixture. *Langmuir* **2010,** *26* (17), 14380-14388.
129. Migneault, I.; Dartiguenave, C.; Bertrand, M. J.; Waldron, K. C., Glutaraldehyde: behavior in aqueous solution, reaction with proteins, and application to enzyme crosslinking. *BioTechniques* **2004,** *37* (5), 790-802.
130. Govardhan, C. P., Crosslinking of enzymes for improved stability and performance. *CURR OPIN BIOTECH* **1999,** *10* (4), 331-335.
131. Zhou, H.-C.; Long, J. R.; Yaghi, O. M., Introduction to metal–organic frameworks. Chem. Rev.: 2012; Vol. 112, pp 673-674.
132. Farha, O. K.; Hupp, J. T., Rational design, synthesis, purification, and activation of metal− organic framework materials. *Acc. Chem. Res.* **2010,** *43* (8), 1166-1175.
133. Wu, D.; Guo, Z.; Yin, X.; Pang, Q.; Tu, B.; Zhang, L.; Wang, Y. G.; Li, Q., Metal–organic frameworks as cathode materials for Li–O2 batteries. *Adv. Mater.* **2014,** *26* (20), 3258-3262.
134. Zhang, Z.; Yao, Z.-Z.; Xiang, S.; Chen, B., Perspective of microporous metal–organic frameworks for CO 2 capture and separation. *Energy Environ. Sci.* **2014,** *7* (9), 2868-2899.
135. Kajiwara, T.; Fujii, M.; Tsujimoto, M.; Kobayashi, K.; Higuchi, M.; Tanaka, K.; Kitagawa, S., Photochemical Reduction of Low Concentrations of CO2 in a Porous Coordination Polymer with a Ruthenium (II)–CO Complex. *Angew. Chem. Int. Ed.* **2016,** *55* (8), 2697-2700.
136. Wang, X.-G.; Dong, Z.-Y.; Cheng, H.; Wan, S.-S.; Chen, W.-H.; Zou, M.-Z.; Huo, J.-W.; Deng, H.-X.; Zhang, X.-Z., A multifunctional metal–organic framework based tumor targeting drug delivery system for cancer therapy. *Nanoscale* **2015,** *7* (38), 16061-16070.
137. Tan, L. L.; Li, H.; Zhou, Y.; Zhang, Y.; Feng, X.; Wang, B.; Yang, Y. W., Zn2+-Triggered Drug Release from Biocompatible Zirconium MOFs Equipped with Supramolecular Gates. *Small* **2015,** *11* (31), 3807-3813.
138. Wu, X.; Ge, J.; Yang, C.; Hou, M.; Liu, Z., Facile synthesis of multiple enzyme-containing metal–organic frameworks in a biomolecule-friendly environment. *Chem. Commun.* **2015,** *51* (69), 13408-13411.
139. Cavka, J. H.; Jakobsen, S.; Olsbye, U.; Guillou, N.; Lamberti, C.; Bordiga, S.; Lillerud, K. P., A new zirconium inorganic building brick forming metal organic frameworks with exceptional stability. *J. Am. Chem. Soc.* **2008,** *130* (42), 13850-13851.
140. Noh, H.; Kung, C.-W.; Otake, K.-i.; Peters, A. W.; Li, Z.; Liao, Y.; Gong, X.; Farha, O. K.; Hupp, J. T., Redox-Mediator-Assisted Electrocatalytic Hydrogen Evolution from Water by a Molybdenum Sulfide-Functionalized Metal–Organic Framework. *ACS Catal.* **2018,** *8* (10), 9848-9858.

141. Buru, C. T.; Li, P.; Mehdi, B. L.; Dohnalkova, A.; Platero-Prats, A. E.; Browning, N. D.; Chapman, K. W.; Hupp, J. T.; Farha, O. K., Adsorption of a catalytically accessible polyoxometalate in a mesoporous channel-type metal–organic framework. *Chem. Mater.* **2017,** *29* (12), 5174-5181.
142. Manna, K.; Zhang, T.; Lin, W., Postsynthetic metalation of bipyridyl-containing metal–organic frameworks for highly efficient catalytic organic transformations. *J. Am. Chem. Soc.* **2014,** *136* (18), 6566-6569.
143. Alkordi, M. H.; Liu, Y.; Larsen, R. W.; Eubank, J. F.; Eddaoudi, M., Zeolite-like metal− organic frameworks as platforms for applications: on metalloporphyrin-based catalysts. *J. Am. Chem. Soc.* **2008,** *130* (38), 12639-12641.
144. Lyu, J.; Zhang, X.; Otake, K.-i.; Wang, X.; Li, P.; Li, Z.; Chen, Z.; Zhang, Y.; Wasson, M. C.; Yang, Y., Topology and porosity control of metal–organic frameworks through linker functionalization. *Chem. Sci.* **2019,** *10* (4), 1186-1192.
145. Ma, L.; Falkowski, J. M.; Abney, C.; Lin, W., A series of isoreticular chiral metal–organic frameworks as a tunable platform for asymmetric catalysis. *Nat. Chem.* **2010,** *2* (10), 838.
146. Zhang, X.; Huang, Z.; Ferrandon, M.; Yang, D.; Robison, L.; Li, P.; Wang, T. C.; Delferro, M.; Farha, O. K., Catalytic chemoselective functionalization of methane in a metal− organic framework. *Nat. Catal.* **2018,** *1* (5), 356.
147. Crable, B. R.; Plugge, C. M.; McInerney, M. J.; Stams, A. J., Formate formation and formate conversion in biological fuels production. *Enzyme Res.* **2011,** *2011*.
148. Bolivar, J. M.; Wilson, L.; Ferrarotti, S. A.; Fernandez-Lafuente, R.; Guisan, J. M.; Mateo, C., Stabilization of a formate dehydrogenase by covalent immobilization on highly activated glyoxyl-agarose supports. *Biomacromolecules* **2006,** *7* (3), 669-673.
149. Akers, N. L.; Moore, C. M.; Minteer, S. D., Development of alcohol/O2 biofuel cells using salt-extracted tetrabutylammonium bromide/Nafion membranes to immobilize dehydrogenase enzymes. *Electrochim. Acta* **2005,** *50* (12), 2521-2525.
150. Chen, X.; Cao, Y.; Li, F.; Tian, Y.; Song, H., Enzyme-Assisted Microbial Electrosynthesis of Poly (3-hydroxybutyrate) via CO2 Bioreduction by Engineered Ralstonia eutropha. *ACS Catalysis* **2018,** *8* (5), 4429-4437.
151. Liao, J. C.; Mi, L.; Pontrelli, S.; Luo, S., Fuelling the future: microbial engineering for the production of sustainable biofuels. *Nat. Rev. Microbiol* **2016,** *14* (5), 288.
152. Kim, M. H.; Park, S.; Kim, Y. H.; Won, K.; Lee, S. H., Immobilization of formate dehydrogenase from Candida boidinii through cross-linked enzyme aggregates. *J. Mol. Catal. B: Enzym.* **2013,** *97*, 209-214.
153. Choe, H.; Joo, J. C.; Cho, D. H.; Kim, M. H.; Lee, S. H.; Jung, K. D.; Kim, Y. H., Efficient CO2-reducing activity of NAD-dependent formate dehydrogenase from Thiobacillus sp. KNK65MA for formate production from CO2 gas. *PLoS One* **2014,** *9* (7), e103111.
154. Li, P.; Chen, Q.; Wang, T. C.; Vermeulen, N. A.; Mehdi, B. L.; Dohnalkova, A.; Browning, N. D.; Shen, D.; Anderson, R.; Gómez-Gualdrón, D. A.; Cetin, F. M.; Jagiello, J.; Asiri, A. M.; Stoddart, J. F.; Farha, O. k., Hierarchically Engineered Mesoporous Metal-Organic Frameworks toward Cell-free Immobilized Enzyme Systems. *Chem* **2018,** *4* (5), 1022-1034.
155. Chambers, M. B.; Wang, X.; Elgrishi, N.; Hendon, C. H.; Walsh, A.; Bonnefoy, J.; Canivet, J.; Quadrelli, E. A.; Farrusseng, D.; Mellot-Draznieks, C., Photocatalytic Carbon Dioxide Reduction with Rhodium-based Catalysts in Solution and Heterogenized within Metal–Organic Frameworks. *ChemSusChem* **2015,** *8* (4), 603-608.

156. Buru, C. T.; Platero-Prats, A. E.; Chica, D. G.; Kanatzidis, M. G.; Chapman, K. W.; Farha, O. K., Thermally induced migration of a polyoxometalate within a metal–organic framework and its catalytic effects. *J. Mater. Chem. A* **2018,** *6* (17), 7389-7394.
157. Zamorano, A.; Rendon, N.; Lopez-Serrano, J.; Alvarez, E.; Carmona, E., Activation of Small Molecules by the Metal–Amido Bond of Rhodium (III) and Iridium (III)(η5-C5Me5) M-Aminopyridinate Complexes. *Inorg. Chem.* **2017,** *57* (1), 150-162.
158. Ganesan, V.; Sivanesan, D.; Yoon, S., Correlation between the structure and catalytic activity of [Cp* Rh (substituted bipyridine)] complexes for NADH regeneration. *Inorg. Chem.* **2017,** *56* (3), 1366-1374.
159. Scheer, H., *The solar economy: Renewable energy for a sustainable global future*. Routledge: 2013.
160. Green, M. A.; Emery, K.; Hishikawa, Y.; Warta, W.; Dunlop, E. D., Solar cell efficiency tables (version 41). *Prog. Photovoltaics* **2013,** *21* (1), 1-11.
161. Rudroff, F.; Mihovilovic, M. D.; Gröger, H.; Snajdrova, R.; Iding, H.; Bornscheuer, U. T., Opportunities and challenges for combining chemo-and biocatalysis. *Nat. Catal.* **2018,** *1* (1), 12.
162. Wang, J.-L.; Wang, C.; Lin, W., Metal–organic frameworks for light harvesting and photocatalysis. *ACS Catal.* **2012,** *2* (12), 2630-2640.
163. Foster, M. E.; Azoulay, J. D.; Wong, B. M.; Allendorf, M. D., Novel metal–organic framework linkers for light harvesting applications. *Chem. Sci.* **2014,** *5* (5), 2081-2090.
164. Stavila, V.; Talin, A. A.; Allendorf, M. D., MOF-based electronic and opto-electronic devices. *Chem. Soc. Rev.* **2014,** *43* (16), 5994-6010.
165. Kornienko, N.; Zhang, J. Z.; Sakimoto, K. K.; Yang, P.; Reisner, E., Interfacing nature's catalytic machinery with synthetic materials for semi-artificial photosynthesis. *Nat. Nanotechnol.* **2018,** *13* (10), 890.
166. Lee, M.; Kim, J. H.; Lee, S. H.; Lee, S. H.; Park, C. B., Biomimetic Artificial Photosynthesis by Light-Harvesting Synthetic Wood. *ChemSusChem* **2011,** *4* (5), 581-586.
167. Ji, X.; Wang, J.; Mei, L.; Tao, W.; Barrett, A.; Su, Z.; Wang, S.; Ma, G.; Shi, J.; Zhang, S., Porphyrin/SiO2/Cp*Rh(bpy)Cl Hybrid Nanoparticles Mimicking Chloroplast with Enhanced Electronic Energy Transfer for Biocatalyzed Artificial Photosynthesis. *Adv. Funct. Mater.* **2018,** *28* (9), 1705083.
168. Hollmann, F.; Witholt, B.; Schmid, A., [Cp∗ Rh (bpy)(H2O)] 2+: a versatile tool for efficient and non-enzymatic regeneration of nicotinamide and flavin coenzymes. *J. Mol. Catal. B: Enzym.* **2002,** *19*, 167-176.
169. Oppelt, K. T.; Gasiorowski, J.; Egbe, D. A. M.; Kollender, J. P.; Himmelsbach, M.; Hassel, A. W.; Sariciftci, N. S.; Knör, G., Rhodium-Coordinated Poly(arylene-ethynylene)-alt-Poly(arylene-vinylene) Copolymer Acting as Photocatalyst for Visible-Light-Powered NAD+/NADH Reduction. *J. Am. Chem. Soc.* **2014,** *136* (36), 12721-12729.
170. Evans, J. D.; Sumby, C. J.; Doonan, C. J., Post-synthetic metalation of metal–organic frameworks. *Chem. Soc. Rev.* **2014,** *43* (16), 5933-5951.
171. Feng, L.; Wang, Y.; Yuan, S.; Wang, K.-Y.; Li, J.-L.; Day, G. S.; Qiu, D.; Cheng, L.; Chen, W.-M.; Madrahimov, S. T.; Zhou, H.-C., Porphyrinic Metal–Organic Frameworks Installed with Brønsted Acid Sites for Efficient Tandem Semisynthesis of Artemisinin. *ACS Catalysis* **2019,** *9* (6), 5111-5118.

172. Liao, F.-S.; Lo, W.-S.; Hsu, Y.-S.; Wu, C.-C.; Wang, S.-C.; Shieh, F.-K.; Morabito, J. V.; Chou, L.-Y.; Wu, K. C.-W.; Tsung, C.-K., Shielding against unfolding by embedding enzymes in metal–organic frameworks via a de novo approach. *J. Am. Chem. Soc.* **2017,** *139* (19), 6530-6533.
173. Miyatani, R.; Amao, Y., Photochemical synthesis of formic acid from CO2 with formate dehydrogenase and water-soluble zinc porphyrin. *J. Mol. Catal. B Enzym.* **2004,** *27* (2-3), 121-125.
174. Tsujisho, I.; Toyoda, M.; Amao, Y., Photochemical and enzymatic synthesis of formic acid from CO2 with chlorophyll and dehydrogenase system. *Catal. Commun.* **2006,** *7* (3), 173-176.
175. Ikeyama, S.; Amao, Y., An Artificial Co-enzyme Based on the Viologen Skeleton for Highly Efficient CO2 Reduction to Formic Acid with Formate Dehydrogenase. *ChemCatChem* **2017,** *9* (5), 833-838.
176. Farha, O. K.; Özgür Yazaydın, A.; Eryazici, I.; Malliakas, C. D.; Hauser, B. G.; Kanatzidis, M. G.; Nguyen, S. T.; Snurr, R. Q.; Hupp, J. T., De novo synthesis of a metal–organic framework material featuring ultrahigh surface area and gas storage capacities. *Nat. Chem.* **2010,** *2*, 944.
177. Matsuda, R.; Kitaura, R.; Kitagawa, S.; Kubota, Y.; Belosludov, R. V.; Kobayashi, T. C.; Sakamoto, H.; Chiba, T.; Takata, M.; Kawazoe, Y., Highly controlled acetylene accommodation in a metal–organic microporous material. *Nature* **2005,** *436* (7048), 238.
178. Li, J.-R.; Kuppler, R. J.; Zhou, H.-C., Selective gas adsorption and separation in metal–organic frameworks. *Chem. Soc. Rev.* **2009,** *38* (5), 1477-1504.
179. Hartlieb, K. J.; Holcroft, J. M.; Moghadam, P. Z.; Vermeulen, N. A.; Algaradah, M. M.; Nassar, M. S.; Botros, Y. Y.; Snurr, R. Q.; Stoddart, J. F., CD-MOF: a versatile separation medium. *J. Am. Chem. Soc.* **2016,** *138* (7), 2292-2301.
180. Lee, J.; Farha, O. K.; Roberts, J.; Scheidt, K. A.; Nguyen, S. T.; Hupp, J. T., Metal–organic framework materials as catalysts. *Chem. Soc. Rev.* **2009,** *38* (5), 1450-1459.
181. Diercks, C. S.; Liu, Y.; Cordova, K. E.; Yaghi, O. M., The role of reticular chemistry in the design of CO2 reduction catalysts. *Nat. Mater.* **2018,** *17* (4), 301-307.
182. So, M. C.; Wiederrecht, G. P.; Mondloch, J. E.; Hupp, J. T.; Farha, O. K., Metal–organic framework materials for light-harvesting and energy transfer. *Chem. Commun.* **2015,** *51* (17), 3501-3510.
183. Kent, C. A.; Liu, D.; Ma, L.; Papanikolas, J. M.; Meyer, T. J.; Lin, W., Light harvesting in microscale metal–organic frameworks by energy migration and interfacial electron transfer quenching. *J. Am. Chem. Soc.* **2011,** *133* (33), 12940-12943.
184. Jin, S.; Son, H.-J.; Farha, O. K.; Wiederrecht, G. P.; Hupp, J. T., Energy transfer from quantum dots to metal–organic frameworks for enhanced light harvesting. *J. Am. Chem. Soc.* **2013,** *135* (3), 955-958.
185. Lee, C. Y.; Farha, O. K.; Hong, B. J.; Sarjeant, A. A.; Nguyen, S. T.; Hupp, J. T., Light-Harvesting Metal–Organic Frameworks (MOFs): Efficient Strut-to-Strut Energy Transfer in Bodipy and Porphyrin-Based MOFs. *J. Am. Chem. Soc.* **2011,** *133* (40), 15858-15861.
186. Liu, Y.; Buru, C. T.; Howarth, A. J.; Mahle, J. J.; Buchanan, J. H.; DeCoste, J. B.; Hupp, J. T.; Farha, O. K., Efficient and selective oxidation of sulfur mustard using singlet oxygen generated by a pyrene-based metal–organic framework. *J. Mater. Chem. A* **2016,** *4* (36), 13809-13813.
187. Chen, Q.; Sun, J.; Li, P.; Hod, I.; Moghadam, P. Z.; Kean, Z. S.; Snurr, R. Q.; Hupp, J. T.; Farha, O. K.; Stoddart, J. F., A Redox-Active Bistable Molecular Switch Mounted inside a Metal–Organic Framework. *J. Am. Chem. Soc.* **2016,** *138* (43), 14242-14245.

188. Li, P.; Moon, S.-Y.; Guelta, M. A.; Lin, L.; Gómez-Gualdrón, D. A.; Snurr, R. Q.; Harvey, S. P.; Hupp, J. T.; Farha, O. K., Nanosizing a metal–organic framework enzyme carrier for accelerating nerve agent hydrolysis. *ACS nano* **2016,** *10* (10), 9174-9182.
189. Howarth, A. J.; Buru, C. T.; Liu, Y.; Ploskonka, A. M.; Hartlieb, K. J.; McEntee, M.; Mahle, J. J.; Buchanan, J. H.; Durke, E. M.; Al-Juaid, S. S., Postsynthetic incorporation of a singlet oxygen photosensitizer in a metal–organic framework for fast and selective oxidative detoxification of sulfur mustard. *Chemistry–A European Journal* **2017,** *23* (1), 214-218.
190. Chen, Y.; Li, P.; Noh, H.; Kung, C. W.; Buru, C. T.; Wang, X.; Zhang, X.; Farha, O. K., Stabilization of Formate Dehydrogenase in a Metal–Organic Framework for Bioelectrocatalytic Reduction of CO2. *Angew. Chem. Int. Ed.* **2019,** *131* (23), 5.
191. Deria, P.; Mondloch, J. E.; Tylianakis, E.; Ghosh, P.; Bury, W.; Snurr, R. Q.; Hupp, J. T.; Farha, O. K., Perfluoroalkane functionalization of NU-1000 via solvent-assisted ligand incorporation: synthesis and CO2 adsorption studies. *J. Am. Chem. Soc.* **2013,** *135* (45), 16801-16804.
192. Leonat, L.; Sbarcea, G.; Branzoi, I. V., Cyclic voltammetry for energy levels estimation of organic materials. *UPB Sci Bull Ser B* **2013,** *75*, 111-118.
193. Hollmann, F.; Schmid, A.; Steckhan, E., The first synthetic application of a monooxygenase employing indirect electrochemical NADH regeneration. *Angew. Chem. Int. Ed.* **2001,** *40* (1), 169-171.
194. Dunn, P. J., The importance of green chemistry in process research and development. *Chem. Soc. Rev.* **2012,** *41* (4), 1452-1461.
195. Panganiban, B.; Qiao, B.; Jiang, T.; DelRe, C.; Obadia, M. M.; Nguyen, T. D.; Smith, A. A.; Hall, A.; Sit, I.; Crosby, M. G., Random heteropolymers preserve protein function in foreign environments. *Science* **2018,** *359* (6381), 1239-1243.
196. Arnold, F. H., Directed evolution: bringing new chemistry to life. *Angew. Chem. Int. Ed.* **2018,** *57* (16), 4143-4148.
197. Homaei, A. A.; Sariri, R.; Vianello, F.; Stevanato, R., Enzyme immobilization: an update. *J. Chem. Biol.* **2013,** *6* (4), 185-205.
198. Luckarift, H. R.; Spain, J. C.; Naik, R. R.; Stone, M. O., Enzyme immobilization in a biomimetic silica support. *Nat. Biotechnol.* **2004,** *22* (2), 211-213.
199. Betancor, L.; Luckarift, H. R., Bioinspired enzyme encapsulation for biocatalysis. *Trends Biotechnol.* **2008,** *26* (10), 566-572.
200. Caruso, F.; Trau, D.; Möhwald, H.; Renneberg, R., Enzyme encapsulation in layer-by-layer engineered polymer multilayer capsules. *Langmuir.* **2000,** *16* (4), 1485-1488.
201. Ai, H.; Jones, S. A.; Lvov, Y. M., Biomedical applications of electrostatic layer-by-layer nano-assembly of polymers, enzymes, and nanoparticles. *Cell Biochem. Biophys.* **2003,** *39* (1), 23.
202. Nguyen, T. D.; Qiao, B.; de la Cruz, M. O., Efficient encapsulation of proteins with random copolymers. *Proc. Natl. Acad. Sci. U.S.A.* **2018,** *115* (26), 6578-6583.
203. Fan, C.; Cheng, S.; Sinha, S.; Bobik, T. A., Interactions between the termini of lumen enzymes and shell proteins mediate enzyme encapsulation into bacterial microcompartments. *Proc. Natl. Acad. Sci. U.S.A.* **2012,** *109* (37), 14995-15000.
204. Shekhah, O.; Belmabkhout, Y.; Chen, Z.; Guillerm, V.; Cairns, A.; Adil, K.; Eddaoudi, M., Made-to-order metal-organic frameworks for trace carbon dioxide removal and air capture. *Nat. Commun.* **2014,** *5* (1), 1-7.

205. Chen, Z.; Adil, K.; Weseliński, Ł. J.; Belmabkhout, Y.; Eddaoudi, M., A supermolecular building layer approach for gas separation and storage applications: the eea and rtl MOF platforms for CO 2 capture and hydrocarbon separation. *J. Mater. Chem. A* **2015,** *3* (12), 6276-6281.
206. Kim, H.; Yang, S.; Rao, S. R.; Narayanan, S.; Kapustin, E. A.; Furukawa, H.; Umans, A. S.; Yaghi, O. M.; Wang, E. N., Water harvesting from air with metal-organic frameworks powered by natural sunlight. *Science* **2017,** *356* (6336), 430-434.
207. Ikezoe, Y.; Fang, J.; Wasik, T. L.; Shi, M.; Uemura, T.; Kitagawa, S.; Matsui, H., Peptide–metal organic framework swimmers that direct the motion toward chemical targets. *Nano Lett.* **2015,** *15* (6), 4019-4023.
208. Taylor-Pashow, K. M.; Della Rocca, J.; Xie, Z.; Tran, S.; Lin, W., Postsynthetic modifications of iron-carboxylate nanoscale metal− organic frameworks for imaging and drug delivery. *J. Am. Chem. Soc.* **2009,** *131* (40), 14261-14263.
209. Feng, L.; Wang, Y.; Yuan, S.; Wang, K.-Y.; Li, J.-L.; Day, G. S.; Qiu, D.; Cheng, L.; Chen, W.-M.; Madrahimov, S. T., Porphyrinic Metal–Organic Frameworks Installed with Brønsted Acid Sites for Efficient Tandem Semisynthesis of Artemisinin. *ACS Catal.* **2019,** *9* (6), 5111-5118.
210. Zhang, X.; Huang, Z.; Ferrandon, M.; Yang, D.; Robison, L.; Li, P.; Wang, T. C.; Delferro, M.; Farha, O. K., Catalytic chemoselective functionalization of methane in a metal− organic framework. *Nat. Catal.* **2018,** *1* (5), 356-362.
211. Kreno, L. E.; Leong, K.; Farha, O. K.; Allendorf, M.; Van Duyne, R. P.; Hupp, J. T., Metal–organic framework materials as chemical sensors. *Chem. Rev.* **2012,** *112* (2), 1105-1125.
212. Chen, Y.; Li, P.; Zhou, J.; Buru, C. T.; Đorđević, L.; Li, P.; Zhang, X.; Cetin, M. M.; Stoddart, J. F.; Stupp, S. I., Integration of Enzymes and Photosensitizers in a Hierarchical Mesoporous Metal–Organic Framework for Light-Driven CO2 Reduction. *J. Am. Chem. Soc.* **2020,** *142* (4), 5.
213. Wang, Q.; Zhang, X.; Huang, L.; Zhang, Z.; Dong, S., GOx@ ZIF-8 (NiPd) nanoflower: an artificial enzyme system for tandem catalysis. *Angew. Chem. Int. Ed.* **2017,** *56* (50), 16082-16085.
214. Chen, Y.; Li, P.; Noh, H.; Kung, C. W.; Buru, C. T.; Wang, X.; Zhang, X.; Farha, O. K., Stabilization of Formate Dehydrogenase in a Metal–Organic Framework for Bioelectrocatalytic Reduction of CO2. *Angew. Chem. Int. Ed.* **2019,** *131* (23), 7764-7768.
215. Liang, W.; Xu, H.; Carraro, F.; Maddigan, N. K.; Li, Q.; Bell, S. G.; Huang, D. M.; Tarzia, A.; Solomon, M. B.; Amenitsch, H., Enhanced activity of enzymes encapsulated in hydrophilic metal–organic frameworks. *J. Am. Chem. Soc.* **2019,** *141* (6), 2348-2355.
216. Wu, X.; Yue, H.; Zhang, Y.; Gao, X.; Li, X.; Wang, L.; Cao, Y.; Hou, M.; An, H.; Zhang, L., Packaging and delivering enzymes by amorphous metal-organic frameworks. *Nat. Commun.* **2019,** *10* (1), 1-8.
217. Hu, C.; Bai, Y.; Hou, M.; Wang, Y.; Wang, L.; Cao, X.; Chan, C.-W.; Sun, H.; Li, W.; Ge, J., Defect-induced activity enhancement of enzyme-encapsulated metal-organic frameworks revealed in microfluidic gradient mixing synthesis. *Sci. Adv.* **2020,** *6* (5), eaax5785.
218. Wu, X.; Yang, C.; Ge, J., Green synthesis of enzyme/metal-organic framework composites with high stability in protein denaturing solvents. *Bioresour. Bioprocess.* **2017,** *4* (1), 24.
219. Lin, X.; Hong, Y.; Zhang, C.; Huang, R.; Wang, C.; Lin, W., Pre-concentration and energy transfer enable the efficient luminescence sensing of transition metal ions by metal–organic frameworks. *Chem. Commun.* **2015,** *51* (95), 16996-16999.

220. Yoshikawa, S.; Muramoto, K.; Shinzawa-Itoh, K.; Mochizuki, M., Structural studies on bovine heart cytochrome c oxidase. *Biochim. Biophys. Acta* **2012,** *1817* (4), 579-589.
221. Islamoglu, T.; Otake, K.-i.; Li, P.; Buru, C. T.; Peters, A. W.; Akpinar, I.; Garibay, S. J.; Farha, O. K., Revisiting the structural homogeneity of NU-1000, a Zr-based metal–organic framework. *CrystEngComm* **2018,** *20* (39), 5913-5918.
222. Maximova, K.; Wojtczak, J.; Trylska, J., Enzyme kinetics in crowded solutions from isothermal titration calorimetry. *Anal. Bioanal. Chem.* **2019,** *567*, 96-105.
223. Mirkin, N.; Jaconcic, J.; Stojanoff, V.; Moreno, A., High resolution X-ray crystallographic structure of bovine heart cytochrome c and its application to the design of an electron transfer biosensor. *Proteins.* **2008,** *70* (1), 83-92.
224. Huang, J.; Rauscher, S.; Nawrocki, G.; Ran, T.; Feig, M.; de Groot, B. L.; Grubmüller, H.; MacKerell, A. D., CHARMM36m: an improved force field for folded and intrinsically disordered proteins. *Nat. Methods.* **2017,** *14* (1), 71-73.
225. Darden, T.; York, D.; Pedersen, L., Particle mesh Ewald: An N· log (N) method for Ewald sums in large systems. *J. Chem. Phys.* **1993,** *98* (12), 10089-10092.
226. Essmann, U.; Perera, L.; Berkowitz, M. L.; Darden, T.; Lee, H.; Pedersen, L. G., A smooth particle mesh Ewald method. *J. Chem. Phys.* **1995,** *103* (19), 8577-8593.
227. Berendsen, H. J.; van der Spoel, D.; van Drunen, R., GROMACS: a message-passing parallel molecular dynamics implementation. *Comput. Phys. Commun.* **1995,** *91* (1-3), 43-56.
228. Abraham, M. J.; Murtola, T.; Schulz, R.; Páll, S.; Smith, J. C.; Hess, B.; Lindahl, E., GROMACS: High performance molecular simulations through multi-level parallelism from laptops to supercomputers. *SoftwareX* **2015,** *1*, 19-25.
229. Planas, N.; Mondloch, J. E.; Tussupbayev, S.; Borycz, J.; Gagliardi, L.; Hupp, J. T.; Farha, O. K.; Cramer, C. J., Defining the proton topology of the Zr6-based metal–organic framework NU-1000. *J. Phys. Chem. Lett.* **2014,** *5* (21), 3716-3723.
230. Todd, M. J.; Gomez, J., Enzyme kinetics determined using calorimetry: a general assay for enzyme activity? *Anal. Bioanal. Chem.* **2001,** *296* (2), 179-187.
231. Kato, S.; Drout, R. J.; Farha, O. K., Isothermal Titration Calorimetry to Investigate Uremic Toxins Adsorbing onto Metal-Organic Frameworks. *Cell Rep. Phys. Sci.* **2020,** *1* (1), 100006.
232. Palomba, J. M.; Credille, C. V.; Kalaj, M.; DeCoste, J. B.; Peterson, G. W.; Tovar, T. M.; Cohen, S. M., High-throughput screening of solid-state catalysts for nerve agent degradation. *Chem. Commun.* **2018,** *54* (45), 5768-5771.
233. Aasa, R.; Albracht, S. P. J.; Falk, K.-E.; Lanne, B.; Vänngård, T., EPR signals from cytochrome c oxidase. *Biochimica et Biophysica Acta (BBA) - Enzymology* **1976,** *422* (2), 260-272.
234. Tsong, T. Y., Acid induced conformational transition of denatured cytochrome c in urea and guanidine hydrochloride solutions. *Biochemistry* **1975,** *14* (7), 1542-1547.
235. Petrović, J.; Clark, R. A.; Yue, H.; Waldeck, D. H.; Bowden, E. F., Impact of surface immobilization and solution ionic strength on the formal potential of immobilized cytochrome c. *Langmuir.* **2005,** *21* (14), 6308-6316.
236. Schweitzer-Stenner, R., Relating the multi-functionality of cytochrome c to membrane binding and structural conversion. *Biophys. Rev.* **2018,** *10* (4), 1151-1185.
237. Qiao, B.; Jiménez-Ángeles, F.; Nguyen, T. D.; de la Cruz, M. O., Water follows polar and nonpolar protein surface domains. *Proc. Natl. Acad. Sci. U.S.A.* **2019,** *116* (39), 19274-19281.